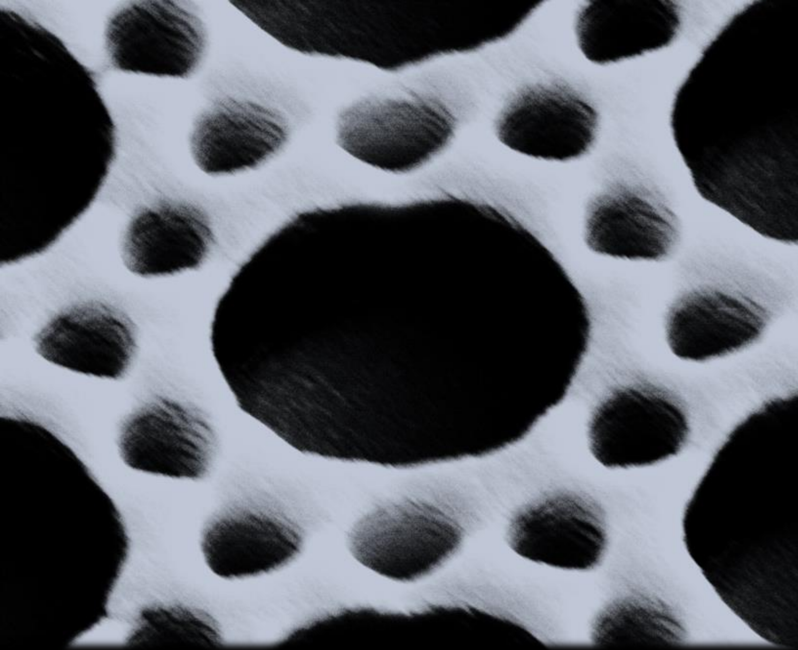
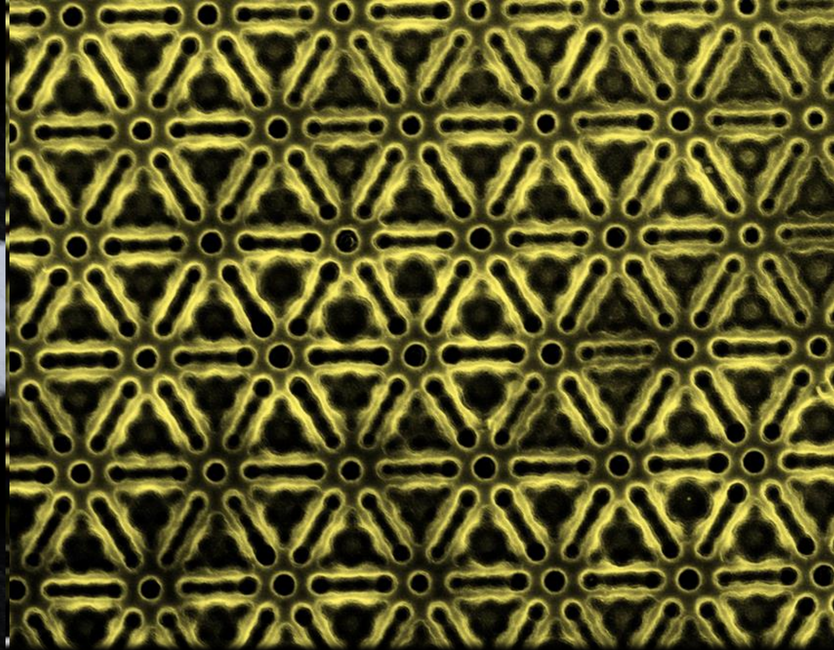

Optical Properties of micro/nano structured metal-insulator-metal nanocavities

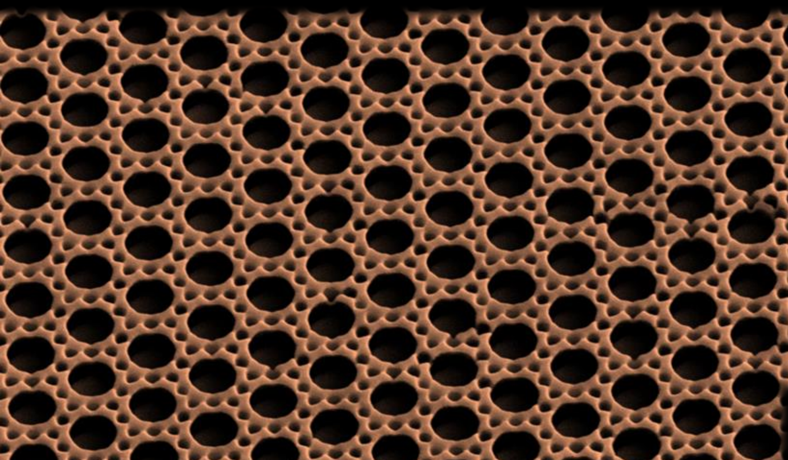
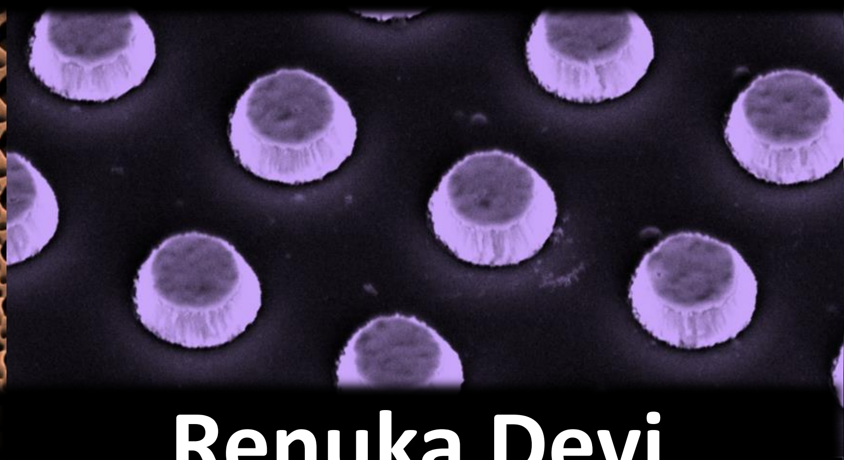

Renuka Devi Pothuraju

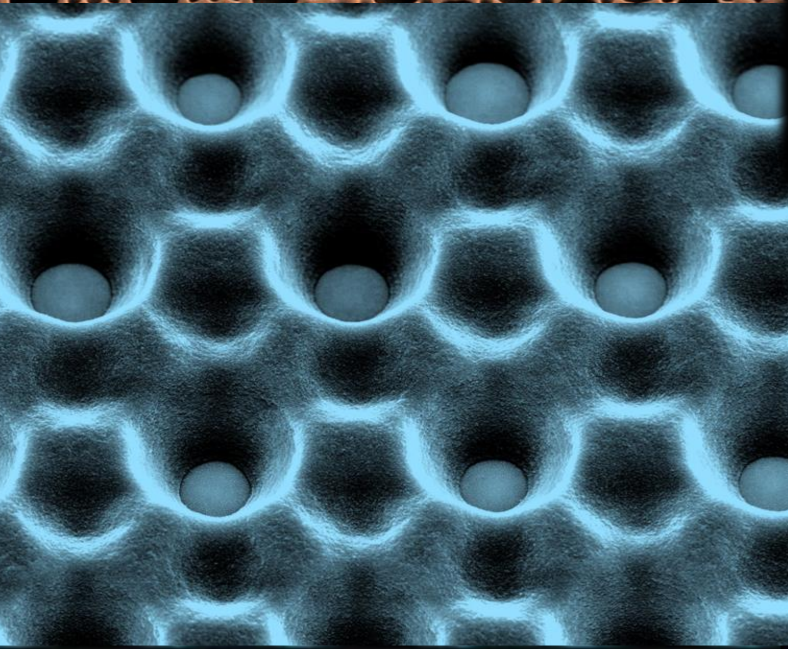
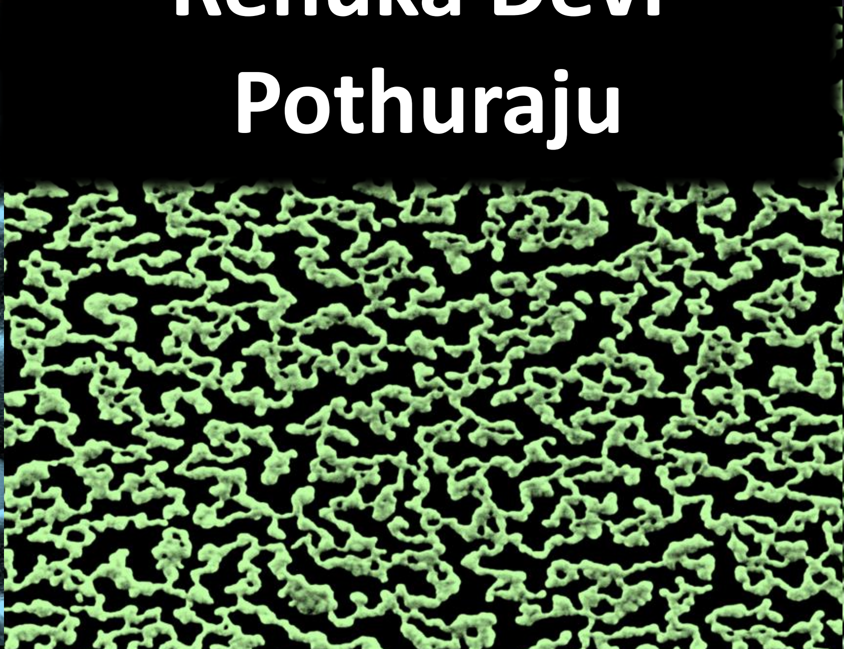

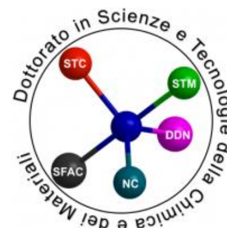

Optical Properties of Micro/Nano Structured Metal-Insulator-Metal Nanocavities

Thesis submitted in partial fulfilment to obtain

Doctorate in Sciences and Technologies of Chemistry and Materials

by

Venkata Naga Sri Renuka Devi Pothuraju

March 2022

Supervisors:

Prof. Roman Krahne

Prof. Maurizio Canepa

To my loving parents

నా తల్లిదండ్రులకు అంకితం

Acknowledgements

This PhD journey has been an amazing experience, which helped me evolve personally and professionally. I'm very glad to be able to work alongside with wonderful people. So, first I would like to thank Prof. Roman Krahne, my supervisor for giving me this opportunity. His constant support, scientific curiosity along with his approachable attitude makes him the best example for a mentor. I can, without a doubt, claim that I had the 'Super cool' supervisor anyone can ask for.

When you are new to the field, it is difficult to understand the concepts without proper teacher, to that I would like to thank Dr. Vincenzo Caligiuri for helping me understand the basic physics of MIMs and guiding me in the first year of my PhD. I would like to thank Dr.Denis Garoli for his support and encouragement during my PhD study. His insights on nanofabrication techniques and plasmonics helped me find solutions to the problems I faced during my course. I would also like to thank my co-advisor Prof. Maurizio Canepa from University of Genoa for the fruitful discussions we had over time. I would like to thank all the members of Optoelectronics group for insightful discussions and fun group lunches. I would like to extend my thanks to all the Cleanroom, Nanochemistry, Material Characterization facility and Nanoplasmonics Technicians and co-ordinators for their co-operation during this course. I would like to thank Iulia Manolache for the administrative support she provided when I initially arrived and also while attending summer schools and conferences. I extend my thanks to Alexander Weber-Bargioni, Stefano Cabrini, Archana Raja of Molecular Foundry, Berkeley labs for their support during my stay as an exchange student.

In these three years, I met people who are not only my colleagues but also became my close friends. I am very grateful to all the people who helped me when I first moved here and made it easy for me to sustain in a new country. I thank Dorwalettoo for all the coffee breaks and life lessons; Nayan ma (you may know her as 'Abinaya' :P) for her emotional

support and wonderful briyanis; Balaji for being that friend who will always be there for you; Drashti for the long walks and silly talks; Aniket for sharing his delicious food with us; Aswin for the playful banter. I convey my thanks to Nisarg, Sahitya, Seda, Nadia, Lyuye, Harshi, Aswini, Arya, Mai, Milan, Giulia(s), and all others who I couldn't mention here but have been a part of this wonderful journey. I want to also thank all the people who I met and spent time with, in the cleanroom.

Whatever I am today, I owe it to my parents, Mr. Sathibabu Pothuraju and Mrs. Ganeswari Pothuraju. I take this opportunity to convey my sincere gratitude to them for their love and care all these years. Abhishek Nalluri, I cannot thank you enough for your constant understanding and motivation in achieving this task. Me, my brother and cousins have always been a tight team helping each other whenever in need, I thank them as well for all those long calls and hearing me out. Finally, I would like to thank my Master's thesis supervisor, Prof. K.B.Jinesh of IIST who kindled my interest for science and encouraged me to pursue a career in research.

I thank and appreciate all the support and love shown by everyone.

Renuka Devi Pothuraju

PS: The quotes mentioned in this thesis are from the TV series "The Big Bang Theory".

Thesis Committee

- Prof. Tobias A.F. Koenig (Leibniz-Institut für Polymerforschung Dresden)

  email: koenig@ipfdd.de

- Prof. Nicolò Maccaferri (Umeå Unversitet)

  email: nicolo.maccaferri@umu.se

Table of Contents

List of Abbreviations and Acronyms 9

List of Symbols 12

Preface 14

1 INTRODUCTION 17

1.1 Surface Plasmons 17

1.1.1 Localized Surface plasmon Resonances 18

1.1.2 Surface plasmon polaritons 19

1.1.3 SPPs in Metal-Insulator-Metal system 24

1.1.4 Plasmonic metamaterials 26

1.2 Epsilon-Near-Zero materials 29

1.2.1 ENZ material properties 30

1.2.2 ENZ modes in Metal-Insulator-Metal (MIM) nanocavities 34

1.3 Conclusion 37

2 GRATING MIM FOR SPATIAL ENZ RESPONSE 38

2.1 Introduction 38

2.2 Characterization of a planar MIM 40

2.3 Grating MIM 45

2.3.1 Simulation 45

2.3.2 Fabrication and characterization 49

2.4 Conclusion 53

3 MIM MICROPILLARS: TALBOT LITHOGRAPHY AND CAVITY RESONANCE FOR PHOTOLUMINESCENCE ENHANCEMENT 54

3.1 Cavity and Dipole resonances in MIM pillars 54

3.2 Talbot lithography 59

3.3 PL enhancement in Molybdenum Disulfide monolayers 63

3.4 Conclusion 66

4 MIM NANOPILLARS: DIPOLE RESONANCES AND ANAPOLE-LIKE MODES 67

4.1 Dipole modes in MIM nanopillars 67

4.2 Anapole-like modes 71

4.2.1 Introduction 71

4.2.2 Results and discussions 73

4.3 Conclusion 76

5 NANOPOROUS METAL FILMS 77

5.1 Introduction 77

5.2 Fabrication 78

5.3 Characterization 79

5.4 Conclusion 83

6 CONCLUSION AND OUTLOOK 84

APPENDIX

SIMULATION, FABRICATION AND CHARACTERIZATION TECHNIQUES 86

A.1 Lumerical FDTD Simulations 86

A.1.1 The Finite-Difference Time-Domain Method 86

A.1.2 Simulation environment and boundary settings 88

A.2 Fabrication Techniques 90

A.2.1 Electron Beam Evaporation 90

A.2.2 Photolithography 91

A.2.3 Electron beam Lithography 94

A.2.4 Reactive-ion Etching 98

A.3 Optical and Physical Characterization 99

A.3.1 Spectroscopic Ellipsometry 99

A.3.2 Scanning Electron Microscopy 101

A.3.3 Atomic Force Microscopy 104

REFERENCES 105

List of Abbreviations and Acronyms

Abs.	Absorbance
AFM	Atomic Force microscope
Ag	Silver
Al_2O_3	Aluminum Oxide
Au	Gold
CF_4	Carbon tetrafluoride
Cu	Copper
CVD	Chemical Vapour Deposition
DTL	Displacement Talbot Lithography
DUV	Deep Ultraviolet
EBL	Electron Beam Lithography
ED	Electric Dipole
EDX	Energy Dispersive X-Ray Analysis
EF	Enhancement Factor
EMA	Effective Medium Approximation
EMNZ	ε-μ-Near Zero
ENZ	Epsilon-Near-Zero
EUV	Extreme Ultraviolet
FDTD	Finite Difference Time Domain
$FeCl_3$	Ferric Chloride
hBN	Boron Nitride
HMM	Hyperbolic Metamaterials
HRTEM	High Resolution Transmission Electron Microscopy
IC	Integrated Circuits
IMI	Insulator-Metal-Insulator
IPA	Isopropanol
Ir	Iridium
LSPR	Localized Surface Plasmon Resonances

MD	Magnetic Dipole
MIBK	Methyl isobutyl ketone
MIM	Metal-Insulator-Metal
MIMIM	Metal-Insulator-Metal-Insulator-Metal
MNZ	Mu-Near-Zero
MoS_2	Molybdenum Disulfide
MSE	Mean Squared Error
Ni	Nickel
NIR	Near Infrared
NPF	Nanoporous film
NPM	Nanoporous Metals
NZI	Near-Zero-Index
Pd	Palladium
PDMS	Polydimethylsiloxane
PDOS	Photonic Density of States
PL	Photoluminescence
PML	Perfectly Matched Layer
PMMA	Polymethyl methacrylate
Pt	Platinum
PVD	Physical Vapour Deposition
Refl.	Reflectance
Rh-6G	Rhodamine 6G
RIE	Reactive Ion Etching
SEF	Surface Enhanced Fluorescence
SEM	Scanning electron microscope
SERS	Surface Enhanced Raman Scattering
SF_6	Sulphur hexafluoride
$SiCl_4$	Silicon tetrachloride
SMM	Scattering Matrix Method

SPCE	Surface Plasmon Enhanced Coupled Emission
SPEA	Surface Plasmon Enhanced Absorption
SPM	Scanning Probe Microscopy
SPP	Surface Plasmon Polariton
SPR	Surface Plasmon Resonances
TCO	Transparent Conductive Oxides
TD	Toroidal Dipole
TE	Transverse Electric
TEM	Transmission Electron Microscopy
TM	Transverse Magnetic
TMDC	Transition Metal Dichalcogenide
Trans.	Transmittance
UV	Ultraviolet

List of Symbols

c	Velocity of light in vacuum
D	Diameter
E	Electric field
e	Electron charge
H	Magnetic field
k_0	Wave vector in vacuum
k_i	Wave vector in medium, i = x, y, z gives the propagation direction
k_m, k_d	Wave vectors in metal and dielectric respectively
k	Wave number
m	Electron mass
μ	Permeability of medium
n	Electron density
n	Refractive index
n_0	linear refractive index
n_2	Kerr non-linearity
n_d	Refractive index of dielectric nanoparticle
P	Periodicity
t_d	Thickness of the dielectric (or insulator) layer
V_g	Group velocity
V_p	Phase velocity
Z_T	Talbot length
β	Propagation constant in the medium
δ_m, δ_d	Penetration depth of light in metal and dielectric respectively
ε_0	Free space permittivity
ε_m, ε_d	Dielectric permittivity of metal and dielectric respectively
ε', ε''	Real and imaginary part of permittivity

θ_r , θ_i	Angles of refraction and incidence respectively
λ	Wavelength
λ_r	Resonance wavelength of the cavity
λ_{SPP}	Wavelength of Surface Plasmon Polariton
λ_0	Wavelength of light in vacuum
Υ	Damping constant
ϕ_p	Angle of polarization
Φ_t , ϕ_b	Phase shift due to the top and bottom metal respectively in a MIM
$\chi^{(3)}$	Third-order nonlinear susceptibility
ω	Frequency
ω_p	Plasma frequency
ω_{SP}	Surface plasmon frequency
ψ and Δ	Ellipsometric data parameters

Preface

The whole world is dying of curiosity!!

- Sheldon Cooper

Plasmonic metamaterials provide a great deal of optical tunability and interesting phenomena in terms of light-matter interaction. Metal-Insulator-Metal (MIM) nanocavities are one of the most versatile systems for nano light confinement and waveguiding. These cavities exhibit Epsilon-Near-Zero (ENZ) modes, which can be used in conjunction with emitters to improve their optical properties. MIM nanocavities have been extensively studied, but when the cavities are confined in one more direction, the behavior changes. The purpose of this study is to investigate the effect of lateral micro/nano structuring on the optical properties of these cavities.

The planar cavities are used in multiple applications, and among them are color filters, due to their selective wavelength transmission. We design a 'Grating MIM' and determine the minimum pixel size that can provide spatial ENZ response along with color filtering. The ENZ cavity resonance present in planar cavities persist as long as the lateral dimensions are larger than 1μm. When the diameters of the cavities are further reduced to hundreds of nanometers, electric (ED) and magnetic dipole (MD) modes appear in the visible spectral range. These modes are present also in micron size structures, but they fall in infrared region. Recently all-dielectric nanostructures have gained popularity to manifest these dipole modes, as they do not show the dissipative losses present in metallic nanostructures and support toroidal dipoles (TD) when the geometry is optimized. The destructive interference of any two of these dipole modes, which cancels the far-field radiation, results in a non-radiative mode known as anapole. However, this

necessitates the use of materials with a high refractive index (n), typically $n \geq 3$. In low index materials like Alumina (Al_2O_3), the MIM configuration provides the necessary field confinement and can excite these modes. The existence of ENZ cavity modes in MIM micropillars, as well as dipole and anapole-like modes in MIM nanopillars, is demonstrated experimentally.

Photolithography (for micropillars) and electron-beam lithography (for nanopillars) were used to fabricate, and ellipsometry to characterize the samples. To facilitate cost-effective, large area fabrication, Talbot lithography technique was exploited to get smaller feature sizes (<200nm) using standard photolithography setup. In addition, a lithography-free, dry-synthesis technique was explored to produce nanoporous metal films and their properties as plasmonic nanomaterials were examined.

Thesis outline

This thesis is composed of five chapters discussing systematically the effects of lateral structuring the MIM nanocavities from micro to nanometer range.

Chapter 1: Introduction presents the basic concepts required to understand the experimental and numerical results reported in the later chapters. It covers the fundamental physics of plasmonics, metal-insulator-metal structure and ENZ materials. The state of art in these fields related to this thesis is also presented.

Chapter 2: Grating MIM provides the details of study on a structured metal-insulator-metal nanocavity to obtain spatial ENZ response. Starting with a brief characterization of MIM, the structured cavity (Grating MIM) is analyzed with simulations and experiments.

Chapter 3: MIM Micropillars is dedicated to study the properties of MIMs when patterned as micro and nano pillar structures. A cost-effective lithographic technique called Talbot lithography is investigated to obtain nanometer sized features. Samples made using this technique were employed to enhance Photoluminescence of Molybdenum Disulfide monolayers

Chapter 4: MIM Nanopillars discusses resonant modes in pillars with diameters that are in sub-micron range. The electric and magnetic dipole modes present in these pillars are experimentally demonstrated. We use MIM nanopillars to observe and excite collective modes that could be 'Anapole-like' in Al_2O_3 by taking advantage of the field confinement provided by metal-insulator-metal configuration.

Chapter 5: Nanoporous Metal films presents a simple dry-synthesis process to produce nanoporous metal films. The fabrication process along with the morphological characterization and purity analysis is discussed. Surface enhanced Raman spectroscopy is performed on one of these films to check the plasmonic activity.

A **Thesis Conclusion** is provided at the end to summarize the results of all the chapters.

An **APPENDIX** details all the simulation, fabrication and characterizations tools used in the course of this thesis.

Happy Reading! 😊

Chapter 1

INTRODUCTION

Who's ready for some science??

- Leonard Hofstadter

This chapter is dedicated to outline the basic concepts of plasmonic resonances and Epsilon Near Zero (ENZ) materials. Physical insight along with fundamental mathematical understanding for exciting different plasmonic resonances is discussed. The properties of ENZ materials and their applications in the field of optics are presented. Plasmonic and ENZ modes in the context of metal-insulator-metal nanocavities are reviewed.

1.1 Surface Plasmons: Fundamentals and theory

Plasmonics is the field of study of the interaction of electromagnetic radiation (i.e., light) with the free electrons in conductive materials. These interactions result in resonances called Surface Plasmon Resonances (SPR). During the past decades, these resonances have been extensively investigated as they provide near-field enhancement[1] and light confinement at nanoscale[2]. Due to these unique properties, surface plasmons have been successfully implemented in optical waveguides[3], photovoltaic devices[4], surface-enhanced spectroscopies[5], biosensors[6], optical data storage[7]and many more[8].

Surface plasmons are longitudinal charge density fluctuations that result from coupling of incident electromagnetic radiation with the electron oscillations in a conductor. Surface plasmons exhibit shorter wavelengths than photons in free space, which can be used for miniaturization of photonic technology[9]. Surface plasmons can be mainly categorized into two types, Localized Surface Plasmon Resonances (LSPRs) and Surface Plasmon Polaritons (SPPs). Localized Surface Plasmon Resonances are non-propagating electron oscillations

that are observed in nanoparticles. Surface Plasmon Polaritons are propagating evanescent waves that propagate along the interface between a metal and dielectric layer.

1.1.1 Localized Surface Plasmon Resonances

Localized Surface Plasmon Resonances (LSPRs) are non-propagating excitations which arise from the coupling of light to the charge density oscillations of metallic nanoparticles[10,11]. When light is incident on a nanoparticle with dimensions much less than the wavelength of light, the electric field polarizes the particle. This results in displacement of the electron cloud which leads to charge accumulation at the surface of the particle as shown in Fig.1.1. Due to the coulomb attraction between the displaced electron cloud and positively charged nuclei, a restoring force arises resulting in a resonant oscillation of the electron cloud[10]. So, there is no need of any momentum matching techniques to excite LSPRs, they occur naturally in nanoparticles.

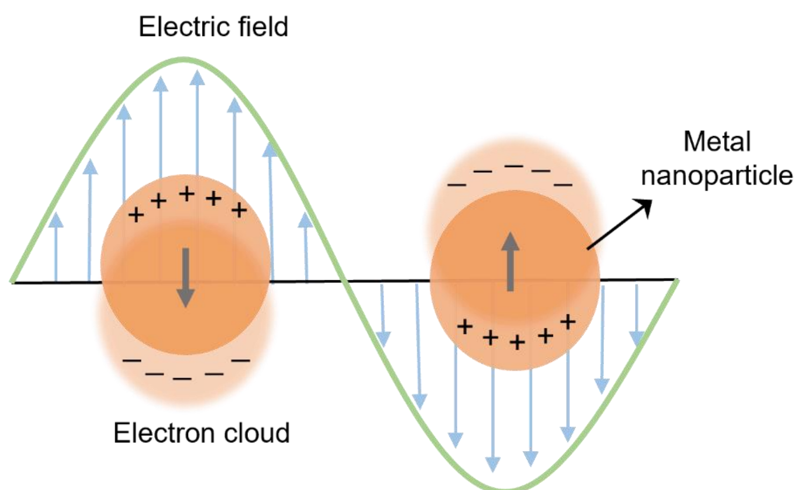

Figure 1.1: Localized Surface Plasmon Resonance. Schematic representation of interaction of metal nanoparticles with light.

Gold and silver nanoparticles exhibit bright colors as their resonances occur in visible spectrum[12,13]. The localized surface plasmon resonance response can be altered by changing the shape and size of the particle[13]. As the size of the nanoparticle increases, the distance between the charges at the interfaces increases, resulting in smaller restoring force and therefore smaller resonance frequency (longer wavelengths). The

resonance can be spectrally shifted by changing the aspect ratio of the particle and it can also be broadened by increasing the particle volume[13,14].

1.1.2 Surface Plasmon Polaritons

Polaritons are quasiparticles resulting from coupling between an electromagnetic radiation and an elementary excitation. Surface Plasmon Polaritons (SPPs) are result of coupling of surface plasmon with a photon[10]. SPPs are propagating electromagnetic resonant excitations which are excited by impinging photons at the interface between metal and dielectric. These excitations decay evanescently along the perpendicular direction to the interface. Figure-1.2 shows the illustration of SPP propagating along a metal-dielectric interface. λ_{SPP} is the wavelength of excited SPP, δ_m and δ_d are skin depth (decay length) of the fields in the metal and dielectric layers along the z-direction respectively.

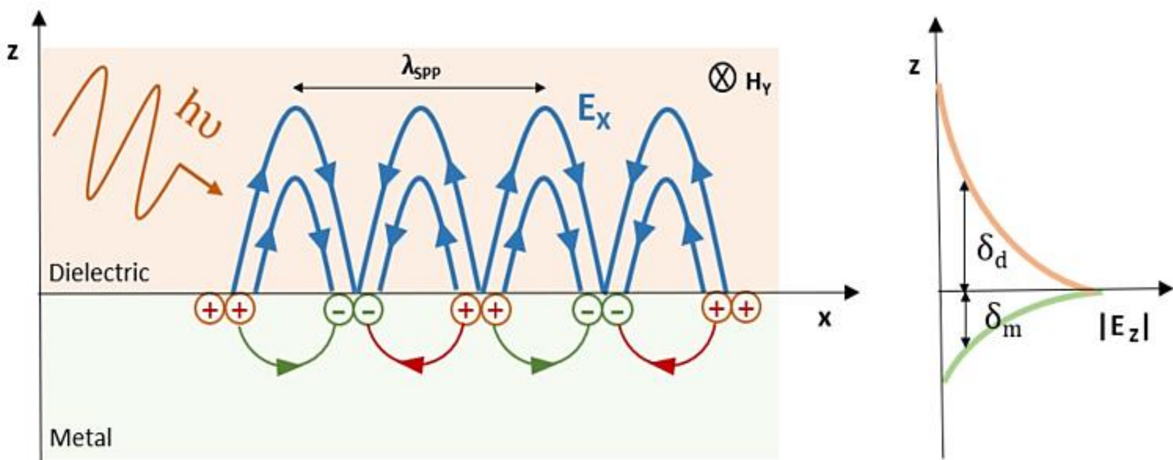

Figure 1.2: (a) Schematic of propagation of Surface Plasmon Polaritons along metal/dielectric interface. (b) Evanescently decaying electric field along z-direction.

The physical properties of SPPs along metal/dielectric interface can be investigated by applying Maxwell's equations[15]. Traverse Magnetic (TM) polarized light has the electric field components of the incident light in plane of incidence and magnetic components are perpendicular to the plane of incidence. For deriving the dispersion relation of SPP, the fundamental wave equation of TM modes in a waveguide is considered and is given as

$$\frac{\partial^2 H_y}{\partial z^2} + (k_0^2 - \beta^2)H_y = 0 \quad (1.1)$$

where $k_0 = \frac{\omega}{c}$, wave vector of propagating wave in vacuum and $\beta = k_x$ is the propagation constant in the medium.

The basic geometry realized to model SPP propagation is an interface between two homogeneous, non-absorbing half spaces: (i) z > 0, medium which is dielectric with positive real dielectric function ε_d (ω) and (ii) z < 0, metallic medium with negative real dielectric function ε_m (ω). The incident TM wave (as shown in the Fig.1.2) has two electric field components in x and z- directions and only one magnetic field component in y - direction. Applying the boundary conditions and analyzing the longitudinal component along z – direction, we get the following field components for z > 0.

$$H_{y,d}(z) = B\, e^{ik_x x}\, e^{-k_d z} \tag{1.2}$$

$$E_{x,d}(z) = i\, B\, \frac{1}{\omega \varepsilon_0 \varepsilon_d}\, k_d e^{ik_x x}\, e^{-k_d z} \tag{1.3}$$

$$E_{z,d}(z) = -A\, \frac{k_x}{\omega \varepsilon_0 \varepsilon_d}\, e^{i\beta x}\, e^{-k_d z} \tag{1.4}$$

For z < 0,

$$H_{y,m}(z) = A\, e^{ik_x x}\, e^{k_m z} \tag{1.5}$$

$$E_{x,m}(z) = -\, i\, A\, \frac{1}{\omega \varepsilon_0 \varepsilon_m}\, k_m e^{i\beta x}\, e^{k_m z} \tag{1.6}$$

$$E_{z,m}(z) = -A\, \frac{k_x}{\omega \varepsilon_0 \varepsilon_m}\, e^{i\beta x}\, e^{k_m z} \tag{1.7}$$

where A,B are Fresnel coefficients[10]. The component of wave vectors perpendicular to the interface can be written as $k_d = k_{z,d}$ and $k_m = k_{z,m}$. To satisfy the boundary conditions and continuity of the fields in the two media,

$$H_{y,d}(z = 0) = H_{y,m}(z = 0) \tag{1.8}$$

$$E_{x,d}(z = 0) = E_{x,m}(z = 0) \tag{1.9}$$

This implies, A must be equal to B, which results in

$$\frac{k_d}{k_m} = -\frac{\varepsilon_d}{\varepsilon_m} \tag{1.10}$$

The confinement of the wave to the surface is only possible if Re (ε_m) < 0 when $\varepsilon_d > 0$, i.e for materials with opposites signs of the real part of permittivity, typically an interface between conductor and insulator. To satisfy the wave equation 1.1,

$$k_m^2 = k_x^2 - k_0^2\,\varepsilon_m \tag{1.11}$$

$$k_d^2 = k_x^2 - k_0^2\,\varepsilon_d \tag{1.12}$$

Combining equations 1.11 and 1.12, we get the dispersion relation (relation between frequency and wave vector) of SPP wave travelling at the interface of metal and insulator and is given by

$$k_x = k_{SPP} = k_0\sqrt{\frac{\varepsilon_d\,\varepsilon_m}{\varepsilon_d+\varepsilon_m}} \tag{1.13}$$

One can derive the similar solution for TE (Transverse Electric) polarized waves, but after applying boundary conditions, none of the solutions satisfy the surface conditions. This proves that no surface modes can exist with TE modes, which demonstrates that SPP modes only exist for TM polarization. A more detailed derivation of the wave equation (eq. 1.1) can be found in the book: "Optical electronics" by Amnon Yariv[16], and the dispersion relations of SPP modes can be found in the book "Plasmonics: Fundamentals and Applications" by S. Maier[10].

Dispersion Relation

For the surface plasmons to exist at the interface according to the dispersion relation in eq. 1.13, the following condition must be satisfied,

$$\frac{\varepsilon_d\,\varepsilon_m}{\varepsilon_d+\varepsilon_m} > 0 \tag{1.14}$$

$$\Rightarrow since\ \ \varepsilon_d\,\varepsilon_m < 0 \Rightarrow \varepsilon_d + \varepsilon_m < 0 \tag{1.15}$$

Since the $\varepsilon_m < 0$ and $\varepsilon_d > 0$, eq. 1.14 also requires that the absolute value of permittivity of the metal must be greater than that of the dielectric.

$$|\varepsilon_m| > |\varepsilon_d| \tag{1.16}$$

To further understand the properties of SPPs let's consider the dielectric function of the metal given by the Drude model[17] assuming negligible damping,

$$\varepsilon_m(\omega) = 1 - \frac{\omega_p^2}{\omega^2} \tag{1.17}$$

where ω_p is bulk plasma frequency of the metal, which is given by,

$$\omega_p = \sqrt{\frac{\mathrm{n}e^2}{\varepsilon_0 m}} \tag{1.18}$$

where n is the electron density, e is the electron charge, ε_0 is the free space permittivity and m is the electron mass. At plasma frequency, the dielectric function changes sign from negative to positive and the real part of the dielectric function falls to zero.

Substituting eq. 1.15 in the dispersion relation eq. 1.13 gives

$$k_{SPP} = k_0 \sqrt{\frac{\varepsilon_d\,\varepsilon_m}{\varepsilon_d + \varepsilon_m}} = k_0 \sqrt{\frac{\varepsilon_d(\omega^2 - \omega_p^2)}{(\varepsilon_d + 1)\omega^2 - \omega_p^2}} \tag{1.19}$$

We notice that $k_{SPP} > k_0$, which implies that the phase velocity of the surface wave given by $\upsilon_{SPP} = \omega/k_{SPP}$ is smaller than the velocity of light, $c = \omega/k_0$. Therefore, direct excitation of surface plasmons is not possible as the momentum of light is smaller than the surface plasmon momentum. This momentum mismatch must be compensated and can be done by multiple techniques like using a Kretschmann prism[18], grating coupler[19] or other techniques[20,21].

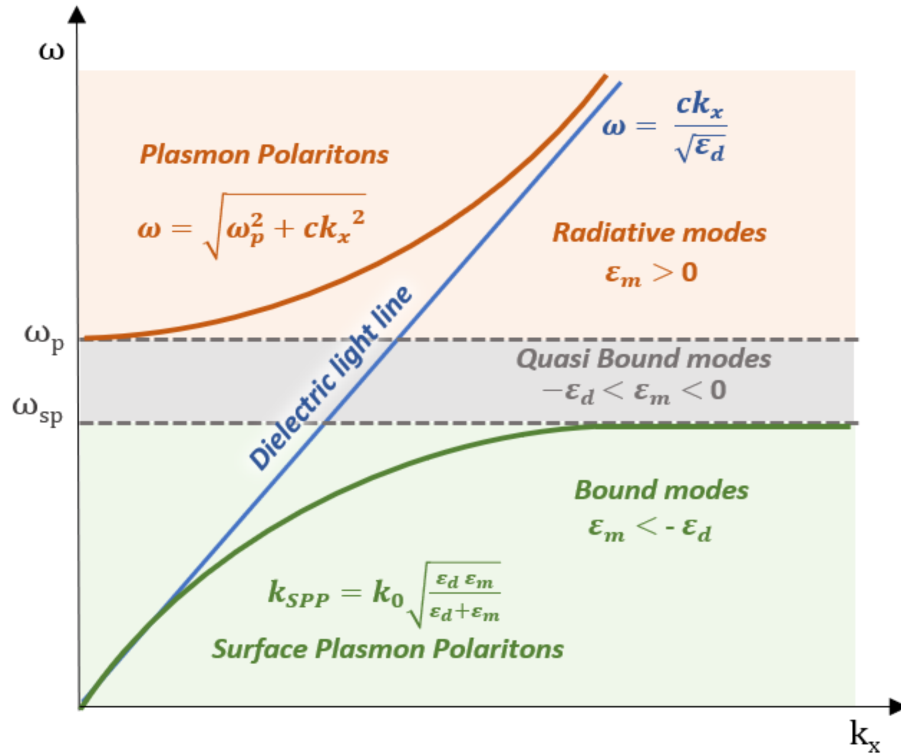

Figure 1.3: Dispersion relation of Surface plasmons for metal/dielectric interface showing different types of modes that can be excited according to the value of ε_m.

Figure-1.3 shows the surface plasmon dispersion relation which can be divided into three regimes, (i) Radiative modes (ii) Quasi-bound modes and (iii) Bound modes, depending on the values of ε_m and ε_d (according to the condition in eq 1.14). For frequencies higher than the plasma frequency ($\omega > \omega_p$), $|k_{SPP}| < |k|$ and hence transverse waves can propagate in the metal as plasmon polaritons. This is called the transparency regime of the metals. $|k_{SPP}| > |k|$ is the bound mode regime which is located to the right of the dielectric light line. Due to their bound nature, SPPs fall into this regime. The frequency gap between and radiative and bound modes, has purely imaginative k_{SPP} and prohibits any kind of propagation.

Two asymptotes can be observed from the figure and can be approximated as

$$\omega \rightarrow 0 \qquad k_{SPP} \rightarrow k_0\sqrt{\varepsilon_d}$$

$$k_{spp} \rightarrow 0 \qquad \omega \rightarrow \frac{\omega_p}{\sqrt{\varepsilon_d+1}} = \omega_{SP} \tag{1.20}$$

where ω_{SP} is the surface plasmon frequency. Since $\varepsilon_d > 0$, the surface plasmon frequency is always smaller than plasma frequency, ω_P. This implies that SPPs can only be excited at frequencies below plasma frequency. Generally, for most metals, ω_P is of the order of 1000-2000 THz, and falls in the ultraviolet spectral region[22]. Therefore, it is possible to excite the surface plasmons with visible light. However as previously mentioned, it is not possible to excite the SPPs directly as there is a momentum mismatch which requires using a phase matching technique. For small wave vectors, the dispersion relation of k_{SPP} follows the wave vector of the light line. The charges in the metal follow the displacement field and act as a perfect reflector. As the wave vector increases, the free charges in the metal are not able to oscillate at such high frequencies resulting in the deviation from the light line. This deviation increases and then saturates as surface plasmon frequency. As k_{SPP} tends to infinity the phase velocity of the surface wave that is inversely proportional to the wave vector approaches zero. This results in an electrostatic-like behavior at the interface known as surface plasmon.

Surface plasmon polaritons are orthogonally confined to the interface's plane and decay evanescently in both sides of the interface[10]. The decay length of the fields perpendicular to the interface is the skin depth (or penetration depth) and is given by,

$$\delta_d = \frac{1}{k_0}\left|\frac{\varepsilon_d+\varepsilon_m}{\varepsilon_d^2}\right|^{\frac{1}{2}} \qquad \delta_m = \frac{1}{k_0}\left|\frac{\varepsilon_d+\varepsilon_m}{\varepsilon_m^2}\right|^{\frac{1}{2}} \tag{1.21}$$

where δ_d and δ_m are skin depths of SPP in dielectric and metal layers respectively. Due to the condition, $|\varepsilon_m| > |\varepsilon_d|$ for the excitation of SPPs, the skin depth of SPPs inside the dielectrics is larger than in the metals. So, the electric field travels longer inside the dielectric. Generally, for a wide range of frequencies, the field decays in the order of about 20nm in metals while in dielectrics the decay is one or two orders larger in magnitude.

1.1.3 SPPs in Metal-Insulator-Metal system

When we consider multilayer systems, two main geometries are thoroughly studied, (i) Insulator-Metal-Insulator (IMI) and (ii)Metal-Insulator-Metal (MIM) both known as plasmonic waveguides[23]. In these configurations, when the separation between the layers

is comparable to the penetration depth, the SPP modes at the two interfaces couple with each other giving rise to bound SPP modes. Consider three homogenous, lossless and isotropic layers in MIM configuration as shown in Fig.1.4 (a). The top and bottom metal

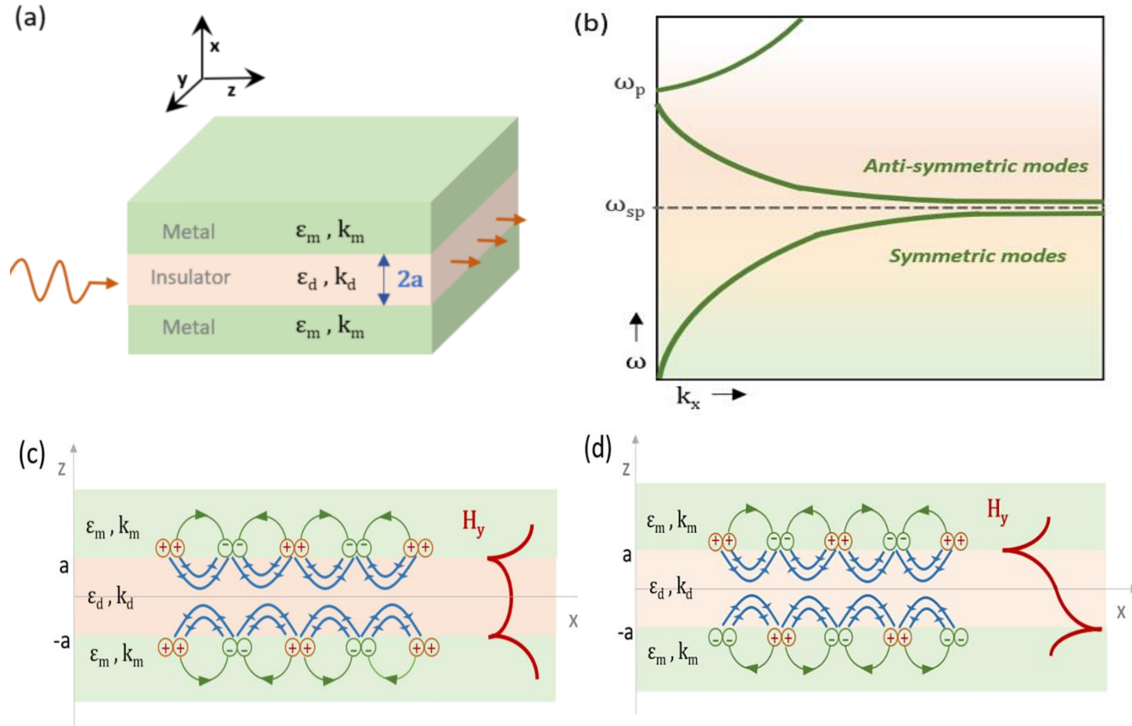

Figure 1.4: (a) Schematic representation of MIM structure (b) Dispersion relation of MIM Charge distribution at the interfaces along with the magnetic field profiles for (c) Symmetric mode (d) Anti-symmmetric mode

layers are made of same material, making it a symmetric MIM. A dielectric (ε_d, k_d) slab of thickness 2a is sandwiched between two identical metal (ε_m, k_m) layers.

A TM polarized light is incident in the z-direction as shown in the Fig.1.4 (a). If we apply the boundary conditions at the two interfaces and derive the dispersion relation, we get,

$$tanhk_d a = -\frac{k_d \varepsilon_m}{k_m \varepsilon_d} \tag{1.22}$$

$$cothk_d a = -\frac{k_d \varepsilon_m}{k_m \varepsilon_d} \tag{1.23}$$

Depending on the charge distributions and their oscillation at the interfaces, MIM can sustain Symmetric (odd) and Anti-symmetric (even) modes. For anti-symmetric modes, the dispersion curve exhibits a negative slope, leading to negative group velocity ($V_g=d\omega/dk$) but the phase velocity ($V_p=\omega/k$) is positive. As a result, this mode thus behaves as if it has a negative refractive index[24]. On the other hand, the symmetric SPP mode (below the surface plasmon resonance frequency) appears to have a positive refractive index, as its group and phase velocities are both positive. Apart from these modes, there are oscillatory modes which come into picture when the SPP propagation constant is imaginary. Complete derivation of the dispersion relation and different modes can be found in the book "Waves in metamaterials" by Solymar et al.[23] The above described SPP discussion applies to MIMs acting as optical waveguide. In this thesis, we use MIM as a photonic nanocavity[25], which will be discussed in Section 1.2.2.

1.1.4 Plasmonic Metamaterials

Light-matter interaction has been a stimulating field of research for a long time. These studies have helped in engineering materials with desired optical properties which are not naturally available and are called as "Metamaterials". Metamaterials are periodically or randomly distributed artificial structures with size and periods much smaller than the incident wavelength. From macroscopic point of view, these elements can be assembled to form a homogenous material with effective material properties[26]. Since early 2000s, plasmonics and metamaterials have been extensively studied in multiple fields like optics[27,28], material science[29,30], biosciences[31], nanoscience[32] etc. These two fields initially advanced along their own individual trajectories, and once they reached the optical regime, researchers started to combine the effects. The interplay between plasmonic and metamaterials has given rise to unprecedented concepts and innovative discoveries. With plasmonic metamaterials, researchers were able to demonstrate phenomena like negative refractive index[33], artificial magnetism[34,35], zero permittivity[36], zero permeability[37], subwavelength field confinement[38], surface enhanced effects[39] and strong chirality[40]. Advances in nanofabrication made it easy for these materials to find

applications in biomedical imaging[41], energy harvesting[42], nanosurgery[43], photocatalysis[44] and data storage[45].

The three main mechanisms utilized to enhance or manipulate the electromagnetic fields using plasmonic structures are (i) Near Field enhancement, (ii) Absorption and (iii) Scattering. When plasmonic structures are irradiated with incident light, the localized surface plasmons generate additional electric field around them. If some molecules are in the vicinity of these plasmonic nanostructures, their Raman signal and fluorescence can be enhanced. These effects are called Surface Enhanced Raman Scattering (SERS) and Surface Enhanced Fluorescence (SEF)[46-48]. Raman signal enhancements of factors 10^8 - 10^{15} have been reported allowing us to detect single molecules[48,49]. The radiative and non-radiative decay of fluorophores can be improved along their quantum yield and lifetime using plasmonic metamaterials[50].

Strong absorption by plasmonic metamaterials can be manifested due to the excitation of the surface plasmons. This in turn increases the localized energy absorption which also generates heat (thermal energy). This phenomenon is mainly used in the biological fields[52,53]. By Irradiating plasmonic nanoparticles at their resonance wavelength, a local temperature rise can be achieved which is used for a wide range of therapies. These photothermal effects are used to generate high thermal contrast to kill/damage targeted cells. Targeted delivery can be achieved by surface functionalization (e.g., biomolecule and ligand conjugations). In 2019, Rastinehad et al., used Au-silica nanoshells in photothermal treatment of prostate cancer in human[54]. They reported near infrared (NIR) absorption of Au-silica nanoshells and high-efficient results in clinical trial. This demonstrated the first safe and efficient photothermal cancer treatment in human.

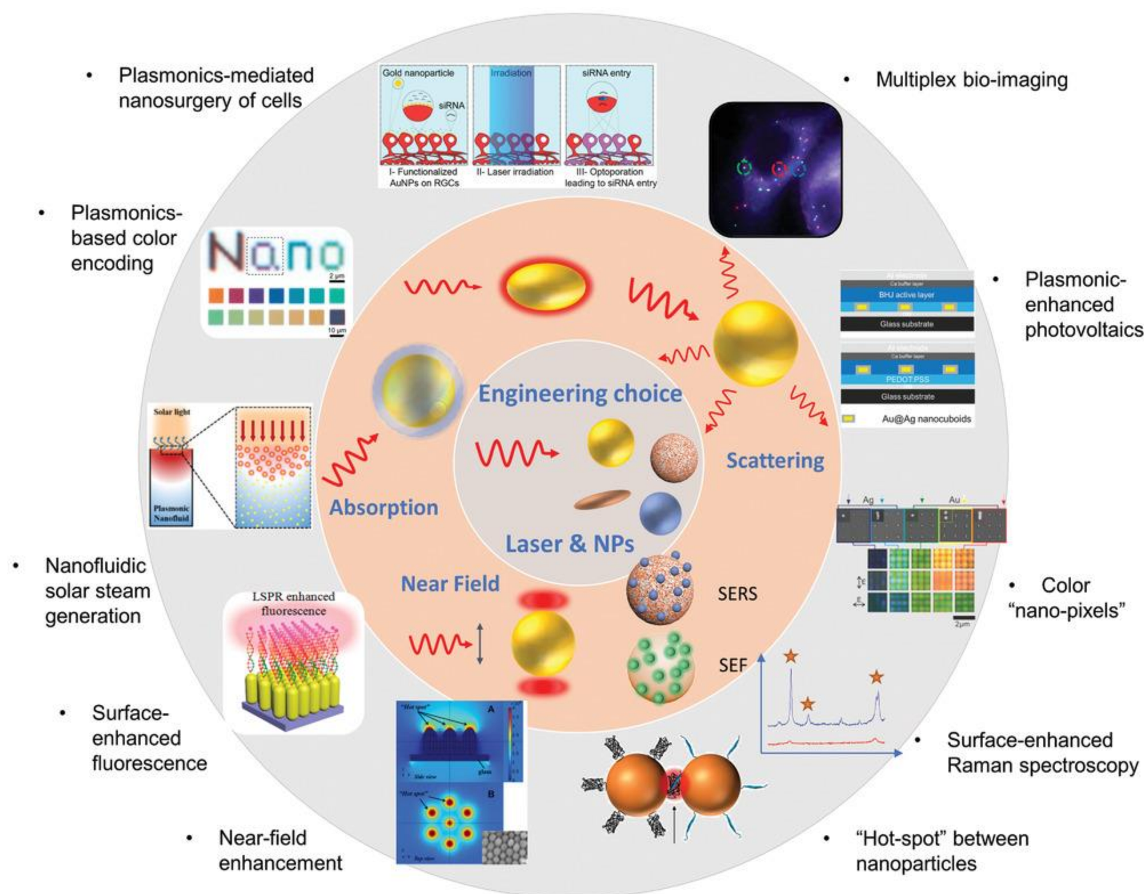

Figure 1.5: Applications of plasmonics. The center circle shows the geometry and composition of the plasmonic nanostructures and illumination source based on wavelength, pulse width, etc. as an engineering choice. The second inner circle (orange) represents the phenomena used for applications namely absorption, scattering, and near field. The outer circle (grey) shows different applications based on the specific phenomena according to the engineering choices. *Reproduced with permission from Ref. 51. Copyright ©2020 Wiley-VCH GmbH*

Plasmonics has found its place in energy technology as well. Solar energy is one of the most abundant sources of energy available. There is significant amount of research going on with remarkable advancements in this field[4,55,56]. But still for implementing these developed approaches, lack of perfect light absorption and conversion efficiency are limiting factors. Using plasmonic metamaterials, the energy conversion devices have shown to improve the performance. Due to the scattering effects of plasmonic nanoparticles, the light path in the semiconductors materials can be elongated, resulting

in higher absorption[56]. When plasmonic structures are implanted on a semiconductor substrate, they tend to scatter light into the substrate, which in turn are reflected from the bottom side of the device. The plasmonic structures can again reflect this light back into the absorption layer increasing the effective path length of the light[51]. This phenomenon has been used to enhance the performance of standard solar cells[57,58], organic solar cells[59,60] and dye-sensitized solar cells[61] giving rise to a new category of solar cells called plasmonic solar cells[62].

Photonic integrated circuits (ICs) are the next most technological advanced circuits in research[63,64]. Given that the semiconductor technology reaching its limits, researchers are turning towards photonic ICs to design new photonic based data storage and computing devices. One of the main limitations of optical devices is the diffraction limit and using plasmonic devices one can overcome this limit. Optical color filters based on plasmonics are already in use[65,66]. Plasmonic metamaterials enable color-encoding at the nanoscale which can be controlled through the illumination conditions and the, plasmonic properties of the materials used[67,68]. Plasmonics-based 'nanopixels' have been demonstrated increasing the resolution over those of conventional imaging techniques[69,70].

1.2 Epsilon-Near-Zero materials

Near-Zero-Index (NZI) materials are class of materials which exhibit zero refractive index values at certain frequencies[71-73]. They display interesting phenomena like enhanced non-linear optical interactions[74], emission tailoring[75], static light[76], super coupling[77,78], photon tunneling[79,80]. The refractive index (n) is square root of product of permeability (μ) and permittivity (ε), therefore one can achieve NZI condition in three ways (i) Mu-Near-Zero (MNZ), (ii) Epsilon-Near-Zero (ENZ) and (iii) ε-μ-Near Zero (EMNZ). As we are interested in optical regime and most of the materials have weak magnetic responses in this frequency regime, the relative permeability is regarded as a constant, $\mu = 1$. It is therefore easier to engineer the permittivity value to near zero than the permeability[81]. This can be achieved by implementing appropriate structural design[82,83].

ENZ materials have been thoroughly under research in the past twenty years[81,84,85]. There are mainly four mechanisms to achieve ENZ behavior, (i) by using metal-dielectric alternate layers to create an effective medium[86,87], (ii) by using free electrons in semiconductors at bulk plasma frequency[88,89], (iii) by using metallic waveguides to confine electromagnetic energy below a certain cutoff frequency[90,91], (iv) by exploiting the photonic Dirac cone in Brillouin zone[92,93]. The first two approaches are mostly used because it is easy to engineer - multilayer photonic structures and, semiconductors and transparent conductive oxides (TCO) by doping to obtain ENZ behavior. Generally, ENZ condition requires only the real part of the permittivity to be zero. However, if the imaginary part (which represents the losses in the material) is not sufficiently low, it cannot be used for few applications. So, there should be a trade-off while designing ENZ materials.

1.2.1. ENZ material properties

ENZ materials are those whose permittivity values are approaching zero, which in general the occurs when the real part of permittivity changes from positive value to negative value at a certain wavelength[84]. This happens naturally in few materials, for example silver films with thicknesses less than 40nm exhibits an ENZ mode at 326nm[94]. For a material to be a loss-free ENZ material, it should have both the real and imaginary parts of the permittivity as zero. However, it is difficult to achieve such a lossless behavior, therefore the ENZ materials designed are generally lossy due to a small positive imaginary part of permittivity[95]. ENZ materials show interesting properties[81,86] which have led to some novel phenomena, and we shall discuss few of them in this section.

Low wavenumber and long wavelength

When we consider the relation,

$$n = \sqrt{\mu\varepsilon} \tag{1.24}$$

as mentioned earlier in optical regime for most materials, μ is considered as 1. This implies

$$n = \sqrt{\varepsilon} \tag{1.25}$$

A material's wavenumber, k is generally defined as

$$k = \frac{2\pi}{\lambda} = k_0 n = k_0\sqrt{\varepsilon}\,, \qquad \lambda = \frac{\lambda_0}{n} \tag{1.26}$$

where k_0 is vacuum wavenumber, λ and λ_0 are wavelength inside the material and vacuum respectively. According to these equations, as permittivity tends to zero, the wavenumber of the propagating wave approaches zero and the wavelength increases. This indicates negligible spatial dispersion, and the wave stretches and exhibits longer wavelength even for higher frequency radiation. Fig.1.6 illustrates how an electromagnetic wave changes in a medium with high permittivity and near-zero permittivity[96].

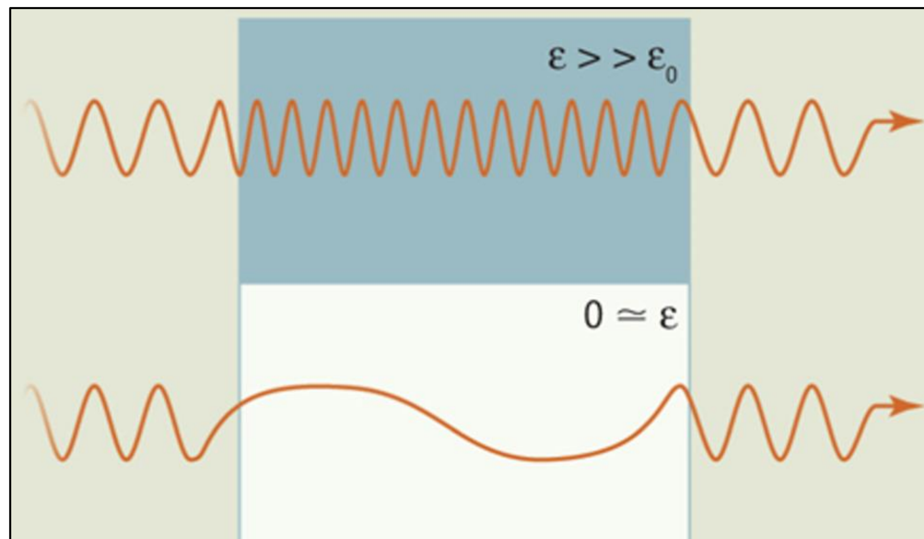

Figure 1.6: Illustration of propagation of electromagnetic wave in high permittivity medium and ENZ medium. *Reproduced with permission from Ref 96. Copyright © 2013, American Association for the Advancement of Science.*

Phase conservation and directionality

When we consider an EM wave expressed as $\bar{E} = E_0 e^{i\bar{k}.\bar{r}}$, the wavenumber is near zero for an ENZ material. This implies that the EM wave phase remains constant while propagating through the medium[97]. This constant phase can be used to achieve enhanced superradiance in antenna designs[98-100]. When dipoles are placed at arbitrary locations in

an ENZ medium, they oscillate with identical phases in the entire region. This results in constructive interference of radiation field which results in an in-phase enhancement.

The constant phase has been utilized to shape the radiation wavefront[101] and directive emission[75]. It is better explained by using Fresnel's formula which is used to determine the angle of refraction at a boundary.

$$\theta_r = \arcsin\left(\sqrt{\varepsilon\mu}\, sin\theta_i\right) \tag{1.27}$$

Where θ_r and θ_i are angles of refraction and incidence respectively. For an ENZ material, θ_r is always zero, which means when a wave propagates from ENZ medium at any incidence angle to other medium, it leaves perpendicular to the boundary. This results in a directional wave leaving the ENZ medium.

Optical non-linearity Enhancement

Non-linear optical effects can be observed due to non-linear properties of the optical polarizability, for example, when an intense laser beam is incident on a material [84,102]. The refractive index of a non-linear material according to the Kerr effect[103] is given as

$$n = n_0 + n_2|E|^2 \tag{1.28}$$

Where n_0 is the linear refractive index, $|E|^2$ is the electric field amplitude, n_2 is Kerr non-linearity, which is expressed as,

$$n_2 = \frac{4}{4n_0^2\varepsilon_0 c}\chi^{(3)} \tag{1.29}$$

$\chi^{(3)}$ is third-order nonlinear susceptibility. As we see, to enhance the non-linear behavior of the material, n_2 must be increased which is inversely proportional to n_0. With ENZ material, n_0 is nearly zero which can be utilized to realize and enhance non-linearity in materials[104,105].

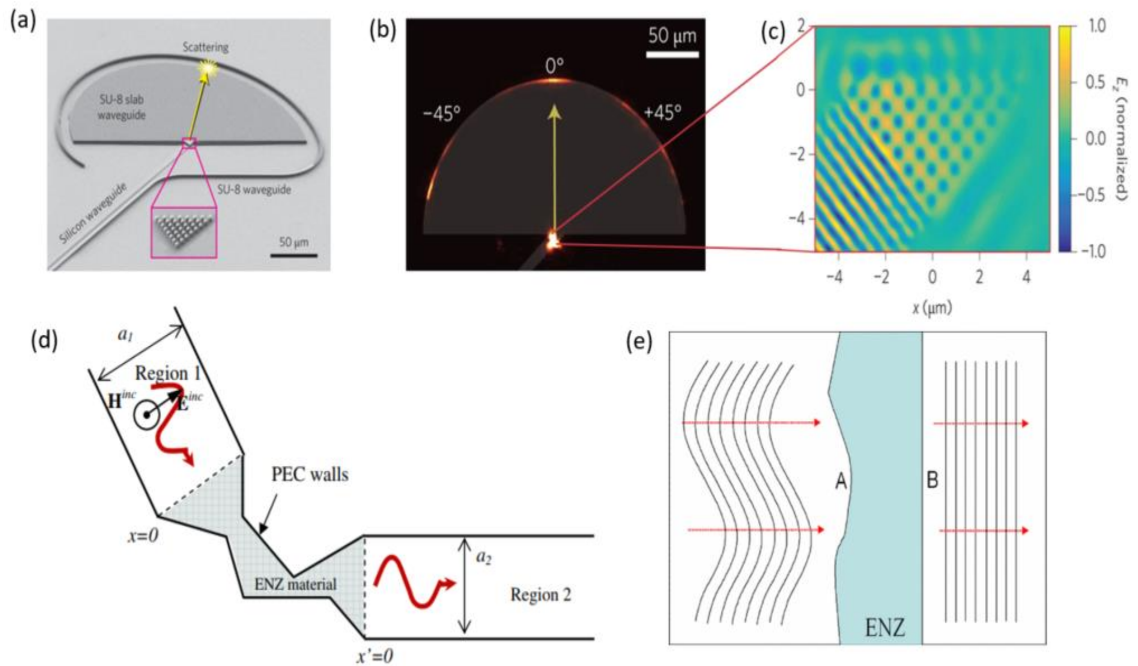

Figure 1.7: Properties of ENZ materials. (a-c) Demonstration of first on-chip NZI metamaterial in the optical regime by Yang Li et al[97]. (a) Scanning electron microscope (SEM) image of the metamaterial prism placed at the end of a silicon waveguide with an SU-8 slab guiding region. Inset shows the prism made of right triangular array of pillars constituting of Silicon and gold. When excited through the silicon waveguide from the bottom left, the light enters the prism and refracts at an angle determined by momentum matching. As the excitation wavelength approaches the zero-index region, the phase velocity tends to infinity and a nearly uniform phase is achieved within the prism which results in emission leaving in the direction normal to the interface instead of at an arbitrary angle. (b) Near-infrared microscope image of the prism showing the refracted beam, which propagates normal to the interface between the prism and the SU-8 slab waveguide. (c) Simulated out-of-plane electric field in the prism illustrating the nearly constant spatial phase distribution. (a-c) *Reproduced with permission from Ref. 97. Copyright © 2015, Nature Publishing Group* (d) Schematic of geometry of a 2D waveguide structure with an ENZ material section proposed by M.Silveirinha et al. to demonstrate the super coupling with ENZ materials. When a monochromatic EM wave with ENZ frequency of the region enters through the waveguide, almost all the electric field and the power flow are squeezed into the narrow channel without any loss causing perfect transmission. *Reproduced with permission from Ref. 79. Copyright © 2006 The American Physical Society* (e) Representation of wavefront shaping using ENZ medium. A curved phase front impinging on an ENZ material leaves the medium with planar phase front which is conformal to the exit surface. *Reproduced with permission from Ref. 101.*

Field Confinement and Supercoupling

While applying boundary conditions between two media, the continuity of the normal components of electric field is maintained. But when wave propagates through an ENZ material, strong discontinuities are induced imposing high values of electric fields inside the ENZ medium. This results in local field confinement and enhancement. Such effects have been reported with both natural ENZ materials and metamaterials[79,106,107].

The constant phase property of the ENZ materials helps in transmitting the EM waves in arbitrary shapes without any losses. It has been theoretically implemented to achieve super-coupling between two waveguides by M.Silveirinha et al. They demonstrated that EM waves can be squeezed and tunneled through subwavelength channels of ENZ medium without any losses[79]. They also proposed an analytical formula which indicated that narrower the waveguide[106], higher the energy tunneled into the waveguide, which was later demonstrated experimentally as well[107]. This can be imagined intuitively that when a wave enters an ENZ medium, its wavelength becomes infinite making it difficult to pursue the width of the waveguide, and simply tunnels through.

All these properties along with several other fascinating phenomena makes ENZ materials an important field of study. In this thesis, we deal with the ENZ nature of metal-insulator-metal nanocavities. The next section will provide the details about the previous works done by my colleagues within the Optoelectronics group which laid the foundation to the work in this thesis.

1.2.2 ENZ modes in Metal-Insulator-Metal nanocavities

Naturally occurring ENZ materials can be used in certain wavelength regimes and engineering them to produce a tunable ENZ response is challenging. Using Metal-Insulator-Metal (MIM) nanocavities, ENZ resonances which can be tuned across the entire visible region just by varying the insulator thickness has been successfully demonstrated by V.Caligiuri et al[108-111]. When MIMs with layer thicknesses of tens of nanometers are incident with light, they support Fabry-Perot cavity modes which manifests an ENZ

resonance. To better understand the physics behind the ENZ behavior, a semi-classical approach was used to analyze the resonant tunnelling ENZ modes in MIM nanocavities[87].

In this model, the square of the refractive index is considered as the optical potential and propagation of photons through this potential is described by the Helmholtz equation. An analytical formula to predict the ENZ resonances in MIM was derived and given as,

$$\varepsilon_{eff,MIM} = \varepsilon_{\infty} - \frac{\omega_p^2}{(\omega^2 + i\gamma\omega)} + \frac{\alpha_1 \omega_{MIM}^2}{(\omega^2 - \omega_{0,MIM_{-1}}^2 - i\gamma_{MIM_{-1}}\omega)} + \frac{\alpha_2 \omega_{MIM}^2}{\left(\omega^2 - \omega_{0,MIM_{-2}}^2 - i\gamma_{MIM_{-2}}\omega\right)} \quad (1.30)$$

where ϒ is the damping constant of Ag (0.021 eV), ε_{∞} = 6.8 eV and ω_P = 2200 THz (corresponding to 9.1 eV for Ag). All the other parameters are derived from experimentally measured and fitted ellipsometric data. There are two eigenmodes, one symmetric and one antisymmetric for a single MIM. These modes can also be identified as peaks in transmission and absorbance and as minima in reflectance as shown in Fig.1.8(a,c). The results agree with the Scattering Matrix Method (SMM) and Finite Element Method (COMSOL) simulations.

Further coupling between two MIM systems, called MIMIM which is composed of MIM with extra insulator and metal layers on top of it is explained and experimentally demonstrated[108]. The same quantum analysis has been applied to the MIMIM system to determine the ENZ behavior. The hybridization of the modes was experimentally demonstrated by changing one of the dielectric layer thicknesses. The coupling strength can be determined by the middle metal layer. Thinner the metal layer, higher the coupling.

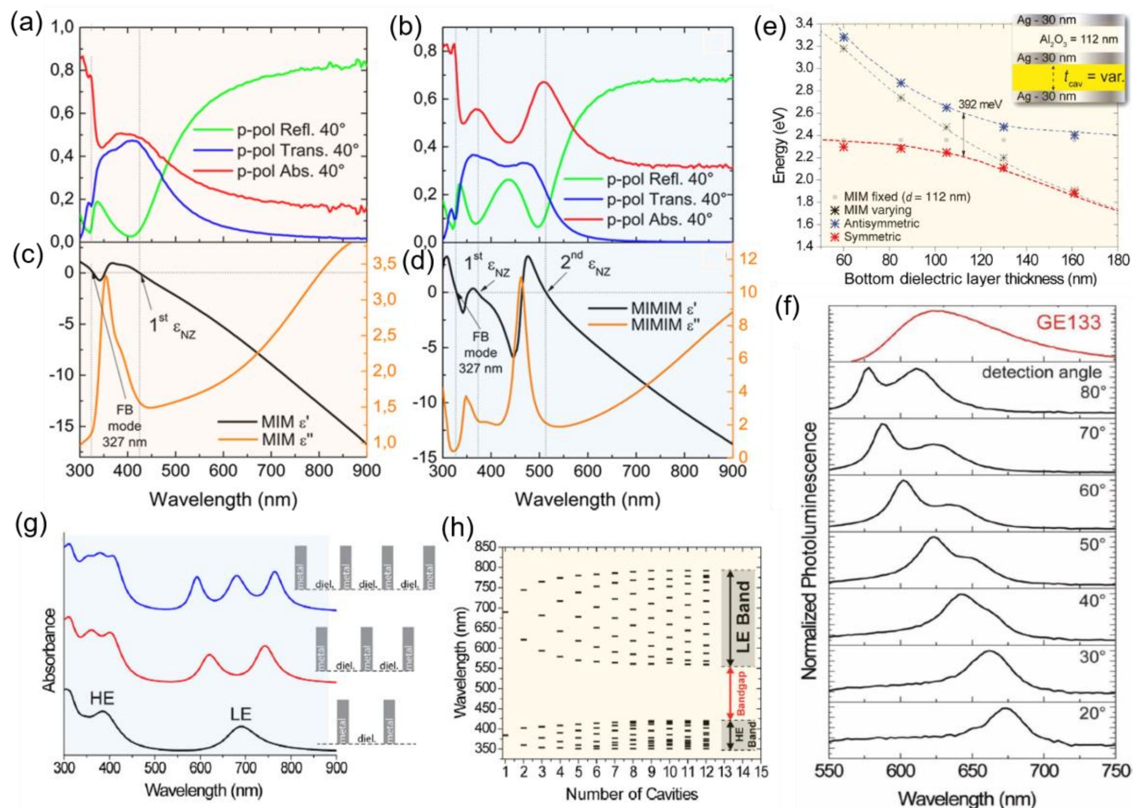

Figure 1.8: ENZ modes in MIM and multilayer nanocavities. (a-d) Optical response of MIM and MIMIM systems. (a,b) Transmittance (blue), reflectance (green), and absorbance (red) of (a) the MIM and (b) MIMIM systems. (c,d) Ellipsometrically measured real (black) and imaginary (orange) parts of the dielectric permittivity of the (c) MIM and (d) MIMIM. *Reproduced with permission from Ref. 110. Copyright © 2018 American Chemical Society* (e) Illustration of hybridization in MIMIM system. The typical anticrossing due to coupling can be seen in a MIMIM system where the metal layers are 30 nm Ag and top dielectric layer is 112 nm Al_2O_3 and the thickness of the bottom dielectric layer is varied. Experimentally measured data is shown by stars and the simulated dispersion via SMM is shown by dashed lines. The gray markers (experimental) and lines (SMM simulations) show the case of noninteracting cavities. *Reproduced from Ref. 108.* (f) Angle dependence of spontaneous emission of a dye on cavity dispersion. Photoluminescence as a function of the detection angle (black curves), and the emission of the dye (red curve). *Reproduced with permission from Ref. 109.* Copyright *© 2019 WILEY-VCH Verlag GmbH & Co. KGaA, Weinheim.* (g,h) Illustration of the hybridization of ENZ resonances when several MIM cavities are placed over one another. g) Symmetric (Low Energy, LE) and Anti-symmetric (High Energy, HE) modes in absorbance of stacks with one,two and three dielectric layers. h) Resonance frequencies for up to 12 cavity layers giving rise to HE and LE bands that are separated by a bandgap. *Reproduced from Ref. 111.*

An angle and polarization dependent spontaneous emission of a dye was demonstrated using MIM nanocavities[109]. A dye was placed inside the cavity and the emission followed the cavity dispersion. An enhancement in the emission due to the Purcell effect was also demonstrated[110]. In this case, fluorophore was coated on the MIMIM cavity whose ENZ resonance wavelengths matched the absorption and emission of the fluorophores. There was an enhancement in the emission due to the increase in the Photonic Density of States (PDOS) of the fluorophore.

As we increase the number of insulator and metal layers in the MIM stack, the ENZ resonances hybridize further resulting in a band like response. A one-dimensional ENZ crystal was designed and experimentally demonstrated using this concept[111]. An analogy between atomic orbitals and MIM nanocavities was used to describe the ENZ crystal. Using this Kronig-Penny model, a boundary between ENZ crystal and hyperbolic metamaterials (HMM) in terms of dielectric thickness has been established. The classic Effective Medium Approximation (EMA) theory which is generally used to explain HMM permittivity fails to explain the ENZ crystals. With the Kronig-Penny model, it is possible to explain the cavity modes that are sustained in thicker dielectric cavity layers providing a novel perspective on these structures.

1.3 Conclusion

This chapter presented the basic concepts of plasmonics and ENZ materials to understand their importance in research and applications. The conditions for exciting plasmonic modes are studied in detail with appropriate derivations. NZI and ENZ material properties were explained and their use in different optical applications was reviewed. ENZ modes in MIM nanocavities which offers the basic concept for this thesis were reviewed in detail.

Chapter 2

Grating MIM for spatial ENZ response

What are ya doing there? Working on a new plan to catch the Road Runner?

Leonard Hofstadter

In this chapter, we use a structured metal-insulator-metal nanocavity called, 'Grating MIM' to obtain spatial ENZ response. We start with brief characterization of MIM and then explore the grating MIM properties. The optical response of grating MIM is studied with Finite Difference Time Domain (FDTD) simulations and experiments.

2.1. Introduction

Color filters are one of the most important devices in displays[112], digital photography[113], printing technologies[114] etc. Conventional color filters were built based on colorant pigments which absorb light to produce desired color. These chemical filters suffer from general environmental conditions like heat, moisture, reactions with components in air etc., and continuous exposure to UV light degrades their performance[115]. Structural color filters which utilize the light interaction with nanostructures to produce different colors are one of the promising technologies to produce better resolution and stable color filters[66,116-118].

Depending on the mode of operation, color filters can be transmissive filters or reflective filters. As the name suggests, transmissive filters transmit only specific wavelengths and block the remaining spectral range and reflective filters absorb few wavelengths and

reflect desirable wavelengths. Fabry Perot filters based on Metal-Insulator-Metal (MIM) cavities are of great importance due to their straight-forward fabrication and response[119-121].

MIM cavities work in transmission mode, where the two metal layers act as semi-transparent mirrors with the dielectric spacer in between. When light is incident on a MIM cavity, it is partially reflected and partially transmitted into the cavity through the top metal layer. The light is reflected from the bottom metal layer, and it travels back and forth in the dielectric region. Due to the Fabry-Perot nature of the MIM cavity, only few specific wavelengths can be trapped inside the cavity and eventually transmitted through. The resonance wavelength which determines the transmission of the MIM is given as,

$$2\left(\frac{2\pi}{\lambda_r}\right)n_d t_d + \phi_t + \phi_b = 2\pi m \tag{2.1}$$

where λ_r is the resonance wavelength of the cavity, n_d and t_d are refractive index and thickness of the dielectric layer respectively. ϕ_t , ϕ_b are the phase shift due to the top and bottom metal layers and m is the order of the cavity mode[120]. The phase condition given by eq. (2.1) must be satisfied for the cavity to achieve resonance. When the total phase accumulated while being reflected by top and bottom layers is an integral multiple of 2π, the light is transmitted through the cavity. This is the physical phenomena that leads to transmission through MIM nanocavities which can be employed as color filters.

As we seen from eq. (2.1), the spectral response can be easily tuned by dielectric thickness. These filters have been recently employed in cameras by using dielectric layers of different thicknesses for different spectral response and creating an image pixel[122]. It has been reported that the MIM cavity resonances manifest Epsilon-Near-Zero (ENZ) modes[108-111]. Multi-ENZ response can be achieved by stacking layers of dielectric and metals on a MIM nanocavity. But the ENZ modes obtained in this fashion, are coupled modes. Similar to designing a pixel, we propose a design in which the bottom metal layer of the MIM is patterned to obtain spatial ENZ response, which we call 'Grating MIM'. We also determine the spatial resolution of this response with simulations and experiments.

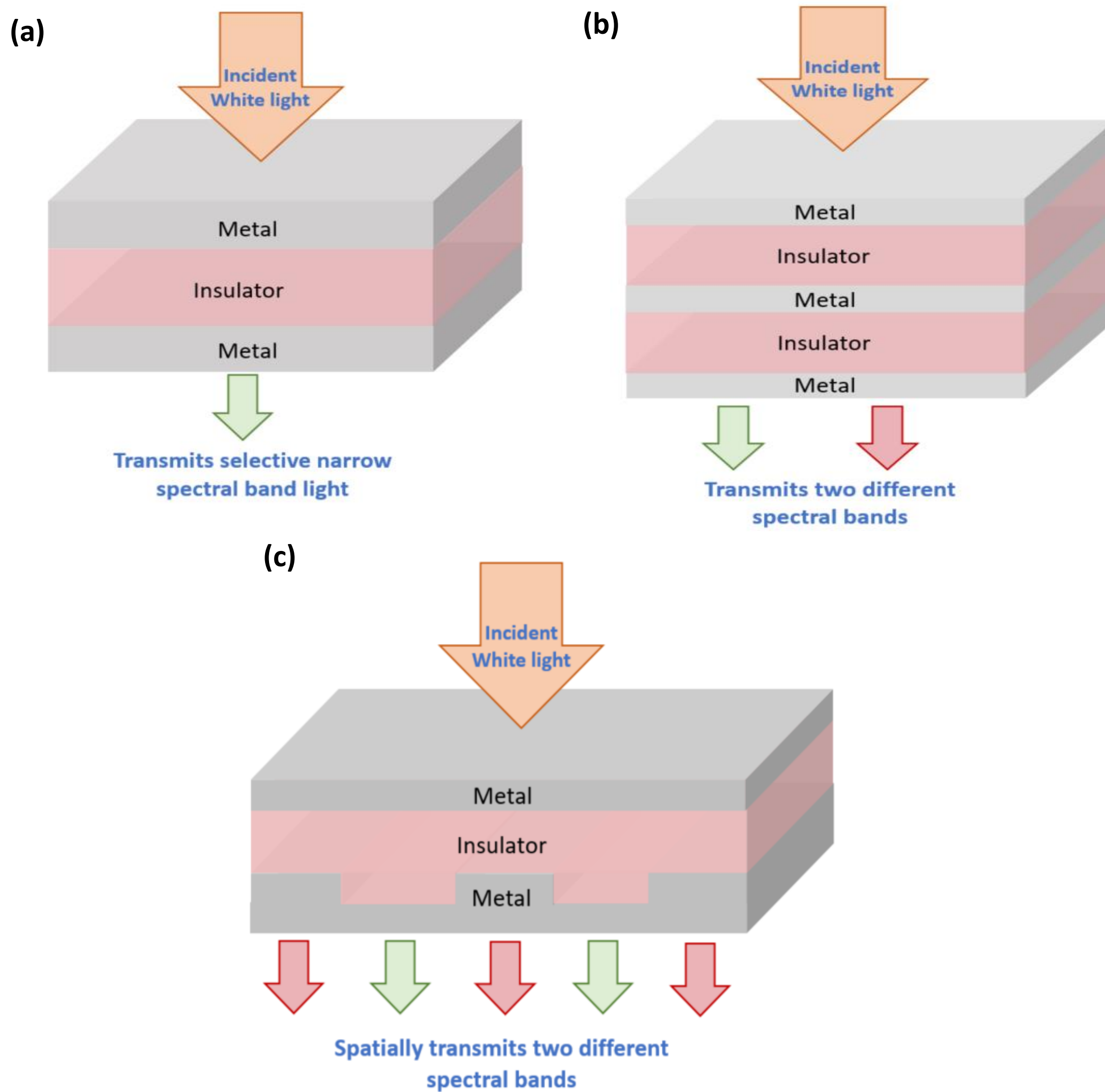

Figure 2.1: Schematic of (a) MIM (b) MIMIM and (c) Grating MIM configurations acting as transmissive filters

2.2. Characterization of a MIM

Before studying the properties of grating MIMs, it is essential to understand the steps involved in characterizing a simple MIM which is infinitely long in X and Y-directions compared to the nanometric dimensions in the Z-direction (termed as 'Planar MIM' in this thesis). We will start by briefly describing the characterization procedure of a planar MIM and MIMIM with thin layers of metal and insulator on a glass substrate.

Simulations

In the previous referred studies[108-111], Finite Element Method based Simulations using COMSOL Multiphysics software were used. Here, we use FDTD based Lumerical software to derive the simulation data. The results obtained are in agreement with the reported COMSOL simulations. Silver (Ag) and Aluminum oxide (Al_2O_3) were used as the metal and insulator layers for this study as they are ideal for exciting ENZ response in the visible spectral regime. The optical constants (n,k) of all the materials used were imported into the library from experimentally measured data. A plane wave source with p-polarization light is used to for illumination along the z-direction. Perfectly Matched Layer (PML) was imposed as the boundary condition and a minimum mesh size of 2.5nm was used. 2D field monitors were used to record the transmittance and reflectance data along with the field profiles.

The thickness of the metal layers should be thin enough, so that the light can penetrate through the top layer into the MIM, and the bottom layer should be able to couple the light out of the MIM. The maximum thickness of Silver that can be used to facilitate this process is 40nm. The thicknesses we chose for the study are 20nm of the Ag layers and 120nm of Al_2O_3. Fig.2.2(a,b) shows the design parameters used for the simulation of a MIM and MIMIM nanocavities. The optical properties, transmittance (Trans.), reflectance (Refl.) and absorbance (Abs.) were plotted for MIM and MIMIM systems as shown in Fig.2.2(c) and Fig.2.2(d) respectively. The absorbance is taken as (1 – Trans. – Refl.). The peaks in transmittance and absorbance and the minima in reflectance represents the cavity modes of the MIM. In the case of MIMIM, we see two different cavity modes arising from the coupling between the top and bottom individual MIM systems. The electric field profiles along the XZ plane at the resonance wavelengths, 531nm for MIM and 485nm for MIMIM shows the field confinement inside the dielectric layers. As the thickness of the dielectric layer increases, the resonance wavelengths red shift and anti-symmetric modes at lower wavelengths can be seen in the blue spectral region.

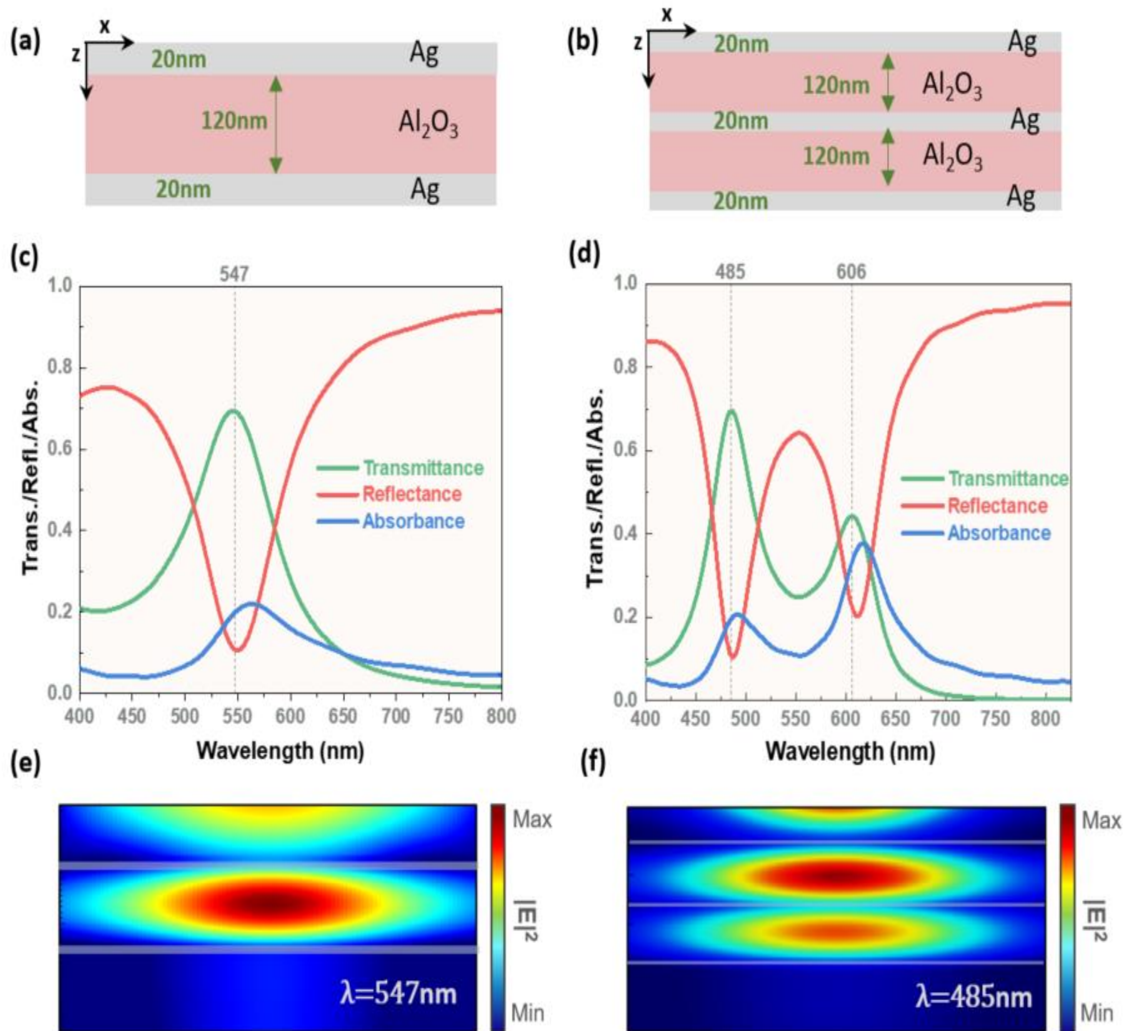

Figure 2.2: Simulation results of MIM and MIMIM. 2D-Model and design parameters of (a) MIM (b) MIMIM along XZ-plane. Transmittance (green) Reflectance (red), and Absorbance (blue) of (c) MIM and (d) MIMIM. Simulated norm of the electric field calculated as $(E_x^2+ E_z^2)^{1/2}$ of (e) MIM and (f) MIMIM at corresponding resonance wavelengths.

Experimental Demonstration

The fabrication of planar MIM structures is a straight-forward process which involves multi-layer deposition using e-beam evaporator. 20nm of Ag and 120nm of Al_2O_3 were deposited at a rate of 0.3 A°/s and 0.5 A°/s respectively. The deposition is done at 10^{-6} Torr pressure with e-beam source of 8KW power. The thickness of the layers was later checked using ellipsometry and were found to be accurate with ±2nm error.

Ellipsometry can be used to retrieve information on each single layer of a multilayer structure to give the measured ψ and Δ. This data can also be used to perceive the multilayer structure as a single effective unknown material to model and derive the optical constants. Fig.2.3(a,b) shows the measured ψ and Δ of the fabricated planar MIM for different angles of incidence. To derive the permittivity of the MIM, we must fit the data to a model constructed with different oscillators. Generally, we start with a CAUCHY oscillator and fit the measured data by point-by-point fitting at a single angle until we obtain a Mean Squared Error (MSE) value of less than 30[111]. Then we build a generic oscillator model consisting of Lorentz and Gaussian oscillators (typical for MIM response) to get a perfect fit as shown in Fig.2.3(c). Using the Kramers-Kronig consistency, this model provides reliable values of real (ε') and imaginary (ε'') part of permittivity of the MIM as a single homogenous medium[123]. Fig.2.3(d,e) shows the permittivity values obtained for the fabricated MIM after fitting at all the measured angles. We can see two zero-crossings of ε'. The first zero crossing has a high imaginary part, which indicates a lossy mode that is not optimal to generate a resonant response. The second crossing at 544nm however has a low imaginary value and therefore corresponds to a cavity mode of the MIM with the ENZ condition.

The plots in Fig.2.3 (f) and (g) shows the transmittance and reflectance data of the fabricated MIM. Absorbance can also be calculated from this data. The measured data shows the angle and polarization dependence of the ENZ cavity mode. The p-polarized light (TM mode) excites the plasmonic response of the metal (Refer to Section.1.1.2). Thus, the p-polarized mode constitutes the cavity and plasmonic responses of the MIM giving it a plasmonic-photonic kind of nature. While with the s-polarized incident light, only the photonic cavity modes are excited, which is pure photonic mode. The energy dissipation in the form of cavity and plasmonic losses results in shift to lower energy (higher wavelength) and slightly broader response with p-polarized light than with s-polarization. However, both p- and s-polarized modes correspond to ENZ dispersion and produce cavity resonances, and these resonances are angle dependent as shown in Fig.2.3(f,g).

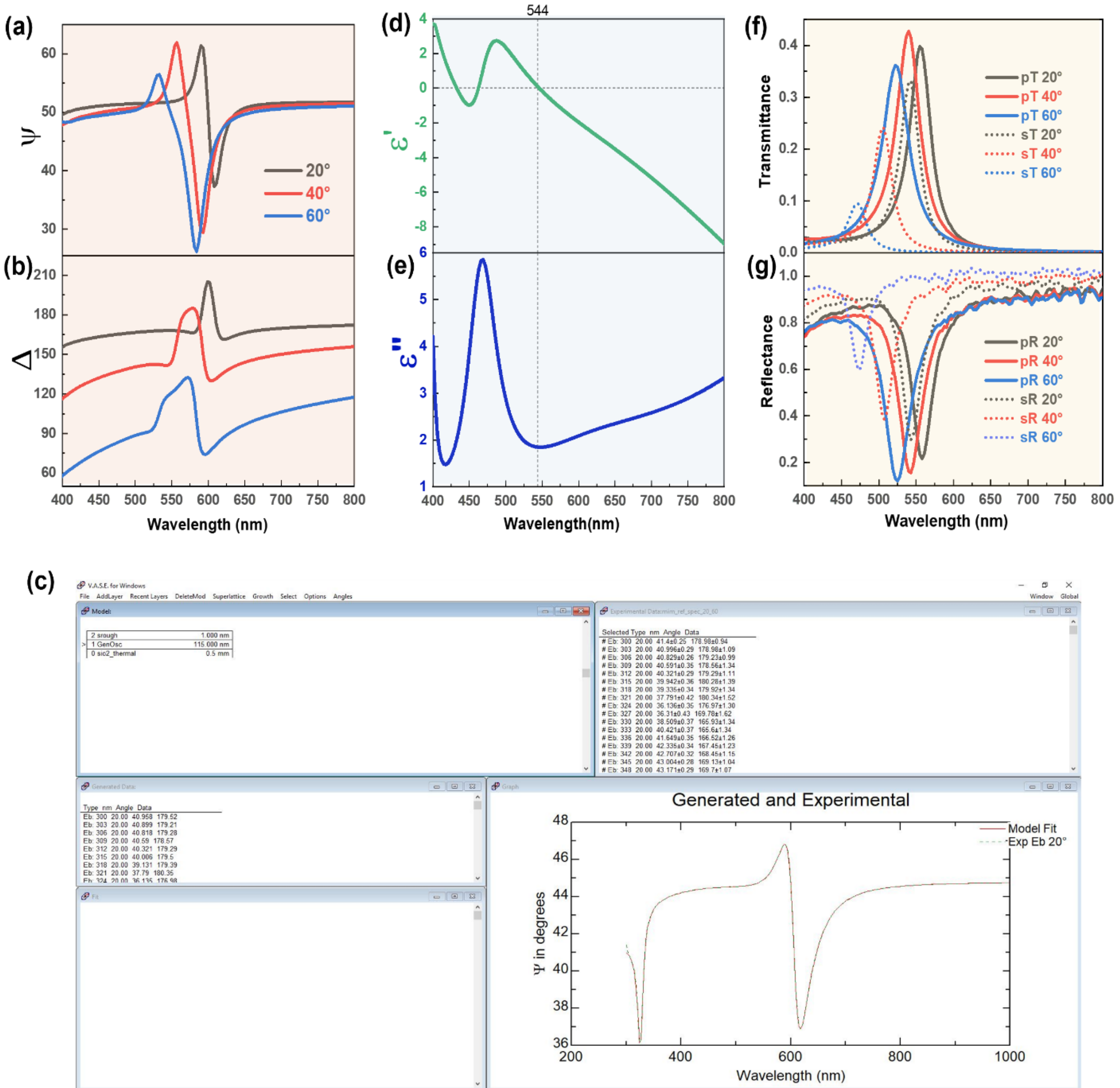

Figure 2.3: Experimental results of MIM with 20nm Ag and 120nm Al_2O_3. (a,b) Ellipsometrically measured ψ and Δ at three different angular incidence. (c) Typical model fit window used in WVASE software of ellipsometer to extract real (ε') and imaginary (ε'') part of permittivity. (d,e) ε', ε'' of MIM after proper fitting at all angles. (f) Transmittance and (g) Reflectance measured at different angles with different p- and s- polarized light.

2.3. Grating MIM

2.3.1. Simulation

A grating MIM with grating periodicity 4µm and height 15nm is modelled to study the optical response as shown in Fig.2.4 (a). Two MIMs with dielectric thicknesses of 125nm and 110nm are incorporated in this design. Transmittance plot as shown in Fig.2.4(b) shows two peaks in transmittance which correspond to two different planar MIMs. The resonance peak at lower wavelength i.e., 531nm is corresponding to the MIM with smaller dielectric thickness (110nm) and the higher wavelength peak at 607nm corresponds to the MIM with dielectric thickness 125nm. These exactly align with the planar MIM features. The electric field profiles (Fig.2.4(c)) at the two resonance wavelengths shows that only a single cavity resonance exists at one specific wavelength. This proves the spatial dependence of the ENZ response (transmittance) at different resonance wavelengths for white light incidence.

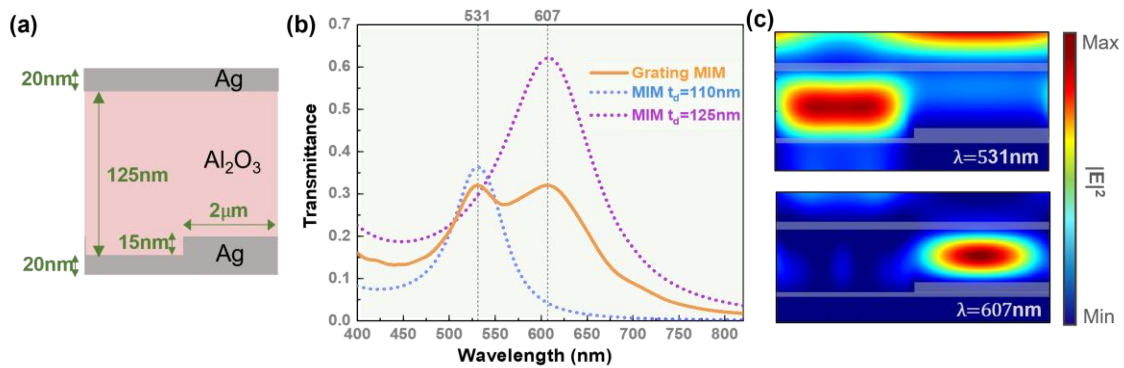

Figure 2.4: Simulation results of grating MIM. (a) Model and design parameters set for simulation. (b) Transmittance of Grating MIM (orange) along with corresponding planar MIMs of insulator thicknesses 110nm (blue) and 125nm (violet). (c) Simulated norm of the electric field calculated as $(E_x^2+ E_z^2)^{1/2}$ at two resonance wavelengths 531nm and 607nm.

This configuration when used in transmissive mode is limited in terms of the grating height, which in turn limits the difference between the resonance wavelengths of the two modes (76nm in above mentioned case). This is due to the fact that the thicknesses of the

top and bottom metal layers should be less than 40nm for the light to enter the structure and couple out of the structure. But if we consider reflective mode of operation, we can overcome this limitation and opt for larger grating heights. This helps in increasing the spectral difference between the two modes.

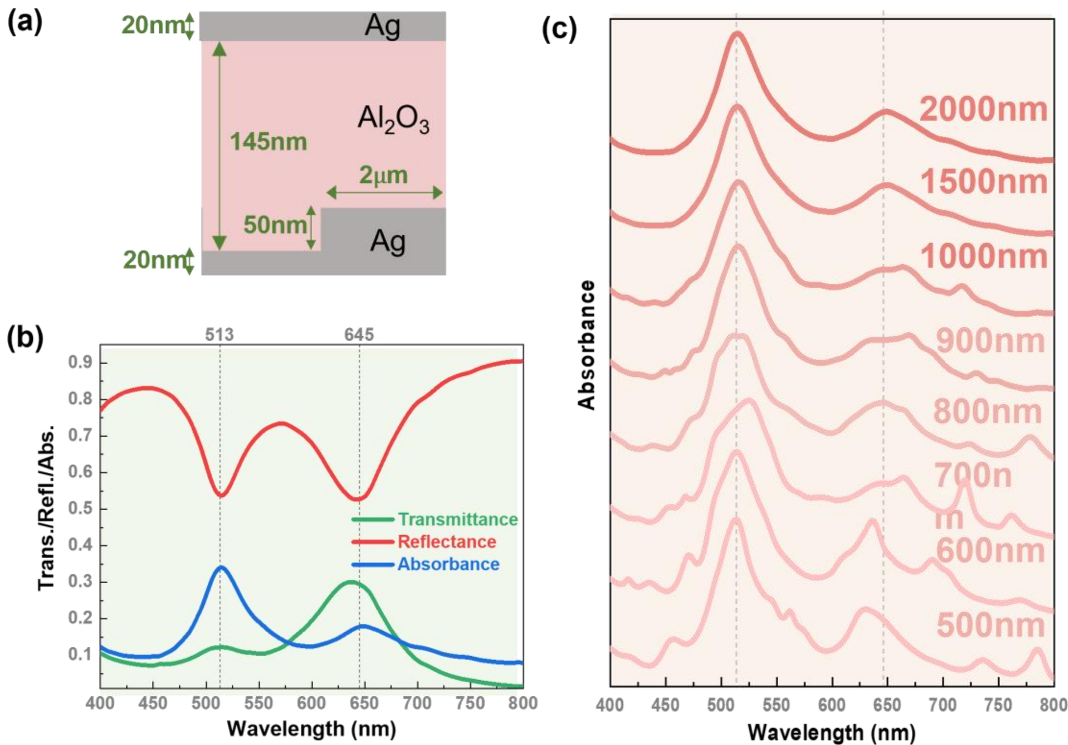

Figure 2.5: Simulation results of grating MIM. (a) Model and design parameters set for simulation. (b) Transmittance (green) Reflectance (red), and Absorbance (blue) of simulated grating MIM with grating period 2μm and height 50nm. (c) Dependence of absorbance on grating period.

A model with grating height of 50nm and period 4μm is designed and the optical response in shown in Fig.2.5(b). The dielectric thicknesses of the two corresponding MIMs chosen in this case are 145nm and 95nm. We can clearly see the two minima in reflectance with a spectral difference of 132nm in the reflectance plot shown in Fig.2.5(b). We can see that the transmittance at 645nm (corresponding to t_d = 145nm MIM) is more than at 513nm (corresponding to t_d = 145nm MIM). This is because the bottom Ag layer is the MIM with thicker dielectric is less (20nm) than the later (70nm).

The two ENZ modes obtained from the grating MIM do not interact with each other like in MIMIM. There is no coupling or energy transfer between the two MIM responses. But as the periodicity of the grating decreases, the two MIMs feel the presence of the other modes along with the plasmonic and grating modes which are present in nano-grating structures[150,151]. Fig.2.5(c) shows the absorbance dependence on the grating period. We see that once the grating periods are below 1µm, the peaks corresponding to the ENZ modes are perturbed by other new entities. The grating of Ag layer is a diffraction grating whose modes depend on the grating period. For periods greater than 1µm, these modes are in infrared region. For smaller periods, the diffration modes fall into visible region and interfere with ENZ modes.

One can achieve more than two ENZ responses by carefully designing a “double grating MIM”, which has both top and bottom Ag layer structured as shown in Fig.2.6(a). The most important thing to consider while designing such a structure is to make sure that the individual MIMs have access to areas more than 1µm^2. As we have seen from Fig.2.5(c), it is the minimum grating period required to obtain unperturbed spatial ENZ responses. For example, the design in Fig.2.6(a) has the top and bottom grating preriods of 8µm, but the top grating starts at the middle of the bottom grating. This makes it possible to have four MIMs each with length in X-direction of 2µm. The four different MIMs in this case are those with dielectric thicknesses, t_d = 110nm, 130nm,160nm,180nm respectively. The absorbance plot (Fig.2.6(c)) shows four peaks corresponding to the four planar MIMs. The electric field profiles at each wavelength shows the cavity mode which is present only at that resonance wavelength corresponding to that particular planar MIM. This shows tha spatially-different spectral ENZ response of the double grating MIM.

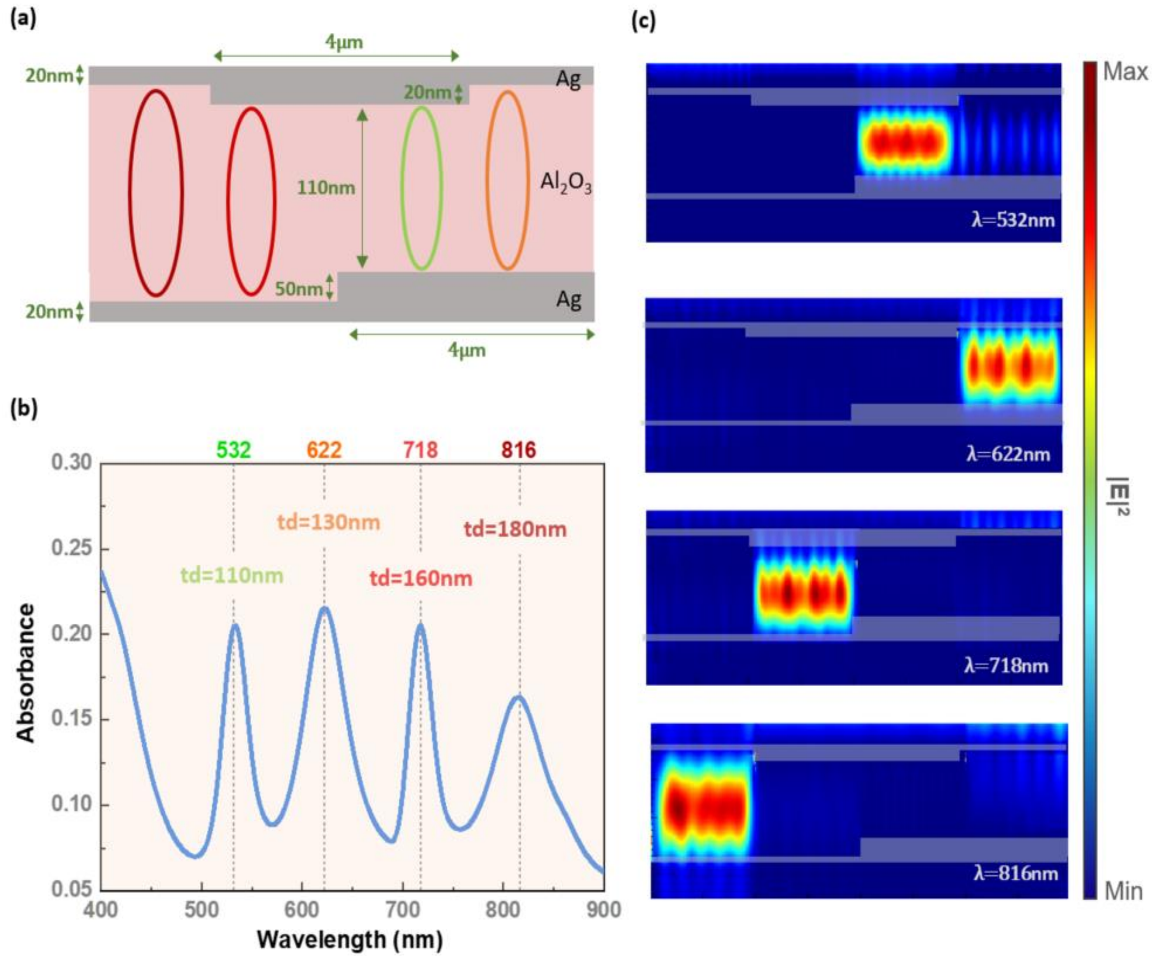

Figure 2.6: Simulation results of double grating MIM. (a) Model and design parameters set for simulation. (b) Absorbance (blue) of simulated double grating MIM with grating period 4µm and heights 20nm (top) and 50nm (bottom). (c) Simulated norm of the electric field calculated as $(E_x^2 + E_z^2)^{1/2}$ at four resonance wavelengths 532nm, 622nm,718nm and 816nm.

2.3.2. Fabrication and characterization

The fabrication of a grating MIM is a multi-step process involving photolithography and e-beam evaporation. The simple way to fabricate a grating MIM of periodicity 2.5µm and height 20nm is to deposit 40nm of Ag, followed by patterning the Ag layer by etching using a photoresist mask, then depositing Al_2O_3 to fill the etched areas, followed by liftoff of photoresist and finally depositing the Al_2O_3 and Ag of desired thicknesses. While trying to fabricate the sample using these process steps, we encountered a problem in the second step of etching Ag. After the lithography process, while wet etching Ag using standard gold etchant (by Sigma-Aldrich) for few seconds, the etchant attacked edges of the areas under the photoresist as well. As a result, there is an undercut after the liftoff of the resist. One way to overcome this problem is to dry-etch Ag using RIE process, but in the facility we have we cannot etch metals as it causes technical problems to the instrument. Therefore, we had to adapt a to a more lengthy but effective fabrication process.

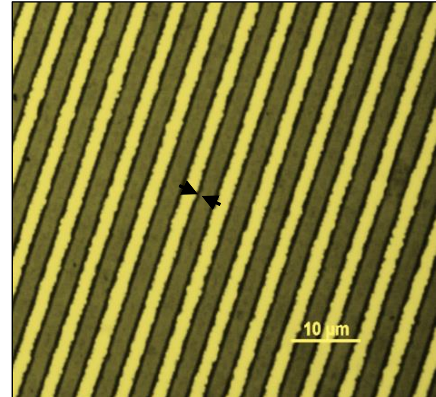

Figure 2.7: Optical microscope image of sample after wet etching of Ag layer. The dark and bright yellow lines are silver with different thicknesses. The arrows indicate the undercut due to the etching (black lines).

This process involves using a different metal mask layer to obtain alternate Ag and Al_2O_3 layer patterns. Fig.2.7 shows the process steps involved in fabricating a successful grating MIM device. First, Ag of 20nm thickness was deposited using e-beam evaporator at a rate of 0.3 A°/s on a glass substrate of thickness 500µm. Photoresist S1813 was spincoated on the sample at 4000rpm speed which produced around 1.5µm thick resist. With the mask aligner, the resist was patterned using a photomask of symmetric grating with periodicity 5µm. 20nm of Ag, 5nm Al_2O_3 and 50nm of copper (Cu) were deposited in the evaporator followed by resist liftoff. The thin layer of Al_2O_3 protects the Ag layer from Cu etchant. This produced a sample with continuous 20nm Ag layer over which a grating pattern consisting of Ag, Al_2O_3 and Cu is present. Then an Al_2O_3 layer of 20nm, which is equal to

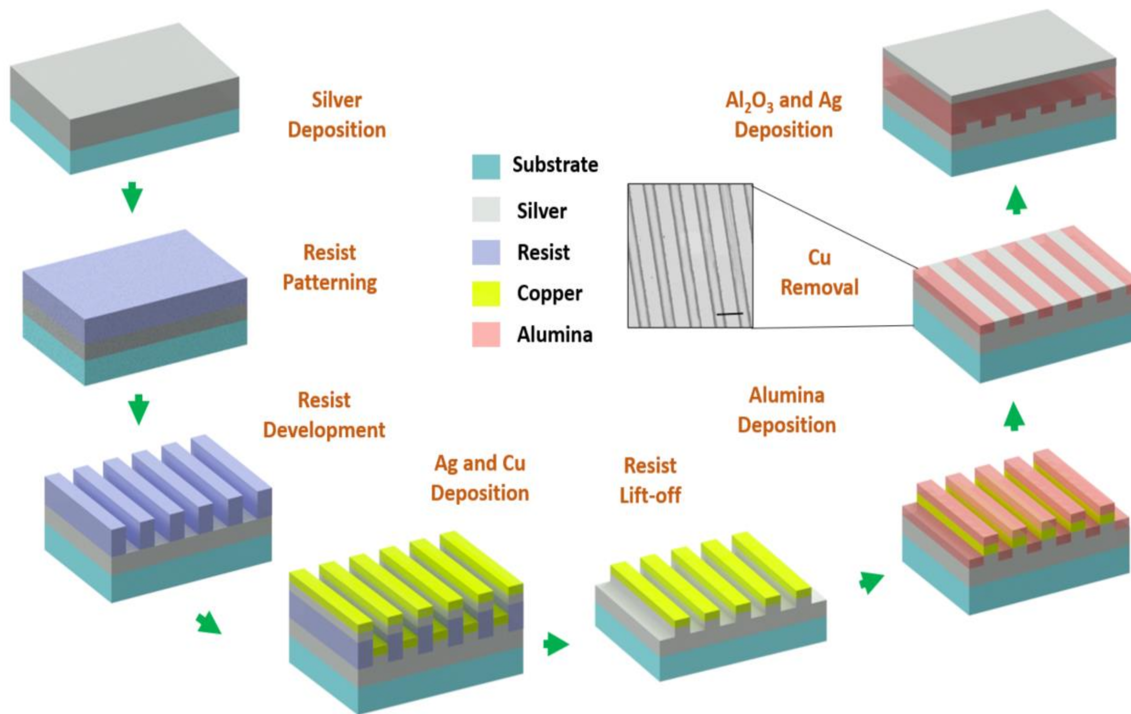

Figure 2.7: Steps involved in fabricating the grating MIM. The inset shows the SEM image of the sample after removing the mask Cu layer. Scale bar 5μm.

the height of Ag layer in the grating pattern, is deposited using the evaporator. After this, the Cu layer is etched using dilute Ferric Chloride ($FeCl_3$) solution. This left alternate Ag and Al_2O_3 layers as shown in the SEM image in Fig.2.7 in the inset. Finally, an Al_2O_3 layer of 120nm (1 A°/s) and Ag layer of 20nm (0.3 A°/s) were deposited using the evaporator.

The grating MIM was characterized using ellipsometry to study the optical response of the device. The transmittance data for different polarizations and different angles of incidence were recorded (Fig.2.8). In parallel to fabricating the grating MIM, planar MIM control samples were fabricated to compare the responses. Fig.2.8(a) shows the p-transmittance at 30° incidence angle for the grating MIM, along with the corresponding planar MIMs. We can see a good correspondence between the grating MIM resonances and the planar MIM resonances similar to the simulation data. Since the bottom Ag layer, corresponding to the MIM with t_d = 120nm, is 40nm, and thus thicker than for t_d = 140nm which is 20nm, the transmittance for the regions with where the MIM has a dielectric

thickness of t_d = 140nm should be higher. However, we observed more signal from the from the higher frequency mode, which is related to the area coverage of the differently structured regions. Even though the photomask used for patterning had a symmetric grating periodicity (2.5µm exposed, 2.5µm unexposed), due to the inconsistencies in the fabrication process steps, the final sample did not manifest a symmetrical grating. The area in the grating MIM covered by the MIM with t_d = 120nm is larger than that of MIM with t_d = 140nm. As the measurements done were with incident beam spot size around 2mm, and the data recorded is the collective response, the transmittance value at

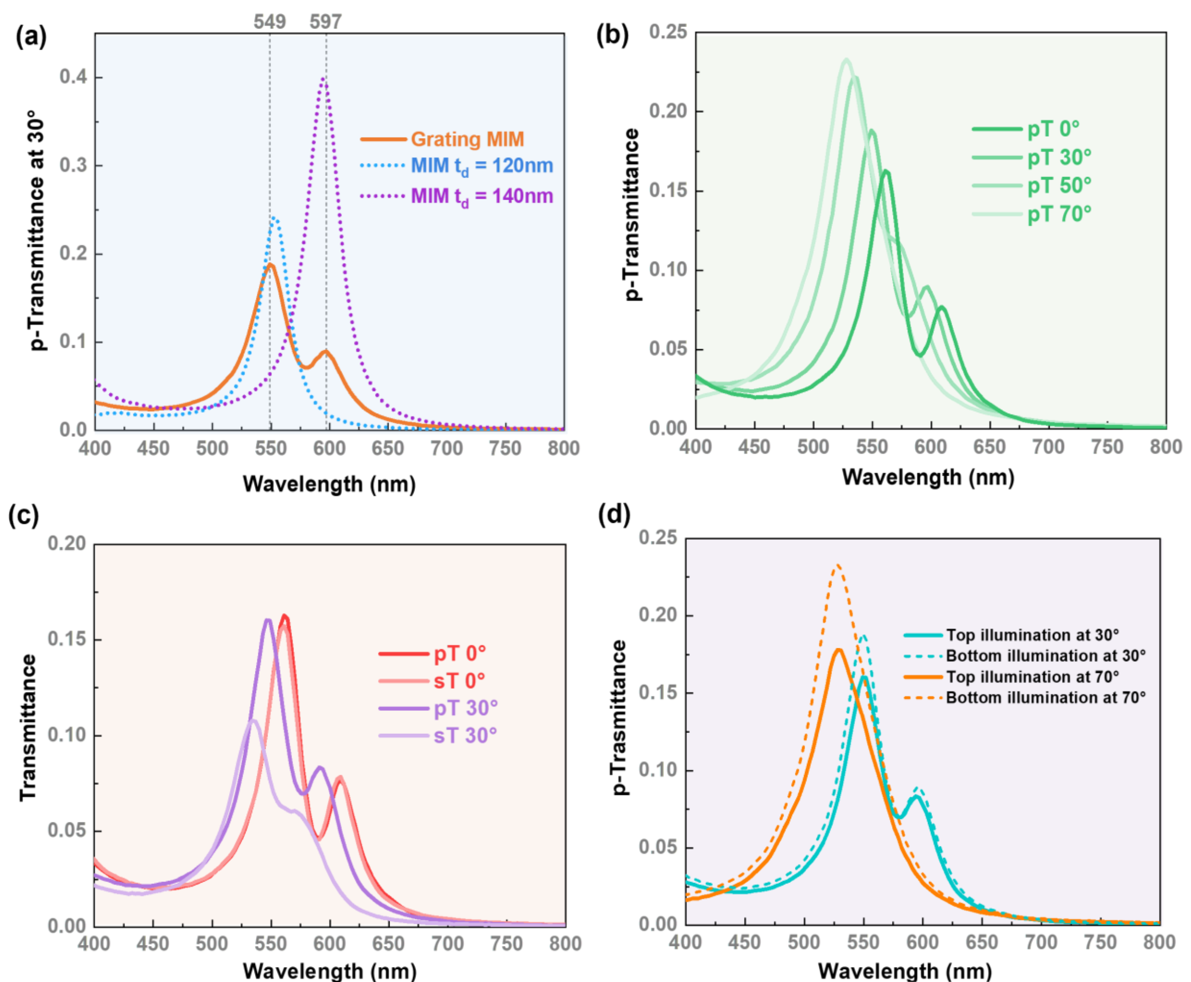

Figure 2.8: Experimental results of grating MIM. (a) Transmittance of Grating MIM (orange) along with corresponding planar MIMs of insulator thicknesses 115nm (blue) and 135nm (violet). (b) p-Transmittance dependence on angle of incidence. (c) p and s-Transmittance at angle of incidences 0° and 30°. (d) Transmittance of grating MIM at different angles when illuminated from top (front) and bottom (backside) of the sample.

resonance at a wavelength of 549nm (corresponding to MIM with t_d = 120nm) is higher than that at wavelength 597nm (corresponding to MIM with t_d = 140nm). For the same reason, we cannot determine the exact permittivity values of the grating MIM, because even though there are ENZ modes corresponding to single MIMs, the separate values add up and do not show the individual dispersions. Nevertheless, we can demonstrate the ENZ nature by a careful interpretation of the transmittance data.

The angle dependence as shown in Fig.2.8(b) shows that the resonances blue shift as the angle increases, which is similar to the planar MIM response. The second peak slowly diminishes as the angle increases, the reason for this might be that at higher angles, the light doesn't completely reach the bottom (to 20nm Ag layer) of the grating MIM, instead gets reflected by 40nm Ag layer of the grating, resulting in stronger response from thinner dielectric MIM with respect to the thicker dielectric MIM. Fig.2.8(c) shows the polarization dependence of the transmittance at two different angles of incidence. We see that at normal incidence the p- and s-polarized response is the same. With 30° angle of incidence, we see the shift between pT and sT, because of the excitation of plasmonic modes. This results in the shift between the responses with different polarizations. This angle- and polarization-dependent responses prove the ENZ nature of the modes.

To experimentally confirm that the double grating MIM analyzed in the FDTD simulations works, we illuminated the sample from bottom (through the glass substrate) to prove that we get similar results with top grating MIM as well. Fig.2.8(d) shows the p-Transmittance at two different angles from top and bottom illumination. We see that the response in both configurations is the same, proving that with careful alignment while performing lithography one can fabricate and obtain results similar to simulation data with double grating MIM.

2.4. Conclusion

We have simulated and fabricated a Grating MIM which gives spatially variant spectral response. The grating MIM delivers two different spectral outputs if the grating period is more than 1µm. This can be used to fabricate Bayer format pixels[117] with basic spectral components red, blue, and green with pixel unit size of 4µm which is well beyond the human eye resolution and comparable to present day display technologies. The spatial ENZ response can also be used to enhance specific spectral response in certain areas of emitting layers that are embedded in the cavity.

Chapter 3

MIM MICROPILLARS: Talbot Lithography and Cavity Resonance for Photoluminescence Enhancement

I feel like my mind just made a baby! And it's beautiful. It's not like human babies which are loud and covered in goop.
- Sheldon Cooper

In this chapter, planar MIMs are patterned as micro and nano pillar structures and their properties are analyzed. A cost-effective lithographic technique called Talbot lithography is investigated to obtain submicron sized features. Samples made using this technique were employed to enhance Photoluminescence of Molybdenum Disulfide (MoS_2) monolayers

3.1. Cavity and Dipole resonances in MIM pillars

Planar Metal-Insulator-Metal (MIM) nanocavities are infinitely long in X and Y-directions, and their use as Fabry-Perot cavities was demonstrated in myriad of applications[119-122]. Similarly, MIM nano resonators with nanometer dimensions in X, Y and Z-directions have also been extensively studied and employed in multiple applications[124-129]. MIM nanoresonators exhibit electric and magnetic dipole resonances when the dimensions are comparable to the incident light wavelength. In this section, we investigate the existence of cavity resonances in MIM micro and nanostructures.

Simulations

One of the most investigated structural configurations in metamaterials are nanopillars. We study this geometry to understand the effects of lateral confinement in MIM

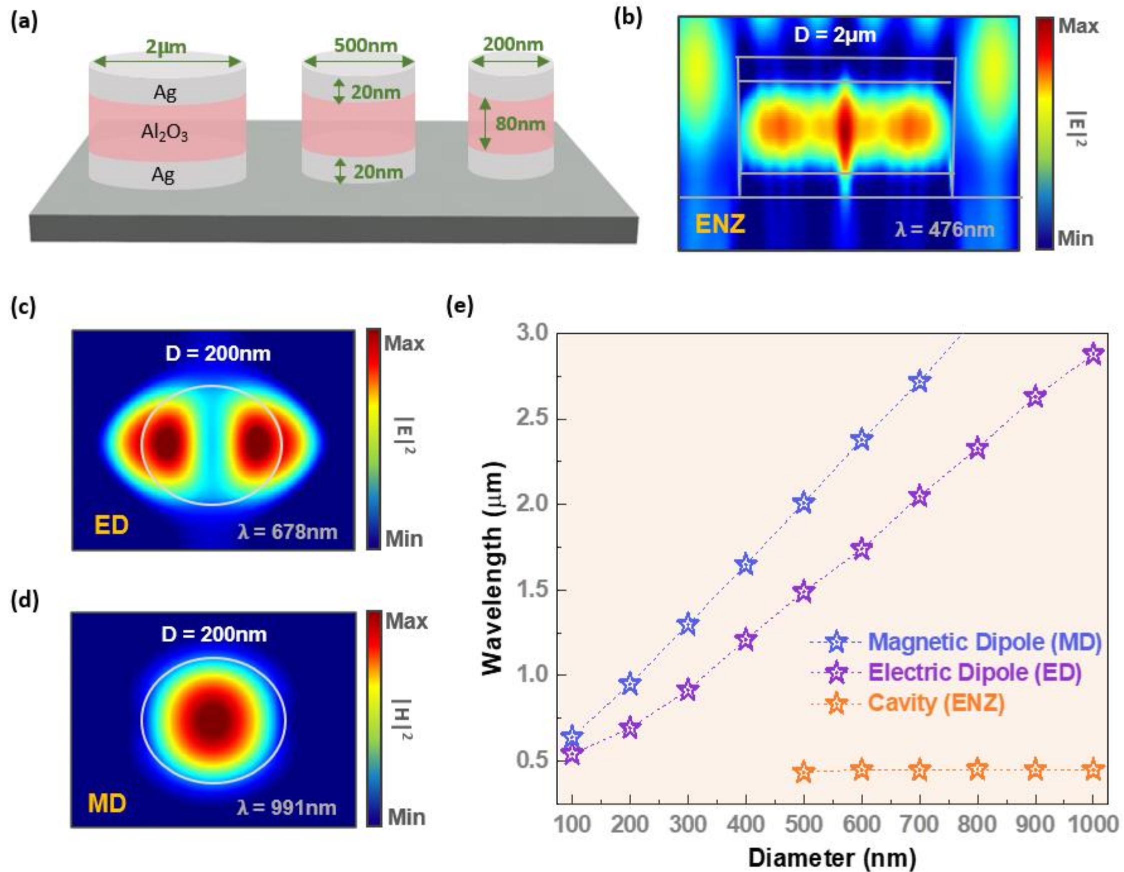

Figure 3.1: Different resonances in MIM pillars. (a) Schematic of MIM pillars of different diameters (D). b) Electric field along the XZ plane (y = 0) at the cavity resonance (ENZ) wavelength for pillar with D = 2μm . (c,d) Top views on a pillar with D = 200 nm. (c) Electric field along XY plane at Electric Dipole (ED) wavelength. (d) Magnetic field along XY plane at Magnetic Dipole (MD) wavelength. (e) Variation of MD, ED and ENZ modes with the diameter of the pillars.

nanocavities. MIM pillars of different diameters (Fig.3.1(a)) were analyzed experimentally and theoretically using Lumerical FDTD simulations. When the diameters (D) of the pillars are in the submicron range, electric and magnetic dipole resonance modes which are generally present in MIM nanostructures fall into the visible and Near-infrared (NIR) spectral range[129]. ENZ cavity resonances originating from planar MIMs are identified as peaks in transmittance and absorbance and minima in reflectance. When the diameter of the pillars is in the micron range, the cavity resonance behaves like the planar MIM. Fig.3.1(b) shows the electric field profile of a simulated D = 2μm MIM pillar at the resonance wavelength of 476nm with 20nm Ag, 80nm Al2O3 as metal and insulator

respectively. On the other hand, Figs. 3.1.(c) and 3.1(d) show the electric and magnetic field profiles along XY plane at Electric Dipole (ED) and Magnetic Dipole (MD) resonance wavelengths, at 678nm and 991nm respectively, for a MIM pillar with D = 200nm. Fig.3.1(e) shows the variation of modes with the diameter of the pillars. As the diameter of the pillars increases, the dipole modes shift towards the infrared region. But in the case of the cavity modes, the mode remains constant for diameters larger than 500nm, and below 500nm they become weaker with decreasing wavelength until they cannot be resolved as a peak in transmittance anymore.

Experiments

To confirm the simulation results, samples were fabricated and characterized with different pillar diameters. In this chapter, we focus on ENZ cavity resonances, while experiments regarding dipole resonances will be presented in the next chapter. We consider two samples to analyze the cavity modes, one with D = 2µm and other D = 500nm. MIM pillars with diameters of 2µm were patterned using photolithography and pillars with 500nm diameters with electron-beam lithography (EBL). A photomask with square array of holes of diameters 2µm and periodicity of 4µm was used for photolithography process. After replicating this pattern on a photoresist using a Mask Aligner; 20nm of Ag, 80nm of Al_2O_3 followed by another Ag layer of 20nm were deposited using an e-beam evaporator. Lift-off of resist produced an array of MIM pillars of diameters 2µm. A more elaborate fabrication process involving Electron-beam Lithography (EBL) patterning will be presented in the next chapter.

Fig.3.2(a,b) shows the SEM images of fabricated samples with diameters 500nm and 2µm respectively. The corresponding planar MIM (t_d = 80nm) transmittance plot (Fig.3.2(c)) shows that the cavity resonance occurs at λ = 480nm. The p-transmittance of the pillar samples is shown in Fig.3.2(d). When compared to a planar MIM, there is a blue shift in the transmittance peak associated to the cavity mode as the diameter decreases. For D= 500nm the peak becomes broader and appears at 471 nm, thus blue-shifted with respect to the planar MIM where it occurs at 480 nm. The ED and

MD modes for 500nm pillars are in infrared region, and therefore only their higher order modes fall in visible region (Fig.3.1(e)). The interference of these modes with the cavity resonance results in perturbed spectral peaks: The dips in the transmittance (Fig.3.2(d)) of D = 500nm pillar at 556 and 774nm can be identified as electric octopole (EO) and magnetic hexadecapole (MH) modes from simulations[130]. There are also additional effects caused by diffraction of the array that contribute to the spectral shape. The cavity resonances can be more straightforwardly studied in simulations where a PML (Perfectly Matched Layer) boundary in X and Y direction is used. Fig. 3.2(e) shows the electric field profile of a D = 500nm MIM pillar at 471nm. It shows that the electric field is not completely confined in the dielectric layer as for planar MIMs. This proves that lateral confinement affects the MIM resonances for smaller diameters, and hence the modes are not fully confined.

The ENZ nature of the MIM pillars is further demonstrated by polarization and angle dependent measurements. Fig.3.2(f) shows the transmittance plot for D = 2µm pillars for different polarization angles (ϕ_p). We see that the peak blue shifts for ϕ_p = 0° (p-polarization) to ϕ_p = 90° (s-polarization), which is typical in the ENZ response of a planar MIM. The p-Transmittance peak dependence on the angle of incidence for planar and pillar MIMs is shown in Fig.3.2(g). The blue shift with the angle corroborates the ENZ nature of the pillars.

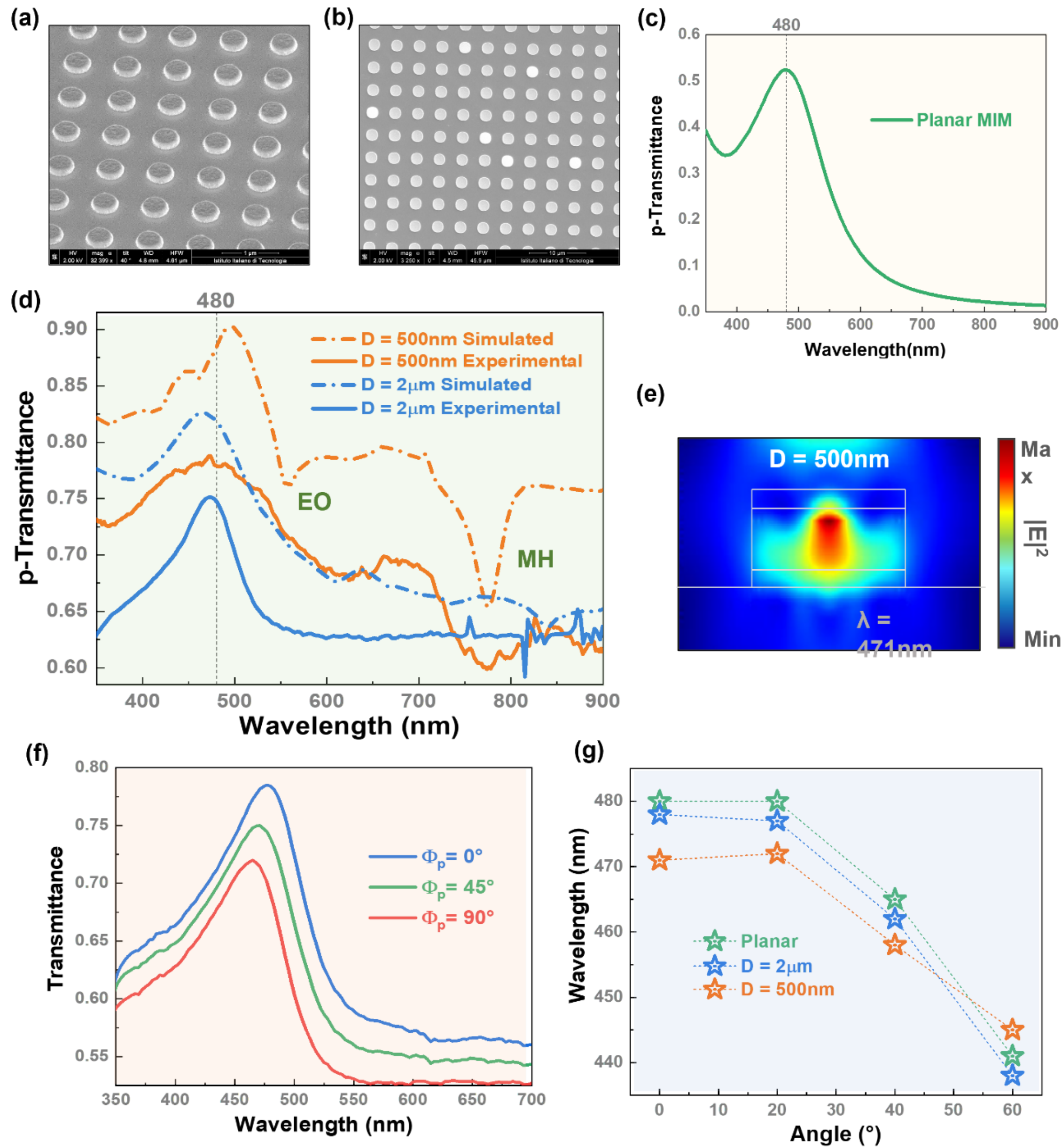

Figure 3.2: SEM images of fabricated pillars of diameters (a) 500nm (b) 2µm. (c) p-Transmittance of corresponding planar MIM (d) Simulated and experimentally measured transmittance of MIM pillars with diameters, D = 500nm and 2µm. (e) Electric field profile simulated at cavity resonance (471nm) for D = 500 nm pillar. (f) Transmittance of D = 2µm pillars for different incidence angle of polarization (ϕ_p). (g) p-Transmittance dependence on angle of incidence for planar MIM, D = 500nm and 2µm MIM pillars.

3.2. Talbot Lithography

Talbot Lithography also known as Displacement Talbot Lithography (DTL) is an interesting mask-based lithography technique which was invented during the last decade[131-133]. It is based on a phenomena called Talbot effect. Generally, Deep or Extreme Ultraviolet (DUV, EUV) light source is used to obtain patterns with nanometer resolution. When light is incident on a periodic mask, a self-image is obsereved at periodic intervals called Talbot length (Z_T) which is given by,

$$Z_T = \frac{2P^2}{\lambda_i} \tag{3.1}$$

where P is the periodicity of the mask and λ_i is the incident light wavelength. This formula is valid when $P > \lambda_i$. Fig.3.3 depicts the 'Talbot Carpet' generated when a plane wave is incident through a grating of period 'P'. The self image of the grating is produced at a distance of Z_T. The exact same self image with lateral shift of P/2 is observed at $Z_T/2$. Along the Talbot carpet, the replica of the original mask, with feature sizes and periodicities divided by an integer factor are observed. For example at $Z_T/4$, the feature size and periodicity are halved thus producing twice the number of original features. At $Z_T/8$, the feature size and periodicity are further halved thus producing four times the number of original features but of 1/8th the original size.

This concept has been sucessfuly utilized to develop a lithographical tool (DTL) and produce nanometer resolution designs[132,133]. By placing the substrate at factors of talbot length, one can achieve features much smaller than the original mask. However, this requires accurate substrate placing from the mask and most of the tools use Extreme Ultraviolet (EUV) sources due to their smaller wavelengths. This accounts for an expensive setup. Here we use standard photolithography in contact mode to obtain nanometer sized features with photomask of micrometer size features.

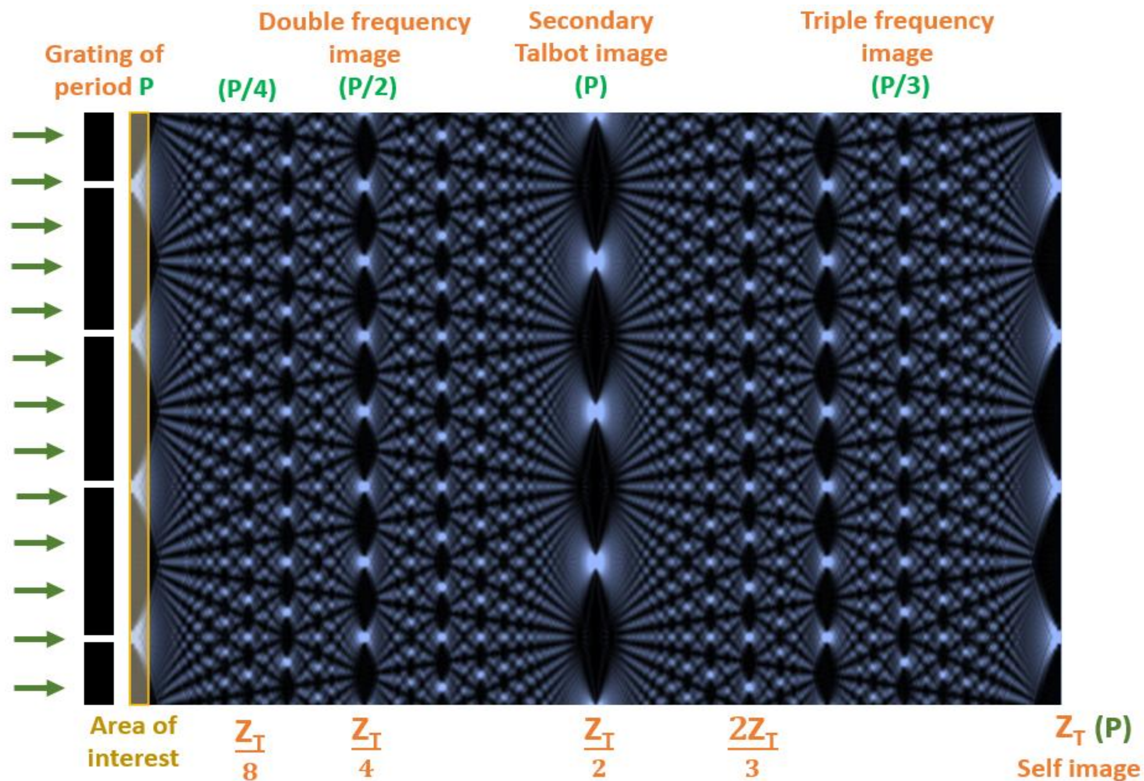

Figure 3.3: Talbot carpet of a 1D grating of period 'P' depicting the patterns at different integrals of talbot length. *Reproduced and modified from Ref. 134.*

Consider a mask of hexagonal array of holes of diameter 2µm with period 4µm and a standard photolithography light source of wavelength 365nm. The Talbot length calculated according to eq.(3.1) is approximately 87.6µm. With standard contact mode lithography, the mask and substrate are seperated by the resist which is few micrometers in thickness, much less than the Talbot length. In Fig.3.3, we see that at the start of the Talbot carpet (area of interest), the light is diffracted from the apertures, keeping the original beam intensity high for certain distance along with diffracted beams. In this area, due to Fresnel diffraction we see higher order diffracted beams along with the original transmitted beam. We operate in this area to obtain smaller features along with the original mask design.

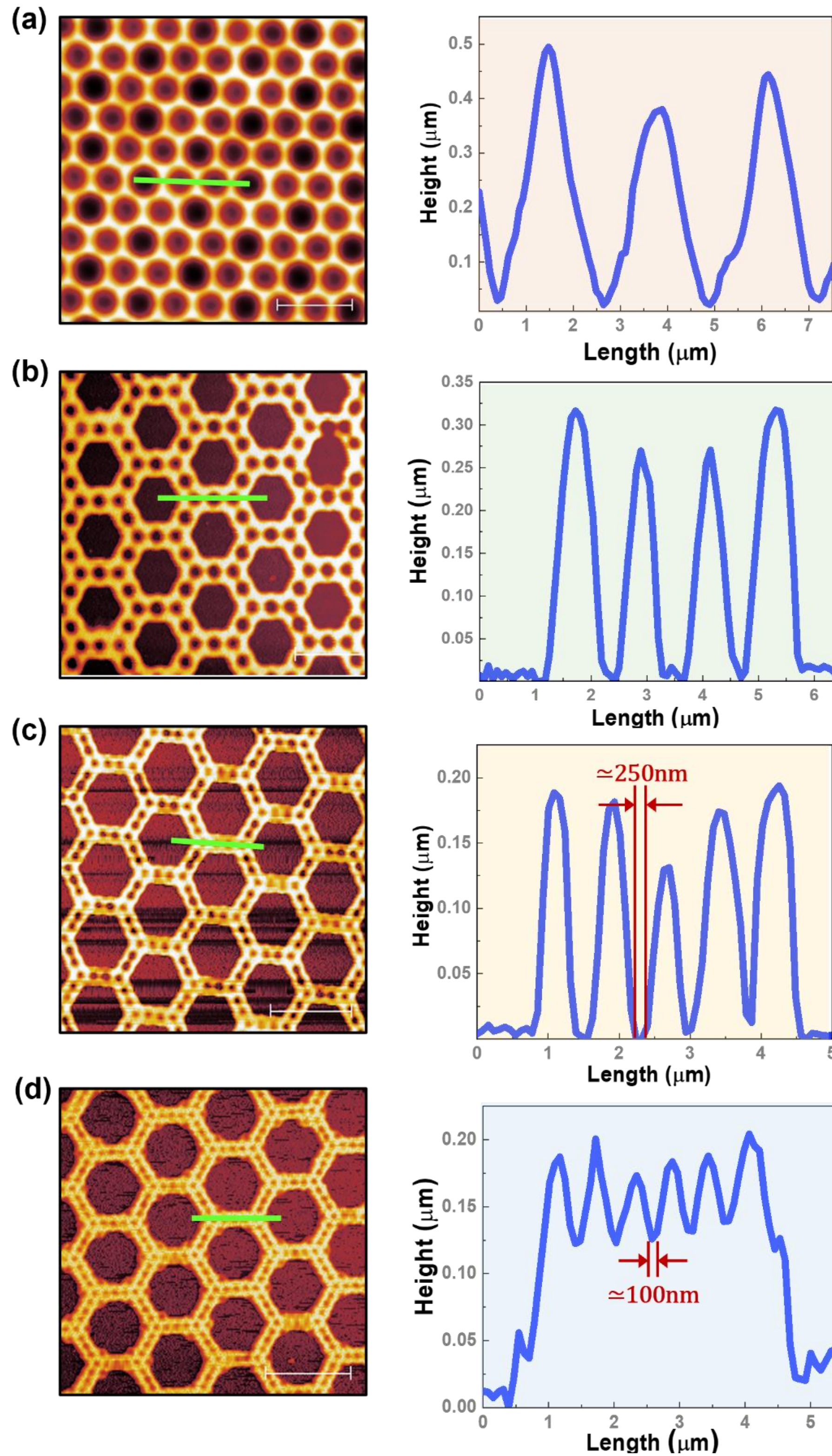

Figure 3.4: Talbot lithography. AFM images of different patterns developed on photoresist along with the corresponding line profiles showing the height.

In order to obtain different orders of diffracted pattern, we use resist with different thicknesses. S1813 photoresist produces around 1.5µm thick films at 4000rpm spin speed. To produce much thinner films we dilute the resist using Anisole as solvent in 1:1 ratio and spincoat at different spins. We obtained resist films of thicknesses around 670nm, 520nm, 310nm and 250nm at spin speeds 4000, 5000, 6000 and 7000 rpm respectively. With the above mentioned hexagonal array of holes, the samples were exposed using contact photolithography for 8-10 seconds and developed for 25-30 seconds (all the process parameters were optimized after several trials for each sample).

Fig.3.4 shows the AFM images of some developed patterns on the resist. We see that the main pattern of the mask is present and increases in size in all the samples. If we consider two adjacent holes which are not the nearest neighbours, we seen that between these two main holes, smaller holes of different sizes originate. In Fig.3.4(a), we see new features of 1µm diameter and 2µm period, which are half in size than those in the original mask, which is the order-1 pattern. Similarly in Fig.3.4(b), the new features are around 500nm in diameter and 1µm in period and correspond to the order-2 pattern. The Figs.3.4(c,d) shows the order-3 and order-4 patterns with feature sizes around 250nm and 100nm and periods 500nm and 250nm respectively. Similar patterns can be obtained for square array of holes as well. Fig.3.5 shows the original mask pattern, order-1 pattern and order-2 pattern of square array of holes. Hence, we were able to produce holes of sizes as small as 100nm with a standard photolithography setup and a mask with 2µm structures.

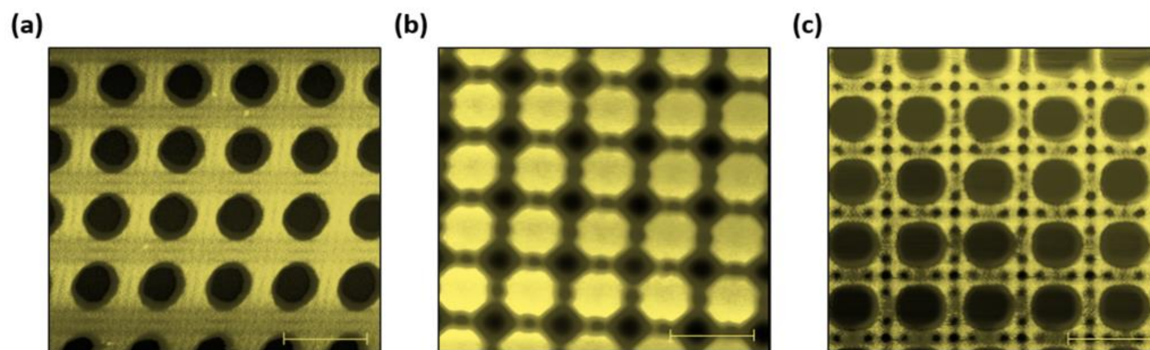

Figure 3.5: AFM images of different patterns developed on photoresist using a photomask of square array of holes.

3.3. PL enhancement in Molybdenum Disulfide monolayers

In this section, we use talbot lithography to fabricate MIM pillars of different diffraction orders to use the ENZ cavity response to enhance the Photoluminescence (PL) spectra of Molybdenum Disulfide (MoS_2) monolayers. MoS_2 is an atomically thin semiconductor which is identified as transition-metal dichalcogenide (TMDC) monolayer. This family of materials have direct bandgap and are used for multiple applications due to their unique properties related to 2D structure of the materials[135,136]. MIM nanocavities were reported to enhance the PL of emitter layers when the cavity resonance matches the emitter absorption or emission[110], and we tested this approach for MoS_2 in combination with MIM pillars.

Hexagonal array of circular holes were patterned in the resist along with order-1,2,3 patterns using talbot lithography (Fig.3.5 (a-d)). After the resist development, multi-layer deposition of MIM layers is done using e-beam evaporation. After the liftoff, we obtained

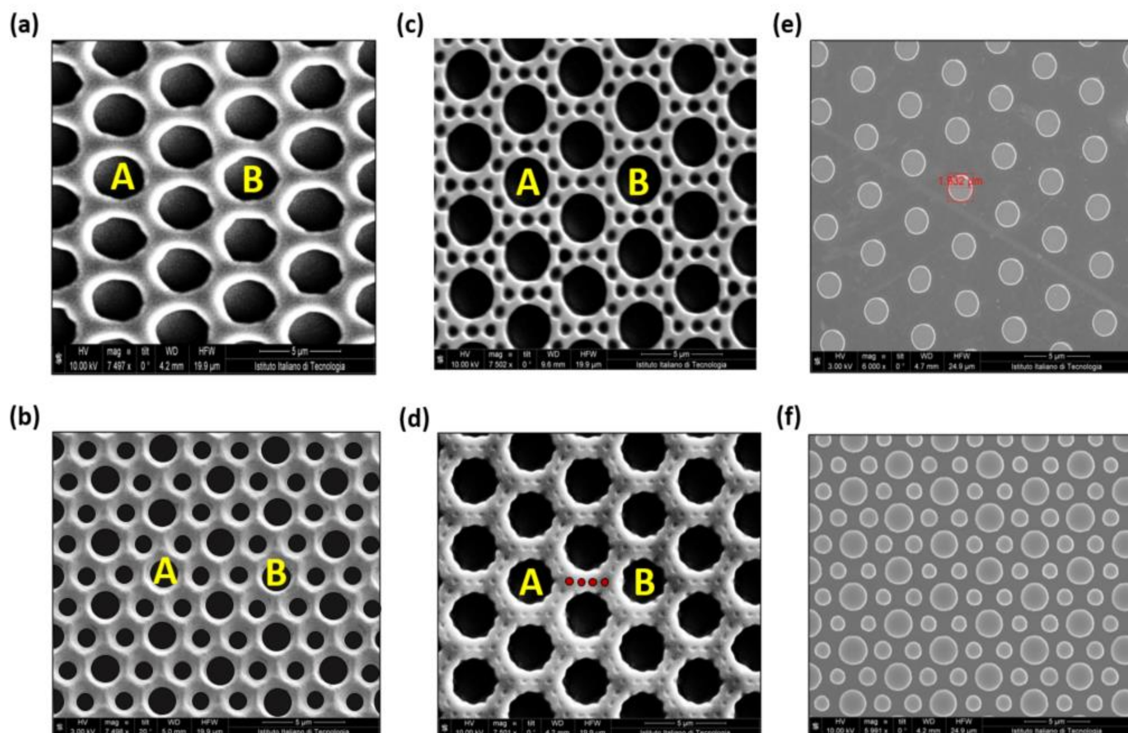

Figure 3.5: SEM images of samples fabricated using Talbot lithography for TMDC transfer. (a-d) Developed resist patterns of different resist thicknesses (e,f) Samples after successful liftoff of developed patterns (a) and (b)

MIM pillars using the resist patterns from Fig. 3.5(a,b) resulting in pillar arrays shown in Fig.3.5(e,f) respectively. Lifting off the resist for patterns in Fig.3.5(c,d) is difficult as the resist thickness is thin and the smaller features are not completely developed even using longer developing times.

The fabricated pillars have two different fill factors (ratio of area covered by the MIM pillars to the total area). The pillars fabricated are 1µm and 2µm in diameter, which according to the simulations should sustain the cavity modes and therefore able to manifest Purcell effect enhancement. Generally, Surface Plasmon Enhanced Absorption (SPEA) and Surface Plasmon Enhanced Coupled Emission (SPCE) are the main mechanisms that result in this kind of enhancement[110,137]. To achieve these effects, we need to match either the absorption (SPEA) or the emission (SPCE) of the emitter to the MIM resonance. SPCE has been reported to give better enhancement, so we use the MIM which can couple with the emission of the MoS_2 monolayer. The MIM pillars are fabricated with the insulator (Al_2O_3) thickness of 145nm so as to match the PL emission of MoS_2 at 660nm. An additional 35nm of Al_2O_3 is deposited on top of MIM and MIM pillars to avoid quenching due to the metal layers[110].

A transfer station setup was used to place the MoS_2 flakes on the MIM pillars. In order to facilitate the process, Polydimethylsiloxane (PDMS) stamps were used. A cube of PDMS was cut and placed on a glass slide. Then a thick viscous droplet of PDMS is placed on top of this cube to get a curved top surface (Fig.3.6). Thin polycarbonate films were used as the top cover of the PDMS. Boron Nitride (hBN) flakes were used as sacrificial layers to pick up the MoS_2 monolayers as they provide better adhesion. The main process steps are (i) exfoliating hBN flakes onto a Si substrate from the crystal, (ii) use the prepared glass slide to pick up the desired hBN flake with the transfer station, (iii) MoS_2 monolayers are then picked up with the assist of

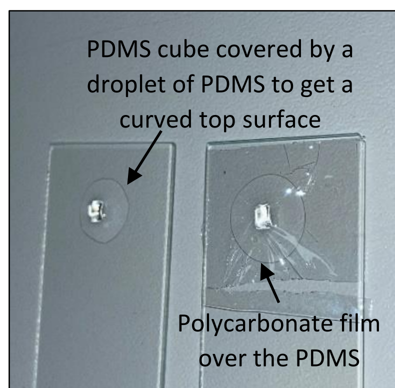

Figure 3.6: Photographs of glass slides with PDMS and polycarbonate used for transferring the MoS_2 flakes

hBN flake (iv) the glass slide with the MoS_2-hBN flake is then brought in contact with the substrate on which they have to be placed, (v) the temperature of the substrate is increased in order to melt the polycarbonate film. (vi) once the polycarbonate is melted onto the substrate, it leaves the MoS_2-hBN flake also, (vi) finally, the polycarbonate film is washed in chloroform leaving the flakes on the substrates. Fig.3.7(a-c) shows the SEM images of the transferred flakes on three different substrates, planar MIM (Flake 1), MIM pillars in mask pattern (Flake 2), MIM pillars with order-1 pattern (Flake 3). The transferred flakes are tens of micrometers in size.

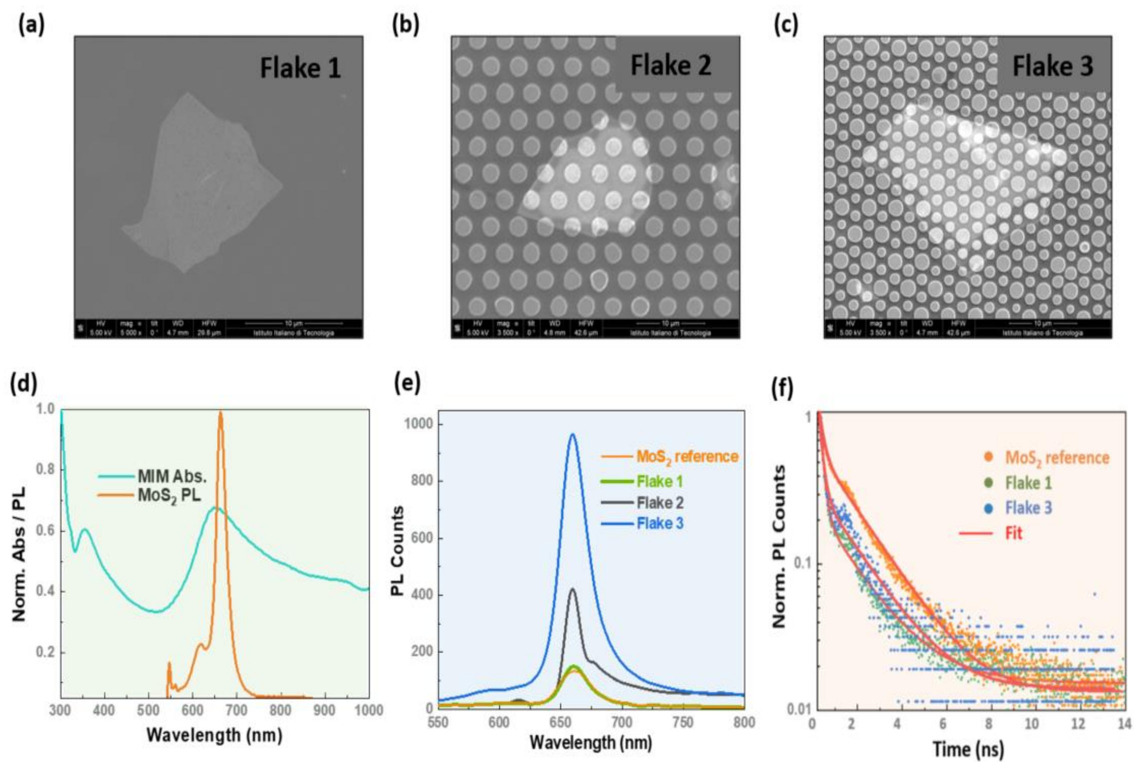

Figure 3.7: (a-c) SEM images of MoS_2 flakes transferred on to (a) planar MIM and (b,c) pillar MIMs with different fill factor. (d) Normalized absorbance of the planar MIM and PL of the MoS_2 monolayers on Si substrate. (e) PL spectra of MoS_2 flakes on different substrates as depicted and labelled in the SEM images (a-c). (f) Lifetime decay of MoS_2 flakes on different substrate along with exponential time decay fit

The MIM pillars fabricated have diameters of 2µm for mask pattern (Flake 2) and, 1µm and 2µm for order-1 pattern (Flake 3), they sustain ENZ cavity modes (Fig. 3.1(e)) and their response is similar to planar MIMs. Fig.3.7(d) shows the normalized absorbance of

the planar MIM and PL of the MoS2 monolayer. Using micro-PL setup, the PL of the flakes was measured with a laser of spot size 2.5µm and wavelength 532nm. Fig. 3.7(e) shows the comparison of the PL counts from the MoS_2 flake on Si substrate (Reference) along with the three transferred flakes (Flake 1,2 and 3 in the Fig.3.7(a-c)). Clearly, we see an enhancement in PL with the MIM pillars. The PL enhancement is highest for flake 3 than flake 2 and 1. The substrate geometry along with the cavity resonance coupling is the reason for this kind of enhancement. The PL enhancement due to the Purcell effect results from increase in photonic density of states (PDOS) which enhances the decay rate[110]. Time decay measurements were recorded for the flakes 1 and 3 (on planar and pillar of order-1 MIM) along with the reference are shown in Fig.3.7(f) including exponential decay fit. Due to the instrument response function caused by reflections in the system, we notice an artifact in the decay measurements. The average lifetimes obtained from the fit for the flakes are 0.046 (reference), 0.039 (planar MIM) and 0.04ns (pillar MIM). Even though there is slight decrease in decay lifetime, it is not significant. Unfortunately, the resolution of the set-up used is 4ps and the general lifetime of MoS_2 is reported to be 10s of picoseconds. So, it is difficult to conclude the PDOS contribution with this data.

3.4. Conclusion

In this chapter, we showed with simulations the behavior of micro/nano MIM pillars and their dependence on pillar diameter. With focus on micro MIM pillars, we fabricated and studied the optical response corresponding to ENZ cavity resonance. A cost effective, large area nanometer size patterning with nanometer resolution based on Talbot lithography was explored. Multiple samples were fabricated with a single photomask using standard photolithography setup. These samples were used as substrates to enhance the photoluminescence of MoS_2 monolayer flakes.

Chapter 4

MIM NANOPILLARS: DIPOLE RESONANCES AND ANAPOLE-LIKE MODES

It's simple. Lizard poisons Spock. Spock smashes scissors.
Scissors decapitates lizard. Lizard eats paper.
Paper disproves Spock. Spock vaporizes rock.
And, as it always has, rock crushes scissors.
- Sheldon Cooper

This chapter is dedicated to study the resonant modes in nanopillars. In the previous chapter, we have seen with simulations that dipole modes come into picture when we reduce the diameters of pillars to the nano range. In this chapter we fabricate nanopillars and investigate their optical response to experimentally verify the results of the simulations. We also explore the possibility of exciting an "Anapole" mode with MIM nanopillars.

4.1. Dipole modes in MIM nanopillars

Dielectric nanoresonators have recently gained interest due to their ability to manifest tunable electric and magnetic dipole resonances[138,139]. These resonances which occur in nanostructures can be best explained with Mie theory[140]. They arise when there is large difference in permittivity between the nanostructure and the surrounding medium. The incident electromagnetic energy is stored in these structures at the resonant wavelengths due to the boundary conditions. For this reason, high-index dielectric materials are used to excite these modes. Due to their scattering properties, these resonances found their place in applications like solar cells[141], surface-enhanced Raman spectroscopy[142], sensors[143] etc. The resonance wavelengths depend on the refractive index and the size of

the nanostructure. The magnetic dipole resonance wavelength for a dielectric nanoparticle can be approximated as,

$$\lambda \approx n_d D \tag{4.1}$$

where, n_d is the refractive index and D is the diameter of the dielectric nanoparticle[144]. We see that the resonance is shifted to higher wavelength regimes as the diameter and refractive index increase.

For all dielectric systems, a large refractive index difference is required to excite the dipole modes. In MIM nanopillars this condition is relaxed because the metal layers aid in providing the necessary field confinement to produce dipole modes[145]. The coupling between the two metallic layers produces symmetric and anti-symmetric plasmon modes. The incident electromagnetic radiation causes in-phase charge oscillations in the top and bottom metal layers at the symmetric resonance wavelength, resulting in electric dipole resonance (ED). Similarly, out-of-phase charge oscillations create a circulating current loop in the dielectric layer, giving rise to a magnetic dipole (MD).

Fabrication

To fabricate the MIM nanopillars, we used e-beam lithography to pattern the substrates. Since we wanted to perform transmission measurements, 500µm thick glass substrates were used. To facilitate electron-beam patterning of the resist, a conductive layer was deposited on the resist. Commercially available PMMA A4 (Polymethyl methacrylate) was used as a positive e-beam resist. PMMA was spin coated on glass substrate to obtain a thinfilm of thickness around 150nm. Using e-beam evaporator a thin layer of 10nm gold (Au) was deposited on the PMMA film. The sample is then loaded into the EBL chamber and patterned with a design constituting an array of holes of diameter D and periodicity P = 2D. Samples with three different diameters of 200nm, 300nm and 400nm were exposed with a dose of 300µC/cm^2. After the exposure, the Au film was removed using standard gold etchant for few seconds. Then the PMMA was developed using Methyl isobutyl ketone (MIBK) which was diluted with isopropanol as solvent in the ratio 1:3 for 25 seconds. After the development, multilayers of 20nm Ag, 80nm Al_2O_3, and 20nm of Ag

were deposited using e-beam evaporator. The resist is later lifted off using Acetone at 70°C for 15 – 20 minutes. Fig. 4.1 shows the process steps of the fabrication of nanopillars.

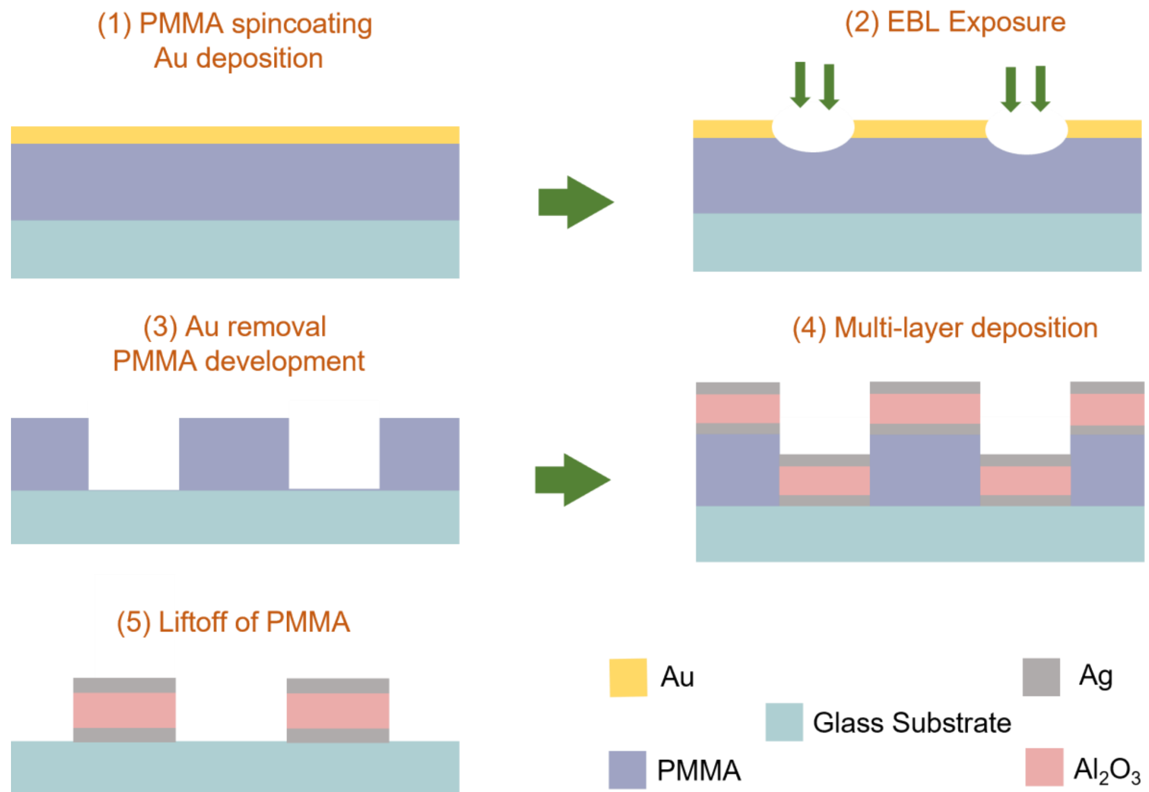

Figure 4.1: Steps involved in fabricating nanopillars with e-beam lithography

Characterization

AFM images of the fabricated nanopillars of diameter 400nm, 300nm and 200nm are shown in Figs. 4.2.(a-c) respectively. The transmittance plots of the MIM nanopillars along with the planar MIM are shown in Fig.4.2. (d). We clearly see the ED and MD modes as minima in transmittance shifting towards infrared region from D = 200nm to D = 400nm. As per the eq. (4.1), the resonance wavelength is directly proportional to the diameter of the pillars, so we observe a red shift with increase in diameter. The peak in transmittance indicating the ENZ cavity mode in planar MIM at 480nm can still be identified in D = 400nm nanopillars, but not in D = 200nm and 300nm. The smaller dips observed in D= 300nm

and D= 400nm plots in the wavelength range of 500nm to 800nm are result of higher order modes of the dipole modes. This data is in agreement with the simulation results, which indicates that the cavity resonances are quenched for nanometer-range diameters of pillars.

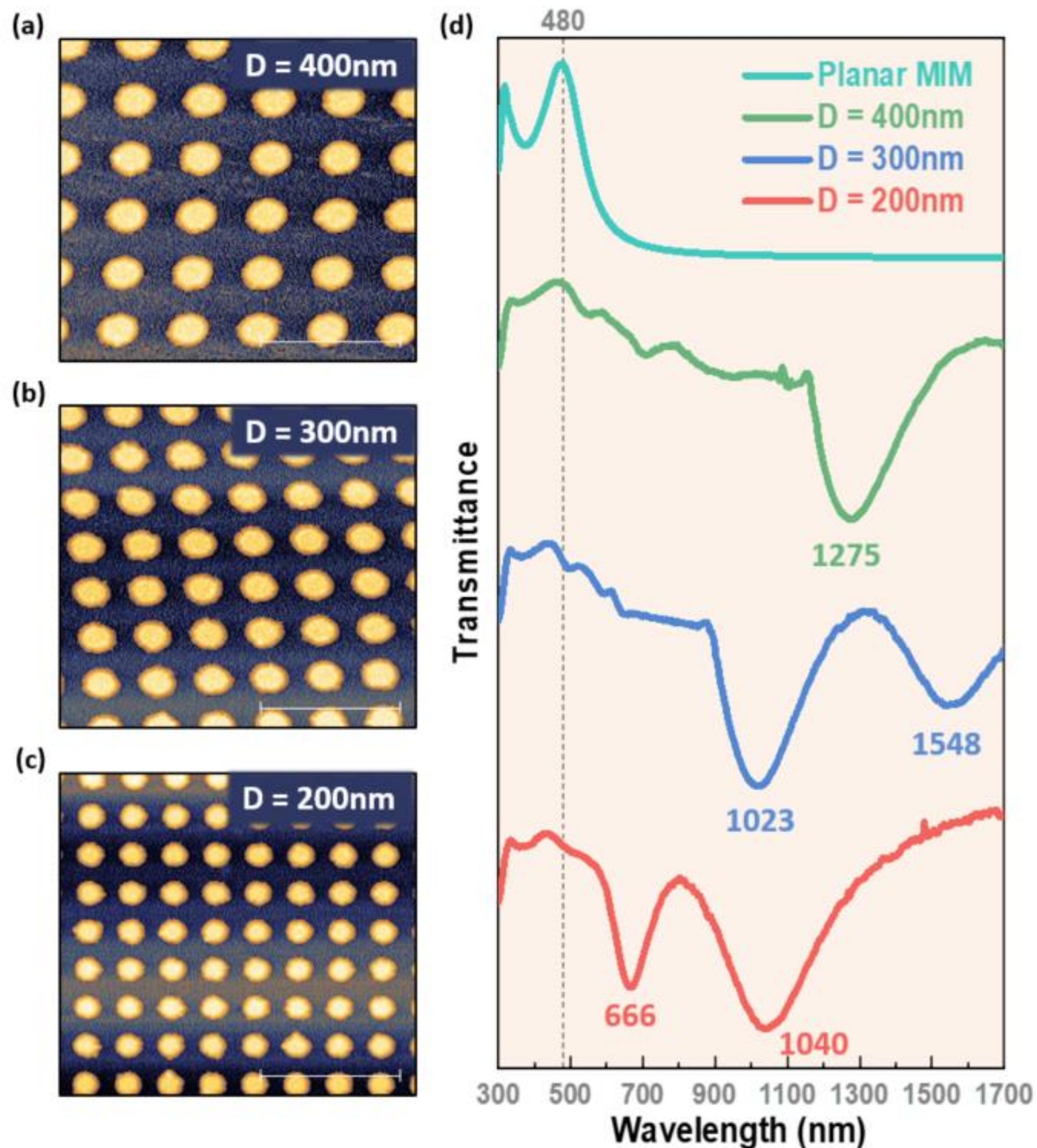

Figure 4.2: AFM images of nanopillars with diameters (a) 400nm (b) 300nm (c) 200nm. Scale bar is 1μm. (d) Transmittance plot of the nanopillars for different diameters along with the planar MIM.

4.2. Anapole-like modes

4.2.1. Introduction

Metamaterials designed using nanostructures with sub-wavelength periodicities are of great interest due to their light manipulation properties at nanoscale[146,147]. These structures exhibit unusual properties like negative refraction[148], cloaking[149], hyperbolic dispersion[150], superlensing[151] etc., which can be tuned by varying the geometrical properties. Using the plasmonic nature of metallic nanostructures, one can achieve perfect absorption[152], optical chirality[153] and light trapping[154]. While they offer promising results, metallic nanostructures suffer from dissipative losses and cannot support strong magnetic resonance modes unless designed with specific geometry like split-ring resonators[155]. All-dielectric metamaterials overcome these losses and support inherent magnetic resonance modes[156]. When illuminated with electromagnetic radiation, displacement currents are induced in the dielectric nanostructures giving rise to magnetic resonant modes. Due to magnetic dipole resonances excited in visible spectra, dielectric nanostructures can be used to create magnetic light[157,158]. They were found useful in applications for phase retardation[159], directional scattering[160], perfect magnetic mirrors[161], Huygens surfaces[162] and others.

According to Mie theory, there are three main dipolar resonances present in nanostructures namely, electric dipole (ED), magnetic dipole (MD) and toroidal dipole (TD)[140]. The destructive interference of two of these modes, cancelling the far-field radiation gives rise to a non-radiative mode called 'anapole'[163,164]. A.E.Miroshnichenko et al reported the first experimental observation of optical anapole[165] using Silicon (Si) nanodiscs following which, they were several reports with different geometrical configurations and materials[166,167].

Most of the research in this field was dedicated to exciting electric anapoles[165-168] and only recently, magnetic anapoles are studied experimentally. Theoretical[169] and experimental[170] demonstrations of magnetic anapoles in the microwave frequency region were reported in high-index dielectric materials. Although perfect magnetic anapoles

were not illustrated, P. Kapitanova et al reported an anapole state as suppression of magnetic dipolar mode and superposition of different multipoles[170]. This depicts that there is more than one way to excite the anapole modes.

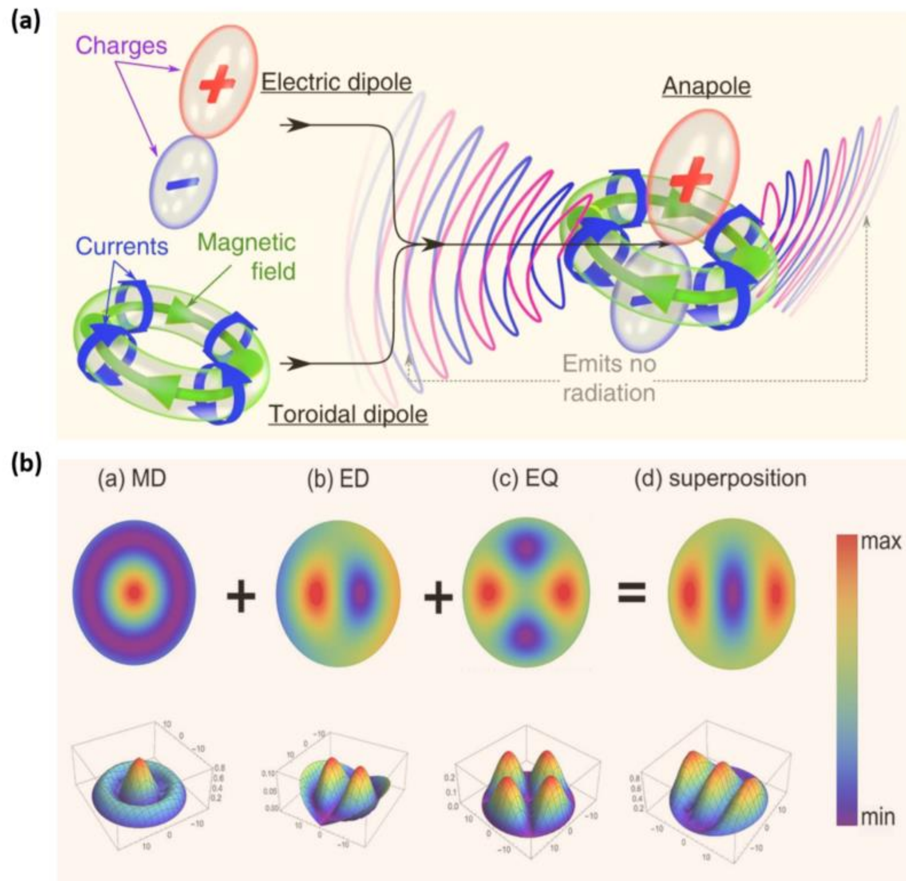

Figure 4.3: Illustration of Anapole modes. (a) Structure of an anapole created due to destructive interference of electric and toroidal dipoles. *Reproduced from Ref.166*. (b) Anapole mode created due to superimposition of magnetic dipole (MD), electric dipole (ED) and electric quadrupole (EQ). The image shows the magnetic field distributions of different modes. *Reproduced with permission from Ref.170. Copyright ©2020 Wiley-VCH GmbH*

Typically, materials with $n \geq 3$, are used which lead to not perfect but lossy anapole modes (not exact zero scattering)[171]. Using materials with lower refractive index leads to significant increase of these losses, making it difficult to decipher the anapole modes. In this section, we used the metal-insulator-metal (MIM) configuration to provide the

necessary field confinement to excite similar modes in low index material such as Alumina (Al_2O_3).

The reported anapole-like modes in this chapter arise from collective response of a metamaterial comprising an array of MIM nanopillars. The behavior of two modes, a magnetic-anapole-like and anapole-like mode[172] (circular electric and magnetic field distributions), and their dependence on the array period were primarily investigated.

4.2.2. Results and discussion

Simulation

Following P. Kapitanova et al. we use the concept of superposition of different higher modes to achieve a destructive interference. To facilitate this, we selected a truncated cone like structure with different dimeters along the height of the pillars as shown in Fig.4.4. This provides excitation of modes corresponding to different diameters. The simulations in this section were performed in collaboration with **Lyuye Lin** using COMSOL Multiphysics. Electromagnetic radiation with wavelengths ranging from 350 to 650 nm is incident in the Z-direction, with electric field polarization in the X-direction and magnetic field polarization in the Y-direction (p-polarization). Silver (Ag) is selected as the metal layer due to its low losses in visible range. Four identical pillars on a 200nm thick glass substrate were modelled with periodic boundaries in the X and Y directions and a PML boundary in the Z direction. The pillars' base diameter (D_b) and top diameter (D_t) are fixed at 330nm and 170nm, respectively. The dielectric environment around the

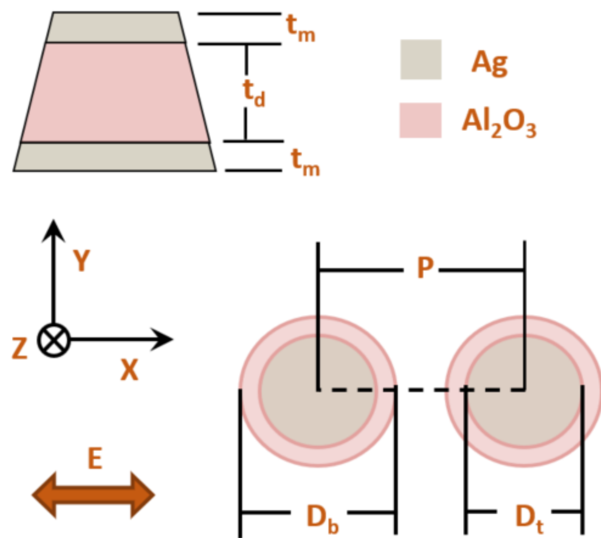

Figure 4.4: Simulated model along with the nomenclature used in this section.

pillars is air (n = 1). The refractive index (n,k) values of the materials used in the simulations were experimentally extracted from individual film ellipsometry data.

For the MD mode to exist, the electric field decay along Z should be sufficient to create opposite orientations of electric fields at the top and bottom of the cavity. This creates a current loop which induces a magnetic dipole moment. The ED mode arises due to the collective polarization of nanopillars with the incident EM radiation. A magnetic current loop is induced in the cavity. The resonant wavelengths depend on the cavity length i.e. dielectric thickness (t_d). When the insulator layer thickness is in the range of tens of nanometers, the resonance wavelengths are strongly dependent on the insulator thickness[173,174]. Once the insulator is thick enough (>120nm), the thickness of the layer has no effect on the resonance wavelengths. We chose thicker dielectric layers, as previous reports on magnetic anapoles primarily used long cylindrical structures[170]. Simulations were performed for thicknesses ranging from 140nm to 280nm, and there was no significant difference in peak strength and positions. We chose t_d = 185nm because it produced the best field profiles. This also helps us to eliminate one parameter which determines the resonance spectrum. With this model, now we ascertained that the resonances we study depend only on the diameter of the pillars.

We begin our investigation by comparing the responses of Al_2O_3 nanopillars and MIM nanopillars. The simulated extinction (1-Trans.) of Al_2O_3 and MIM nanopillars for t_d = 185nm and periodicity, P = 400nm is shown in Fig.4.5(a). We can see a portion of the spectral response of a photonic crystal with Al_2O_3 nanopillars. With the MIM configuration, two peaks at wavelengths of 415nm and 552nm are clearly visible. The results of these simulations represent the collective response of the nanopillars rather than the individual pillar. The magnetic and electric field distributions at 415nm (Fig.4.5.(c,d)) show that the excited mode has circular magnetic and electric field configurations in the YZ and XZ planes respectively. Amanaganti, S.R. et al. termed these field profiles "Anapole-like" mode[172] (referred to as "Mode-1" in this report). Although these modes have been reported in the micrometer regime, we observe in the visible region for the first time.

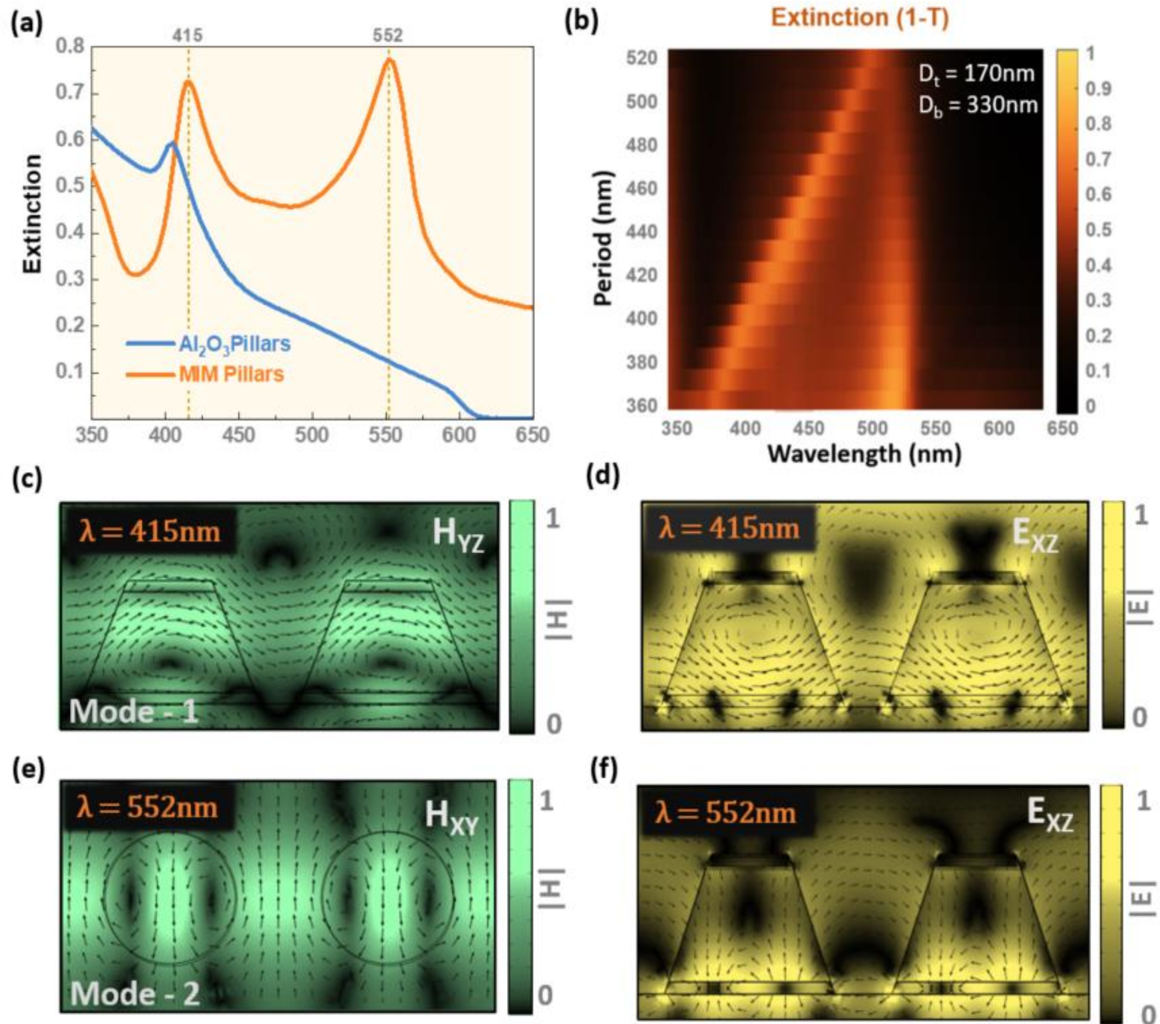

Figure 4.5: (a) Extinction plot comparison of Al_2O_3 pillars and MIM pillars. (b) Dependence of modes on array period. (c) Magnetic field distribution in YZ plane at λ1 (d) Electric field distribution in XZ plane at λ1. (e) Magnetic field distribution in XY plane at λ2 (f) Electric field distribution in XZ plane at λ2. The arrows in the field plots represent the corresponding field vectors. These simulations done in collaboration with Lyuye Lin.

A 'magnetic-anapole-like' mode (referred to as 'Mode-2') can be identified from the magnetic and electric field distributions in the XY and XZ planes in Fig. 4.5(d,e) at 552nm. We see two circulating magnetic fields in the XY plane, similar to a typical anapole mode, while the electric field enters and exits through these circles along the XZ plane. The field is observed between the two pillars, as opposed to the basic anapoles reported, where the field is concentrated in a single dielectric nanostructure[165]. The magnetic vectors depict two opposite circulating fields between the pillars, while the electric field vectors

enter one pillar and exit the other. As a result, the modes are considered as collective response of the metasurface.

We investigated the dependence of these modes on periodicity because both modes are reliant on the gap between the pillars. Fig.4.5(b) represents the extinction data of nanopillars for various periods ranging from 350nm to 520nm. Mode-1 red shifts with periodicity, whereas Mode-2 shifts to longer wavelengths for periods less than 440nm and then shifts to shorter wavelengths. When P > 500nm, the two modes appear to converge and become indistinguishable.

Experiments

MIM nanopillars were fabricated as described in section 4.1 with few changes in the parameters to obtain a truncated cone like geometry. Using e-beam lithography, an array of holes of diameter 300nm were patterned in an area of 500µm X 500µm. To get truncated cone like structures, high dosage (400µC/cm2) and short development time was employed. After the writing, the gold layer was etched with standard gold-etch solution. The samples were developed in a solution of 3 parts of Methyl Isobutyl Ketone (MIBK) and 1 part of Isopropanol (IPA) for 15 seconds. 20nm of Ag, followed by 185nm Al_2O_3 and 20nm of Ag were deposited using e-beam evaporator. Lift-off of PMMA was done using acetone. This process produced standing MIM pillars with truncated-cone like geometry. Six samples with varying array periods from 400nm to 480nm were fabricated by this process.

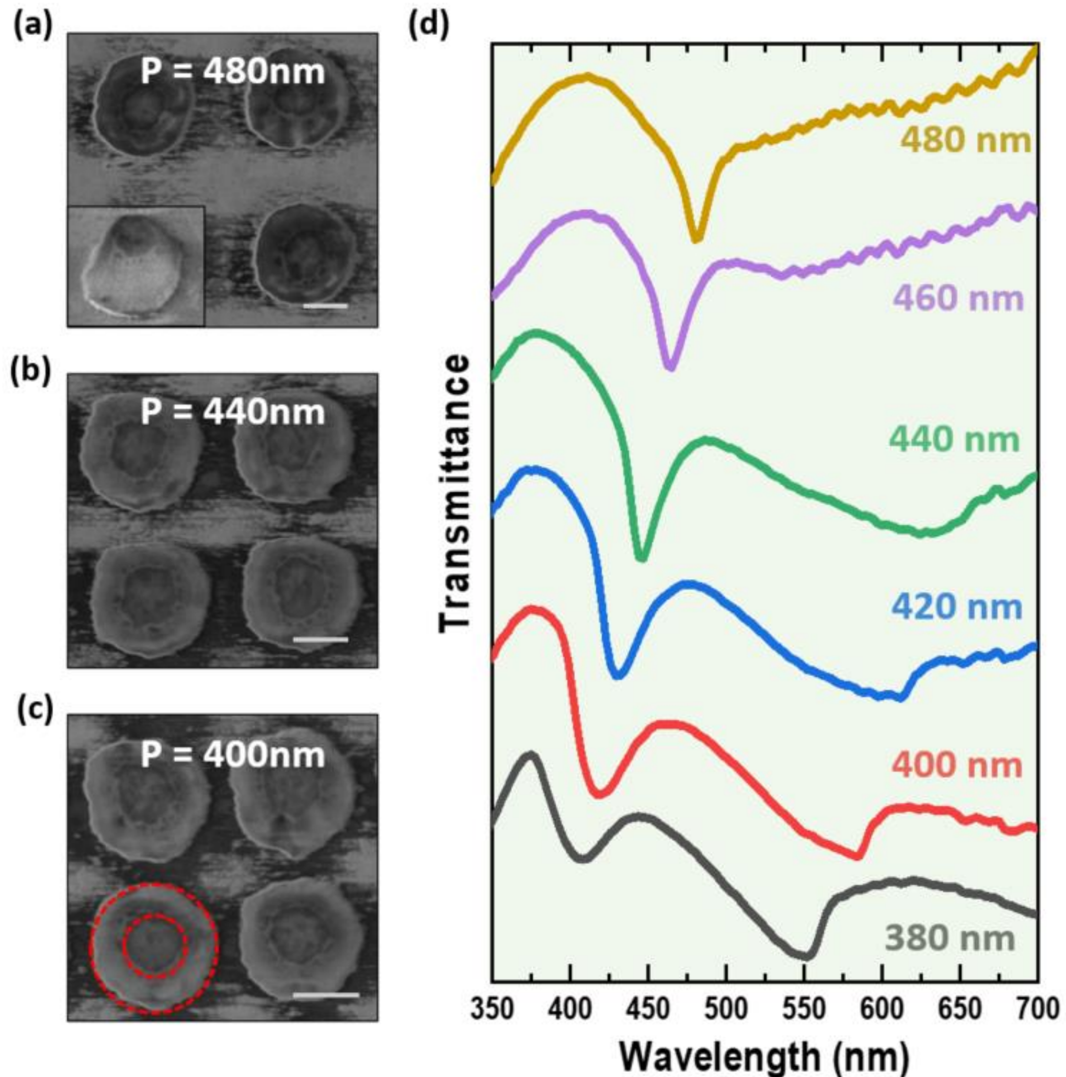

Figure 4.6: SEM images of fabricated truncated cone like pillars of periods (a) P= 480nm (b) P = 440nm (c) P = 400nm. Inset shows the geometry of the pillars. Scale bar is 200nm. (d) Extinction plot comparison of Al_2O_3 pillars and MIM pillars. (c) Transmittance plot illustrating the dependence of modes on array period.

Figs.4.6(a-c) shows the SEM images of the nanopillars with different periods, 400nm,480nm and 480nm respectively. The inset in Fig.4.6(a) shows the truncated cone geometry of the fabricated pillar. The red dotted circles in Fig.4.6(c) indicates the bottom and top diameters which are around 330-340nm and top diameter of 160-170nm respectively. Transmission data was recorded and plotted in Fig. 4.6(d). We have excellent agreement with the simulation data. The mode dependence on periodicity follows the same trend as predicted from the simulations. Mode-2 appears to be stronger than mode-

1 for P < 420nm and for higher periods, it is reversed. Both modes clearly red shifts with period till P = 440nm. Mode-2 starts shifting towards shorter wavelengths for P > 440nm. Both the modes eventually merge to one mode. The quality factor of the peak at Mode-1 increases with periodicity while the Mode-2 peak gets broader.

Dipole resonances shift to longer wavelengths with increase in diameter. Therefore, only higher order modes appear in the visible spectral range for diameters larger than 250nm. As in our model, we have dipoles corresponding to bottom diameter D_b = 350nm and top diameter D_t = 160nm. The higher order modes corresponding to D_b = 350nm fall in visible region and interact with dipole modes of D_t = 160nm. The magnetic-anapole-like and anapole-like modes shown here result from the superposition of two or more multipolar modes with leads to destructive interference in far field radiation.

4.3. Conclusion

The dipole resonance in MIM nanopillars and their dependence on the diameter of the pillars were experimentally shown. Magnetic-anapole-like and anapole – like modes were excited in a low dielectric material (Al_2O_3) by utilizing the metal-insulator-metal configuration. We fabricated truncated cone like structures to experimentally demonstrate these modes. Their dependence on the array period was illustrated with simulations and experiments.

Chapter 5

NANOPOROUS METAL FILMS

What's life without whimsy?

- Sheldon Cooper

In this chapter, we present a lithography-free large area dry-synthesis process to produce nanoporous metal films. The fabrication process along with the morphological characterization and purity analysis is discussed. Surface enhanced Raman spectroscopy is performed on one of these films to check the effect of the field enhancement.

5.1. Introduction

The ability to confine light to nanometer scale of plasmonic nanostructures has been exploited in several applications[12,46,46,51]. Different configurations like nanoparticles, array of metal nanopillars, thin metal nanofilms etc., have been used to achieve this. One system of strong current interest in this field are Nanoporous metals (NPM)[175-177]. These materials provide nano-size pores which can act as hot spots to generate high localized energy fields or thermal radiations. They also provide large surface to volume ratio along with high density of surface energy atoms at curved surfaces. Nanoporous metals have been successfully implemented in several applications in sensors[178,179], catalysis[180], energy conversion[181,182], spectroscopies[183,184] etc.

There are several methods to synthesize nanoporous metals. The most used techniques are templating, dealloying and chemical synthesis[185]. Templating involves using a pre-porous polymer as a sacrificial layer and depositing metals using electrochemical deposition or sputtering[186-188]. The polymer is later etched completely to obtain NPMs. Dealloying process is the most widely used NPM synthesis technique[189-191]. Basically, in

this process, the less stable metal is selectively etched from an alloy. For example, Ag-Au alloys are used from which Ag is removed to obtain nanoporous Au films[192]. Wet chemical synthesis involves reactions like reduction of metal salts to form metal nanoparticles which are then aggregated to form nanoporous structures[193,194]. Even though these techniques are effective, they are either time-consuming (templating) or contain impurities (dealloying) or cannot produce long connected curved structures (wet synthesis).

Here, we present a process which is fast, gives highly pure films and provides long connected networks. We fabricate NPMs with 6 metals namely Au, Ag, Platinum (Pt), Palladium (Pd), Iridium (Ir) and Nickel (Ni).

5.2. Fabrication

The technique used to prepare nanoporous metal films is a straightforward approach without incorporating any wet chemical process steps. Different metal layers were deposited using an e-beam evaporator on a sacrificial polymer which is later etched by plasma to produce a nanoporous film (NPF). Polymethyl methacrylate (PMMA) is spin coated on a clean Si substrate to produce films of thicknesses in the range of 100-150nm. The PMMA coated substrates are mounted on an inclined substrate holder in the evaporator. Metal films (Au, Ag, Pt, Pd, Ir, Ni) of 10nm thickness were deposited at different deposition rates depending on the type of the metal. The deposition rate and the angle of inclination of the substrate holder plays a crucial role in deciding the nanoporous ligament and pore sizes. These parameters are selected in such a way that the sizes of the deposited particles are big enough to form gaps between each other, at the same time not too large to facilitate nano-sized pores. These narrow gaps are required to access the underneath PMMA layer in the later steps. For example, Au films are deposited at an angle of 60° with 0.3 A°/s rate whereas Ni films were deposited at 80° angle at lower rate of 0.1 A°/s. After the deposition, the films were treated with nitrogen plasma of 200W power for 10 minutes using a basic tabletop plasma cleaner. During this step, the plasma attacks the PMMA layer beneath the metal particles slowly shrinking the

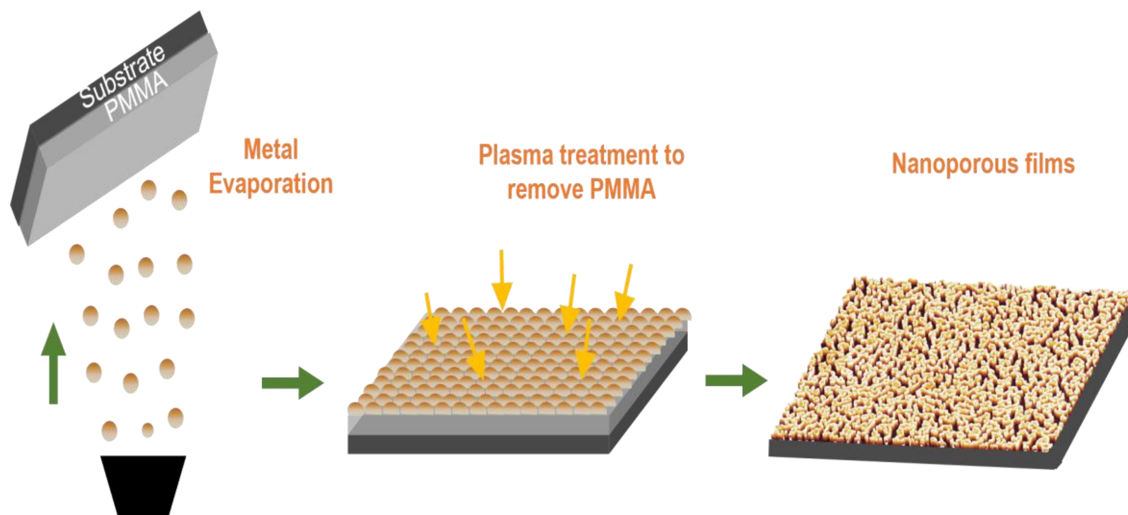

Figure 5.1: Schematic illustration of preparation of the nanoporous metal films.

PMMA layer. As the PMMA is etched, the metal particles on the layer merge with neighboring particles and form nanoporous metal films as shown in Fig.5.1.

5.3. Characterization

The morphology of the fabricated nanoporous metals is checked with SEM. We achieved good quality of nanoporous films as shown in Fig.5.2. The films have different pore and ligament sizes (width of the connecting wires) depending on the deposition conditions. Ag films have highest pore and ligament sizes of hundreds of nanometers. For the other films the pore sizes are around 10-50nm and ligament sizes from 8nm to 30nm. The low magnification images (Fig.5.2(a)) show that the films are well connected over large areas.

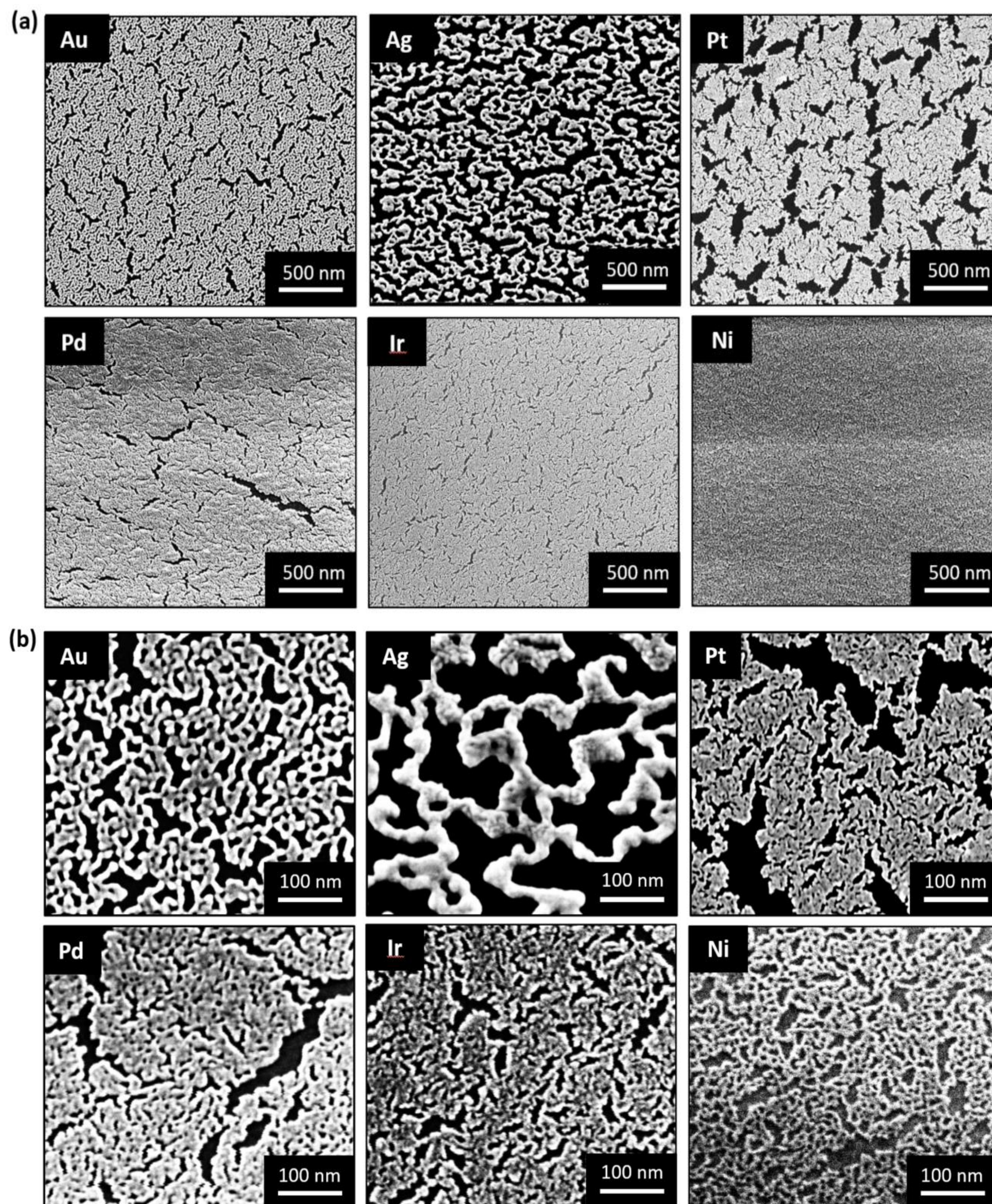

Figure 5.2: SEM images of fabricated nanoporous films of six metals shown at two different magnifications.

The purity and elemental analysis of the films was performed using High Resolution Transmission Electron Microscopy (HRTEM) And Energy Dispersive X-Ray Analysis (EDX). The NPF of Pd and Pt were prepared on TEM grids of 100µm^2 window of 100nm thick Silicon Nitride (SiN) membranes. Fig.5.3 shows the HRTEM image, along with the elemental maps of the NPF metal, Si (from substrate) and O (impurity). The EDX analysis showed that the carbon and oxygen content from the PMMA are negligible, which proves that the films fabricated have no residues of polymer.

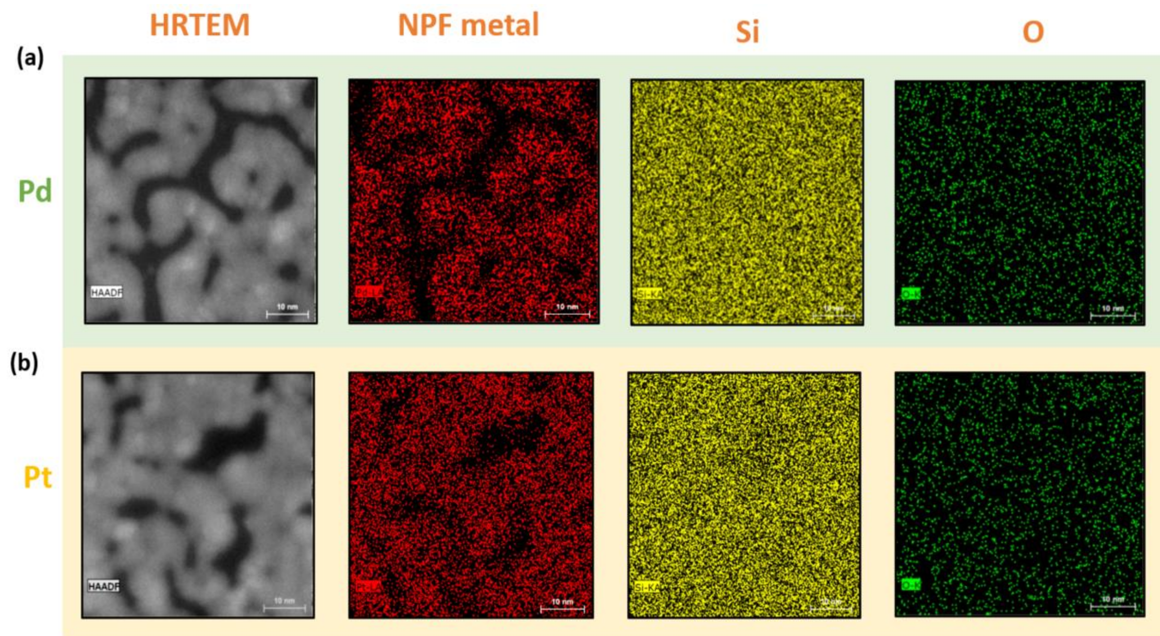

Figure 5.3: HRTEM images along with EDX analysis of (a) Pd and (b) Pt nanoporous films. Analysis performed by Rosaria Brescia.

Optical characterization and Surface Enhanced Raman Spectroscopy

One of the advantages of nanoporous metals is their light weight and increased transparency[175,195]. NPFs were fabricated on glass substrates using the same process steps and the transmission data is recorded. Fig.5.4 shows the increased transmission of Ag and Au NPFs compared to 10nm non-porous Ag and Au films respectively. Gold and silver nanoporous materials exhibit interesting optical properties due to their plasmonic nature in the visible spectrum. Plasmonic nanostructures confine light in subwavelength volumes and provide localized field enhancement, which can be used in spectroscopic applications to enhance the output signals. With Au and Ag NPFs, plasmonic hotspots can be generated to enhance the Raman scattering from molecules.

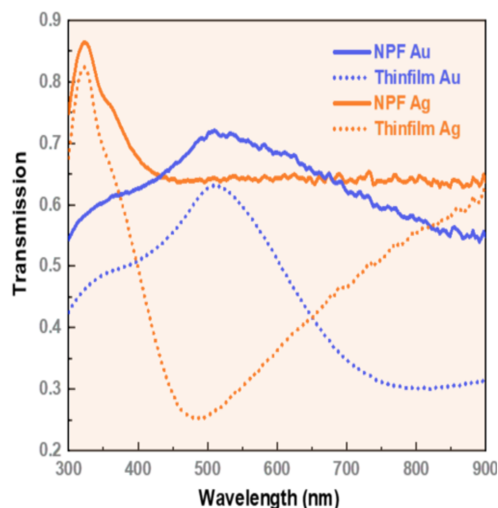

Figure 5.4: Transmission plot of nanoporous Au and Ag films along with non-porous 10nm Au and Ag

We use Rhodamine 6G (Rh-6G) molecule as an analyte to check the SERS signal from nanoporous Au films. Equal quantities of 50µM solution of Rh-6G are drop casted on plain Si substrate and NPF Au substrate. The Raman signal from the samples is recorded for laser excitations of wavelength 632nm of spot size about 1-2µm^2 for 2s of integration time. We calculated the enhancement factor (EF) as the ratio of intensity on Au NPF substrate to the normal Si substrate for the characteristic peaks.

$$EF = \frac{Raman\ Intensity\ on\ NPF\ substrate}{Raman\ Intensity\ on\ Si\ substrate} \quad (5.1)$$

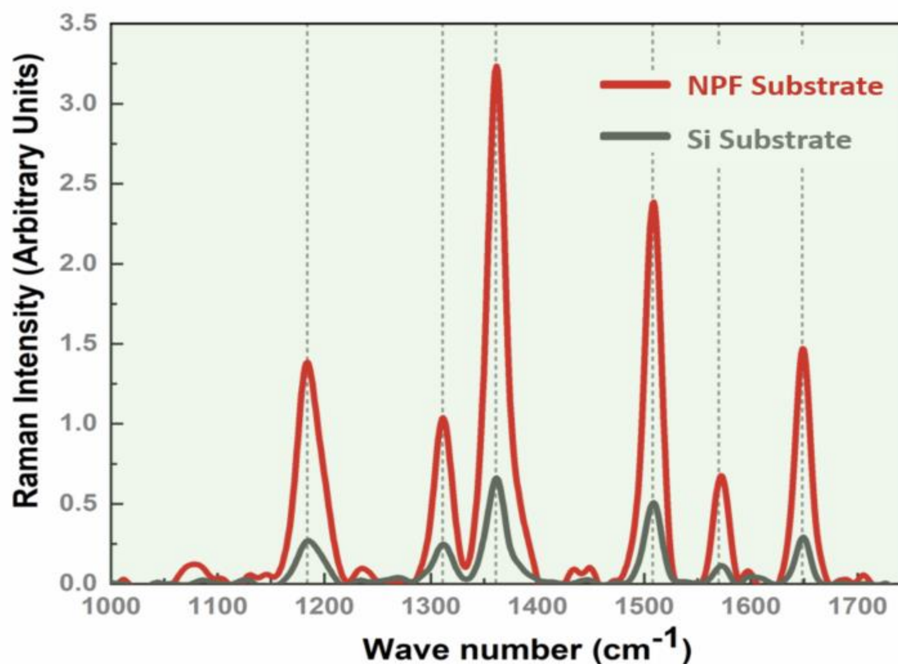

Figure 5.5: Raman measurements of Rhodamine-6G on Au NPF substrate and on Si substrate

The enhancement factor obtained was in the range of 4.2 to 4.5 for different peaks. This signal enhancement can be attributed to generation of plasmonic hot spots due to excitation of localized surface plasmon resonances in the metal. Even though the signal enhancement is not as significant as the reported results, one could improve the performance by fabricating much thicker nanoporous metals.

5.4. Conclusion

We presented a simple dry synthesis technique to produce nanoporous metal films. The quality of the films in terms of morphology and purity are verified using standard and high-resolution electron microscopic techniques. The plasmonic nature of the gold nanoporous films was exploited to enhance the Raman signal from Rhodamine 6G molecule.

Chapter 6

Conclusion

12 years after high school and I'm still at the nerd table

- Leonard Hofstadter

This thesis provided a detailed report on the change in optical properties of Metal-Insulator-Metal (MIM) nanocavities when they are laterally confined. Starting from microstructuring of MIMs as grating we studied the effects of lateral confinement in MIM nanopillars.

Using the grating MIM configuration, we were able to determine the spatial resolution of the MIMs to provide unperturbed ENZ response. This knowledge can be used in manufacturing MIM based ENZ pixels similar to MIM based Fabry Peròt color filters. Pixels containing four filters of unit sizes 4μm^2 can be constructed which are comparable to present day display technologies. A white emitting material can be placed on the Grating MIM with four different resonances to produce selective enhanced spectral response from specific sites.

Talbot Lithography introduced in chapter-3 can be used as a cost-effective alternative to several nanopatterning techniques. The Displacement Talbot lithography which is commercially used has multiple components to achieve the nano patterns at talbot distances. With our approach, different designs corresponding to different orders of diffraction can be achieved with a single photomask. MIM micropillars can be used to improve the photo response of emitters as they provide enhancement due to Purcell effect (due to cavity response) and lattice effects (due to periodic array of pillars).

The dipole resonance in MIM nanopillars were exploited to excite intriguing modes like ‘Magnetic-anapole-like’ and ‘Anapole – like’ mode. Unlike several reported studies in which high index materials were used, we excited these modes in a low dielectric material (Al_2O_3) by utilizing the metal-insulator-metal configuration. This was facilitated by the varying diameters in truncated-cone like nanopillar structures. This study can be used to achieve similar modes in other lower index materials by providing the necessary field confinement using thin metal layers.

A simple lithography free technique was introduced to produce nanoporous metal films. This technique provided high quality nanoporous films. Thicker nanoporous metal films can also be produced by careful selection of angle of inclination and deposition rate along with controlled plasma conditions. One can produce alloys consisting of different metals by using co-evaporation using our technique.

To summarize, this thesis provided insights on the optical properties of MIM micro and nanopillars to obtain ENZ and dipole resonances. We explored novel patterning techniques to facilitate cost effective, large area fabrication. Talbot lithography technique illustrated in Chapter-3 can be employed to produce large area photonic crystals and fractals with standard photolithography set-up. Similarly, fabrication technique provided in Chapter-5 can be used to produce large area nanoporous metals which can be integrated with biosensors to improve their performance.

APPENDIX

Simulation, Fabrication and Characterization Techniques

Engineers are just as smart as physicists

- Howard Wolowitz

A.1. Lumerical FDTD Simulations

Simulation is one of the important tools to design, model and analyze a device before investing time and money in manufacturing. It gives a chance to design the device with optimal parameters. All electromagnetic simulations in this thesis were done with *Lumerical FDTD Solutions*. This software uses Finite-Difference Time-Domain Maxwell's solver in 3D environment to analyze and provide reliable results for optical applications. It uses Computer Aided Design (CAD) environment which is user-friendly and consists a library of simulation objects and materials which can be designed according to the user's requirement. It also provides sweep routines, scripting capability and optimization routines[196].

A.1.1 The Finite-Difference Time-Domain Method

The Finite-Difference Time-Domain (FDTD) technique was first devised by Kayne S. Yee in 1966[197]. It is a numerical finite difference method for solving Maxwell's equations which quickly became a standard tool for modelling electromagnetic systems. Finite difference method is a numerical approach in solving differential equations. Time-domain refers to the use of time-differentiable finite difference equations while Finite Difference Frequency Domain methods uses frequency-differentiable equations. Due to its straightforward implementation, FDTD can be used to solve complicated problems particularly those with component dimensions in wavelength orders[198].

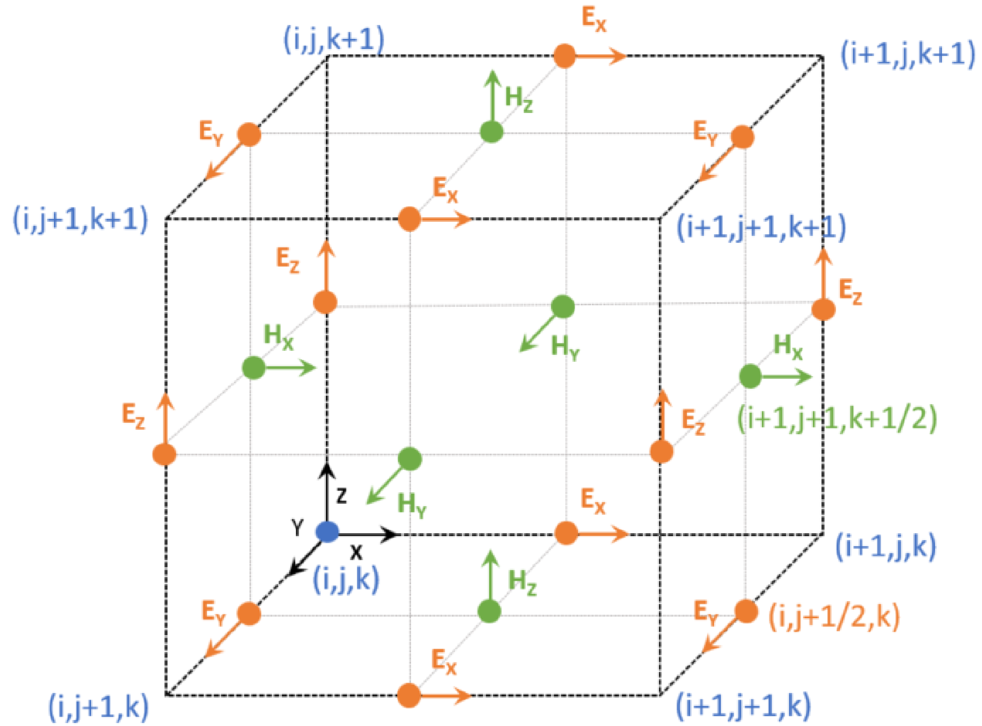

Figure A.1: Illustration of a 3D Yee lattice. The electric and magnetic field vectors are represented in orange and green respectively. Different nodes of the lattice are indicated in blue, and the example nodes of electric and magnetic fields are given in the respective field colors.

The FDTD method is a grid-based differential method. It solves the following time-dependent Maxwell's time-dependent equations[199],

$$\nabla \times E = -\frac{\partial B}{\partial t} \tag{2.1}$$

$$\nabla \times H = -\frac{\partial D}{\partial t} \tag{2.2}$$

$$\nabla . D = 0 \tag{2.3}$$

$$\nabla . B = 0 \tag{2.4}$$

using finite difference methods. Yee lattice, termed after its creator is the grid system of nodes used in this method. The Yee lattice grid can be seen in the Fig.2.1. The electric field vectors are positioned at the center of the edges and oriented in the direction of the edge. The magnetic field vectors are placed at the centers of the faces and orthogonal to the plane of the face. This facilitates the overlap of electric and magnetic fields and fills the lattice with interlinked Faraday's law and Ampere's law contours. The various nodes of the Yee lattice hold values of either the electric or magnetic field which are calculated at every discrete half-time steps taking into account the value of neighboring nodes following a leapfrog scheme[200].

A.1.2 Simulation environment and boundary settings

To set-up the simulation in order to produce reliable results, it is important to consider several factors like the mesh size, boundary conditions, source type etc. In Lumerical FDTD Solutions software, the library generally has different geometrical objects, material database, monitors, sweep tools etc. In general, to set-up a simulation, one needs to define a set of objects, simulation region, boundary conditions, source and monitors which is saved as a model. The geometrical and structural parameters of each object can be defined by the user easily such as the material type, dimensions, and the position. It is also possible to import experimental data (refractive index, n+ik) to the existing material database.

The typical simulation set-up used for most of the simulations in this thesis is shown in the Fig.2.2. A 3D simulation region is defined as shown in the perspective view of Fig.2.2. As in this thesis, a periodic array of elements is studied, periodic boundaries are set in the X- and Y- directions. A Perfectly Matched Boundary (PML) is used in the Z- direction. This reduces the reflections from the top and bottom boundaries. As the waveform propagates towards the grid boundary, it is simulated as if it is propagating to infinity to eliminate undesired interference.

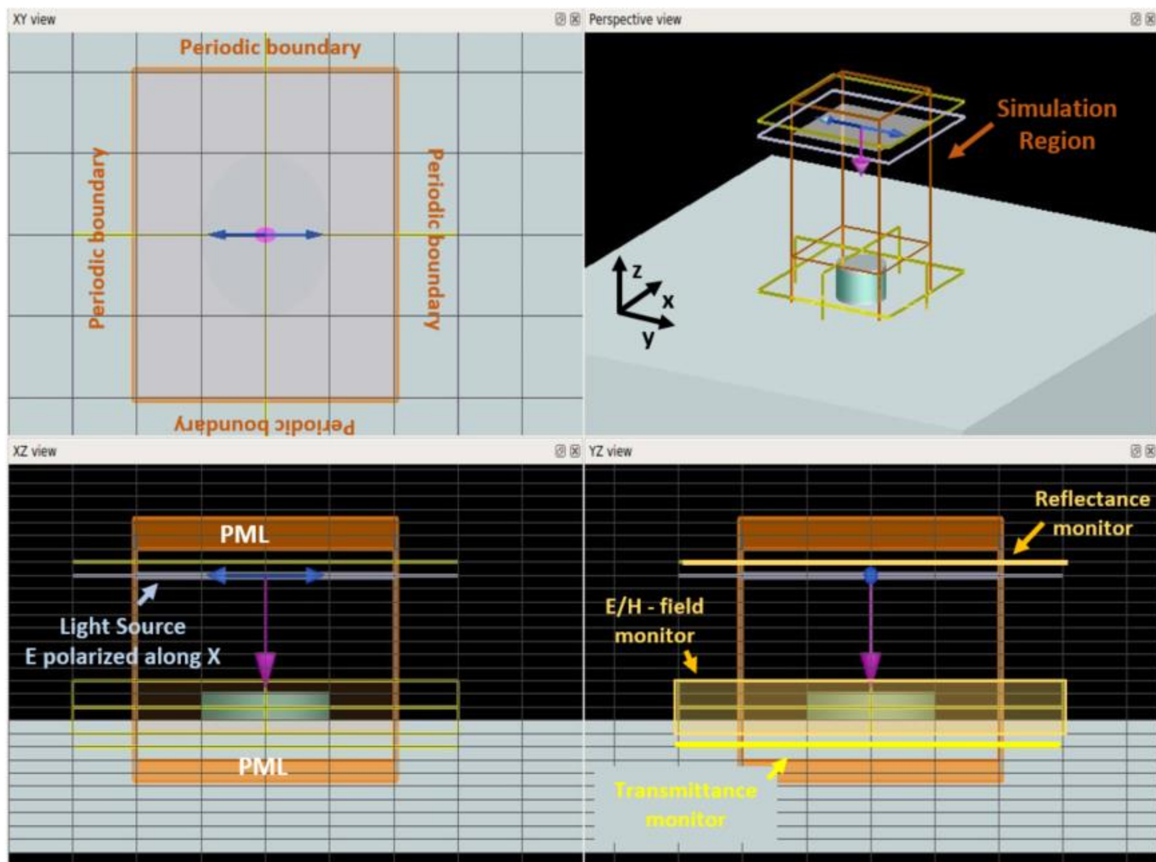

Figure A.2: Lumerical simulation set-up of 2D array of pillar structures. Each window shows the XY view, Perspective (3D) view, XZ-view and YZ-view of the model.

A plane wave light source is used to illuminate the objects. The frequency, direction, polarization, position of the source can be defined as per the user's requirement. Two-dimensional frequency-domain field monitors are added inside the simulation region at top and bottom of the structures to record transmittance and reflectance data. To record the electric and magnetic fields inside and around the structures, extra 2D frequency-domain field monitors are added in different planes to get the specific field distributions. There is a possibility to add index monitors which allow the user to check the refractive indices of the objects in the model. The data obtained after the simulations can be easily collected and saved, for example reflectance data can be saved as in JPEG format or as a text file. There is a possibility to write scripts if one needs to sweep a parameter in a specific region. For example, the diameter of the pillars can be swept from 200nm to

500nm in the steps for 10nm and the reflectance data can be recorded and plotted. The configuration of all the simulations shown in this thesis have the similar set-up as shown and described in this section.

A.2. Fabrication Techniques

A.2.1. Electron Beam Evaporation

Electron-Beam evaporation (e-beam evaporation) is a type of Physical Vapour Deposition (PVD) techniques used to controllably deposit thin films[201]. It is carried out in high vacuum conditions and is done in four steps, evaporation, transportation, reaction and deposition. Unlike Chemical Vapour Deposition (CVD)[202], evaporation has the advantage that it does not produce any hazardous by-products and is a high-quality non-contaminating process. The electron-beam used to melt the samples is guided by a magnetic field and can be scanned across the source and be accelerated to desired values. This gives a high controllability of the deposition rate and utilization of the source material.

Two different evaporators were used in the course of this thesis, Kurt J.Lesker PVD75 e-beam evaporator and Kenosistec KE500ET e-beam/thermal evaporator. A schematic of e-beam evaporation process is shown in the Fig.A.3. The typical process involves bombardment of the electron-beam produced from a charged tungsten filament with the target material (to be deposited). This converts the target material from solid state to gaseous state which eventually evaporates and deposited on the substrate. In order for this process to happen, high energy electrons are required. The thermionically emitted electrons from a hot filament are accelerated and steered using the magnetic fields, so that when they hit the target, they possess enough energy flux to evaporate the material[203].

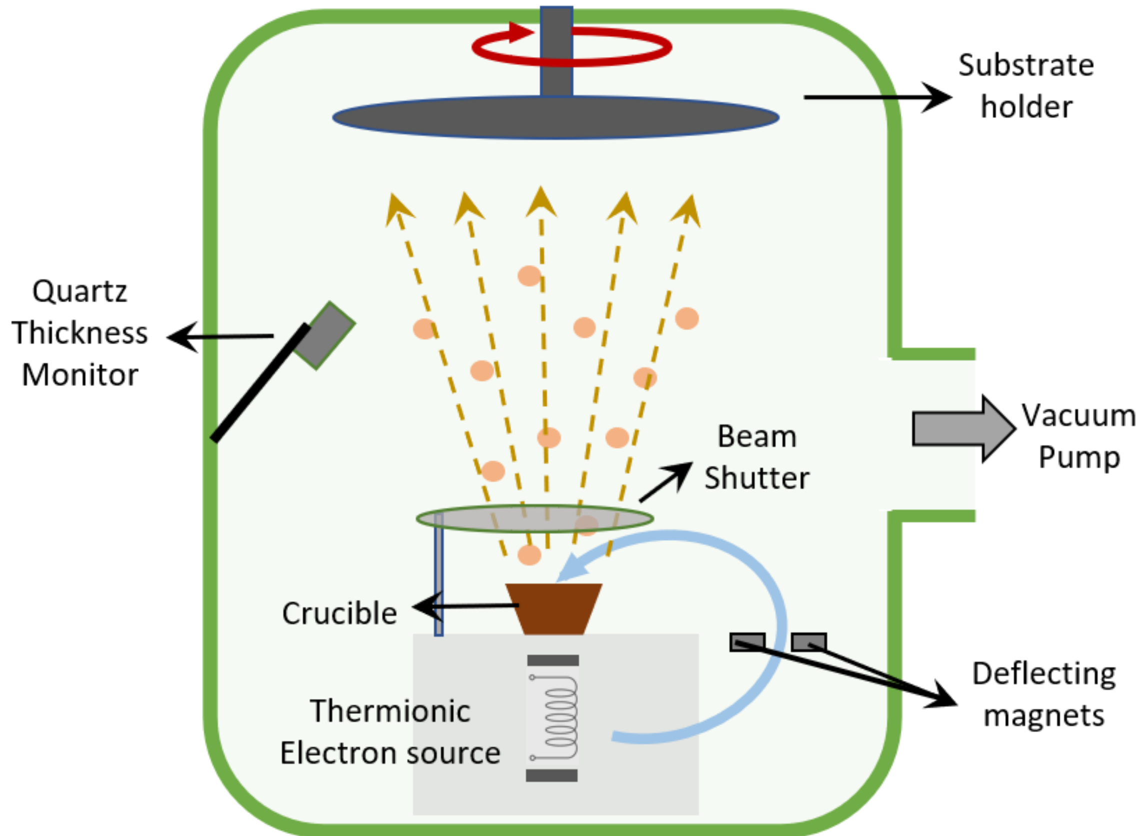

Figure A.3: Schematic of an e-beam evaporator

A quartz thickness monitor with a feedback control loop is used to control the deposition rate of the materials. The crucible containing the evaporation materials are water cooled to confine the heating to only the area occupied by the source material and eliminating any unwanted contamination from neighboring components. Typically, 10kW electron beam source at 1 x 10^{6} Torr pressure were used for depositing the materials in this thesis. The deposition rate was selected according to the thickness and type of the films required.

A.2.2. Photolithography

Photolithography is one of the widely used fabrication processes to pattern the substrates. It rose to significance in 20th century as the drive to miniaturize the semiconductor technology has been satisfied by improving the resist and exposure

parameters[204-206]. It is classified as contact or non-contact lithography depending on whether the mask and the substrate are in contact with each other or not. It can be further categorized as Optical lithography or UV lithography depending on the wavelength of the light source. In this thesis, UV contact lithography (365nm) was used to fabricate the samples.

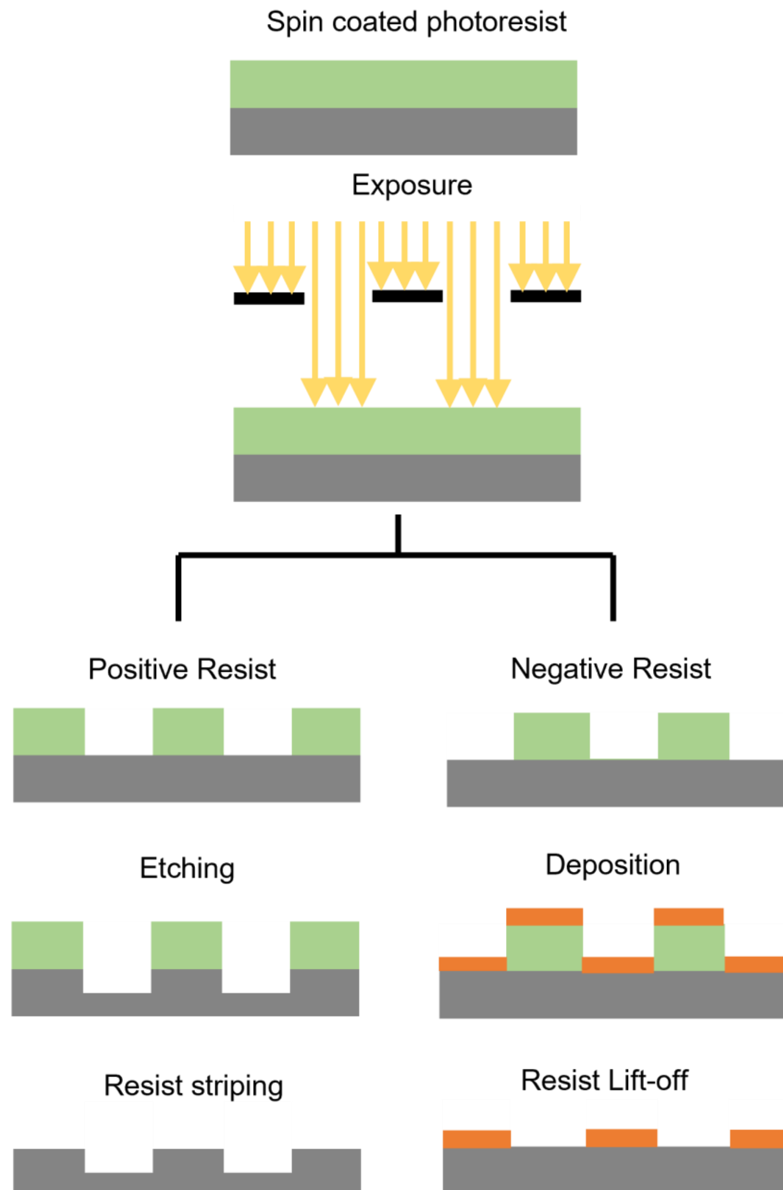

Figure A.4: Photolithography and steps involved to fabricate the desire samples. Left branch shows the etching process steps and right branch depicts the lift off process.

Photoresist is a light-sensitive material used in photolithography to create patterns on the substrate. There are two types of photoresists, positive resist or negative resist depending on how they react with the developer after being exposed to the light[207]. A photomask, with a prefabricated pattern is used to replicate the same design onto the photoresist. Positive resists are those having the light-exposed areas soluble in a specific solvent (this process is called developing). This is facilitated by a photo-induced chemical reaction that breaks the polymer chains to make them more soluble. On the other hand, in negative resists, photons induce cross-linking of polymer chains making it difficult to be soluble in the developer. This results in obtaining an inverse of exposed pattern on the resist. Depending on the application, resists are chosen. Once the resists are patterned, one can either use it as etching mask or a deposition mask. In case of etching, the resist is removed after the desired etch to get patterns on the substrate. When used as a deposition mask, the resist is used as shadow mask and the removed (lift-off) to get a pattern made of the deposited material.

In this thesis, two positive resists from MICROPOSIT SERIES, S1813 and AZ5214E were used. S1813 is positive resist which when spincoated at 4000rpm forms a thinfilm of around 1.5µm thick. After exposure, it can be developed using MF319 developer. AZ5214E is less concentrated solution which forms a film of 1µm when spinned at same speed and can be developed using AZ726 developer. We used lift-off process to remove the resist mask after depositing the desired thin films. A much-detailed explanation on the fabrication steps are provided in coming chapters.

A.2.3. Electron beam Lithography

Even though with optical lithography, we obtain large-area patterns, the minimum feature size is limited by the light diffraction limit. Current state-of-the-art photolithographic tools use deep ultraviolet (DUV)[208] or extreme ultraviolet (EUV)[209] light to allow minimum feature sizes down to 50 nm and 5 nm, respectively, but they are still under development for commercial use. Electron Beam Lithography (EBL) uses a focused beam of electrons to expose specific areas of radiation-sensitive resists. Electrons have wavelengths in the range of 0.2 - 0.5 A°, which makes it possible to obtain much smaller feature sizes than photolithography[210,211].

The EBL system used for fabricating samples in this thesis is Raith 150 TWO ultra-high resolution electron beam lithography and imaging system. The schematic of major components in an EBL system are outlined in Fig.A.5. The EBL system mainly divided into two parts, the pattern generator, and the deflection and astigmation controller. The main components of the system are (i) an electron gun - a source to generate electrons, (ii) electromagnetic lenses- to align and collimate the beam along the path and reduce its energy spread, (iii) blanking electrodes – to turn on and off the beam, (iv) apertures – to maintain the beam size, (v) deflection control – to deviate the beam while writing, (vi) astigmation corrector – to adjust the focus of the beam and correct the aberration and (vii) an electron detector to image the sample.

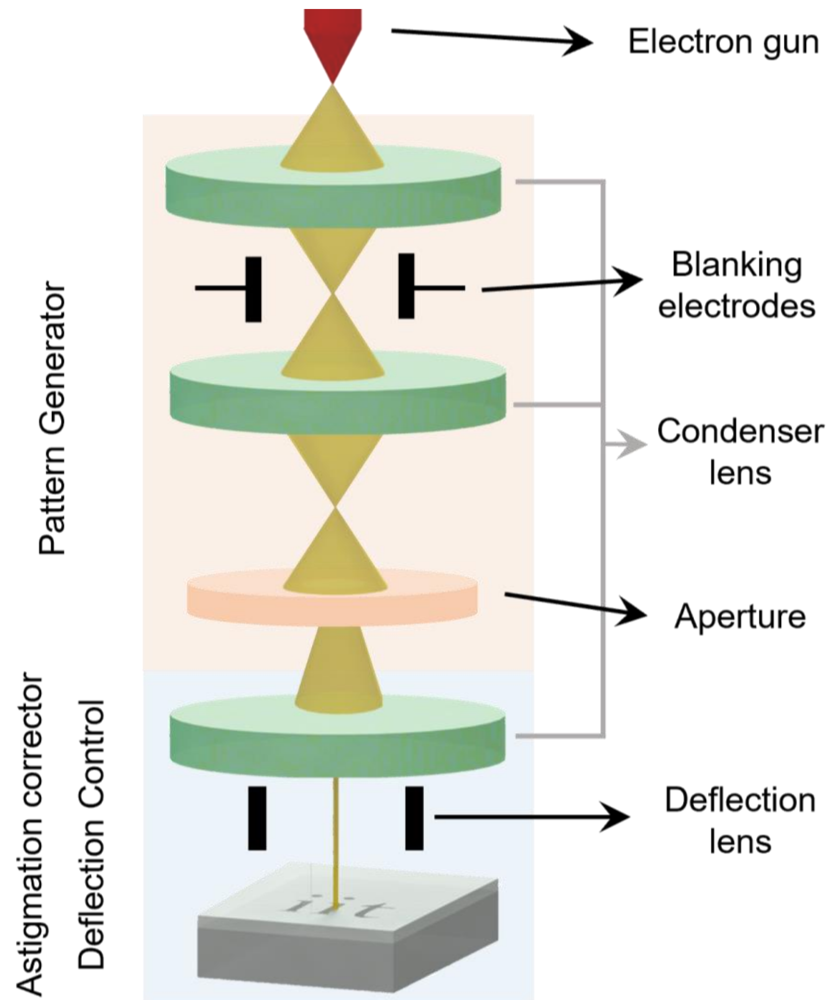

Figure A.5: Schematic diagram of typical EBL system along with its major components.

The EBL column, which consists of all the components to generate the desired beam is at higher vacuum (typically 10^{10} torr) than the wafer loading/unloading system (10^{7} torr). The EBL system is placed on an anti-vibrational table in a thermally and electromagnetically insulated room as it is very sensitive to environmental conditions.

There are two ways to generate electrons, thermionic emission (heating) and cold cathode emission (electric field). The Raith 150 TWO system uses a thermionic source, a tungsten filament. When the supplied energy is higher than the metal work function, the free electrons from the metal tunnel through the electrostatic potential barrier and leave the emitter. Once the electrons leave the gun, they are subjected to several focusing and limiting processes to get a very small spot size with good energy spread.

There are different process parameters to be considered while patterning using EBL. One of them is the electron resist to be used. Similar to photoresist, electron resists can be of two types, positive and negative depending on its solubility after undergoing the exposure. A positive resist undergoes physio-chemical changes to make the exposed areas soluble in the developer. In this thesis, a positive resist, Poly methyl methacrylate (PMMA) is used to pattern the samples. The resist thickness plays an important role in obtaining good features. Depending on the application, different concentrations of PMMA, spincoated at different speeds are used to obtain desired patterns. The exact parameters for fabricating different samples are outlined in corresponding chapters.

While writing the pattern, one important parameter to consider is the "dose". It is defined as the number of electrons per unit area which is measured in $\mu C/cm^2$ units. The higher the dosage, the longer it takes to complete a specific pattern. Typically, 100-600 $\mu C/cm^2$ doses are used according to the design. Higher doses imply high solubility of the resist (positive) after exposure. However, using a higher dose can result in over exposure of the sample due to proximity effects. When the electron beam hits the substrate, it undergoes electron-matter interactions resulting in scattered electrons. These scattered electrons expose the areas which are not part of the design, resulting in disruption of the original design[212]. As a rule of thumb, lesser dosages are used for smaller feature sizes.

After exposing, developing the sample using the right developer and for optimum time is very important. For PMMA resist, Methyl Isobutyl Kethone (MIBK) is used as a developer. Higher development times results in over development, which means even the parts slightly exposed due to proximity effects are developed. Low development times, results in under development, by not completely removing the exposed resist. So, according to

the dosage and the minimum feature size, development time plays a critical role to obtain optimal results.

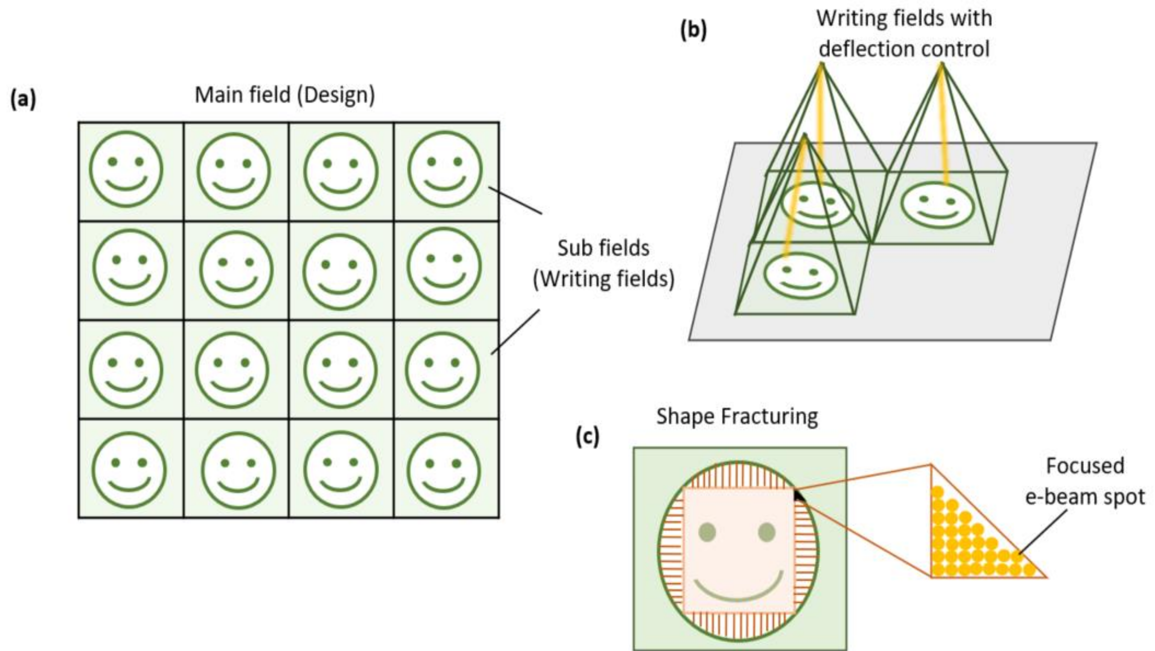

Figure A.6: Fracturing of the design. (a) Layout fracturing (b)Deflection control over individual writing fields (c) Shape fracturing and depiction of individual beam shots in a fractured element

To design the masks (to be written on the resist), RAITH150-TWO Nanosuit software was used to create and edit the CAD files which are saved and implemented in GDSII file format. The dose to be used will be indicated in the design. The GDSII fracturing processor reads the file and decomposes the large design (main field) by the user into several subfields called "writing fields". This is called layout fracturing. A writing field is the minimum area covered during the exposure by deviating the electron beam using the deflection controls before moving to a different point (A mechanical moving stage is used to move the sample). Within each writing field, the beam exposes the resist and write the rectangles and trapezoids (shape fracturing) that compose the pattern. Each shape is exposed by an array of individual beam shots as shown in Fig.A.6(c).

A.2.4. Reactive Ion Etching

Reactive Ion Etching (RIE) is dry etching technique to selectively remove a target material[213]. In this thesis, ICP-RIE SI 500 by Sentech instruments with CESAR RF power generator is used to fabricate few samples. Reactive etching is an isotropic chemical process which uses free radicals of the plasma to selectively remove the material. Ion etching is a physical (mechanical) process in which the ions bombard the target surface to etch it. This is anisotropic process with low selectivity. Reactive ion etching is a combination of reactive and ion etching thus incorporating the advantages of both the processes.

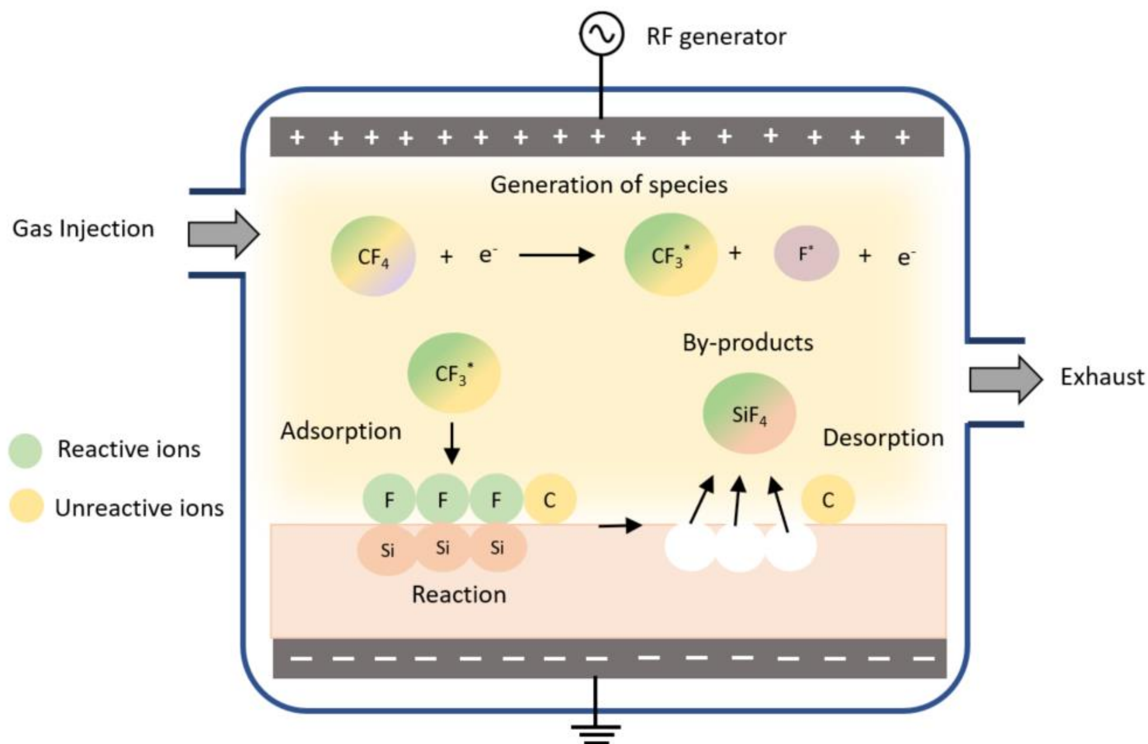

Figure A.7: Reactive ion etching process depicting the process steps involved in etching of Si substrate using CF_4 gas.

The RIE process can be divided into four steps, (i) Generation of reactive species, (ii) Transport and adsorption, (iii) Reaction and (iv) Desorption. A vacuum chamber is filled with reactant gas or gases. A strong RF (radio frequency) electromagnetic field is applied

to an electrode to create plasma. The oscillating electric field dissociate the reactants into electrons, ions and free radicals.

The substrate is positioned on a negatively charged electrode, therefore positively charged ions accelerate towards the surface bombarding the sample and causing physical etching. Reactive ions are adsorbed on the surface of the sample. These ions chemically react with the target material causing chemical etch. The reaction by-products are then desorbed from the surface and removed from the chamber.

To design an efficient RIE process, there are few parameters that must be considered to obtain good etch rate, selectivity and directionality. The RF power plays an important role in creating a very high plasma densities and determining the etch rate. The type of gas used must be selected according to the material to be etched to trigger the chemical reaction. For example, to remove silicon nitride layer, Carbon tetrafluoride (CF_4) or Sulphur hexafluoride (SF_6) gases are injected, while to etch a metal like aluminum, Silicon tetrachloride ($SiCl_4$) gas is used. The operating temperature also has to be monitored according to the sample and mask used.

A.3. Optical and Physical Characterization

A.3.1. Spectroscopic Ellipsometry

Spectroscopic ellipsometry is an optical thinfilm analyzing technique used to study the dielectric properties (changes in molecular properties when exposed to external electric field) of films. It gives information about refractive index, thickness, transmittance and other material and optical properties. It is used in a plethora of applications ranging from semiconductors[214], optical sensors[215], displays to biosensors[216].

The basic principle is to measure the change in the polarization of light when incident on the material of interest. Light is an electromagnetic wave with oscillating electric fields in different directions. If the direction of electric field oscillation is random, it is called unpolarized light. When the electric field oscillation traces a well-defined shape at any point and time, it is called polarized light[217]. Polarization can be classified in three

different types depending on the phase difference (ϕ) between the X and Y- components of the electric field.

1. Linear: ϕ = π.
2. Circular: ϕ = π/2.
3. Elliptical: ϕ = any other angle.

In Ellipsometry, we use elliptically polarized light to study the properties of the material. Ellipsometry can be single-wavelength or spectroscopic ellipsometry. There are many ellipsometry techniques in use, but the most used is Reflectance/Transmittance Ellipsometry. This technique analyses the change in polarization of the light when reflected/refracted through the material. Ellipsometry measures the complex reflectance ratio which is given by

$$\rho = \left|\frac{R_p}{R_s}\right| e^{i(\delta_p - \delta_s)} = tan\,\Psi . ei\Delta \tag{2.5}$$

where,

$$\left|\frac{R_p}{R_s}\right| = tan\,\Psi \tag{2.6}$$

$$e^{i(\delta_p - \delta_s)} = \Delta \tag{2.7}$$

Ψ is the angle whose tangent gives the ratio of the amplitude attenuation (or magnification) of the amplitudes of p-reflection to the s-reflection coefficients. Δ is the phase shift of the p- component of the polarization of the reflected beam with respect to the s- component. With these values, one can determine parameters like, permittivity (ε1,ε2), refractive index (n,k) and other optical properties of the material.

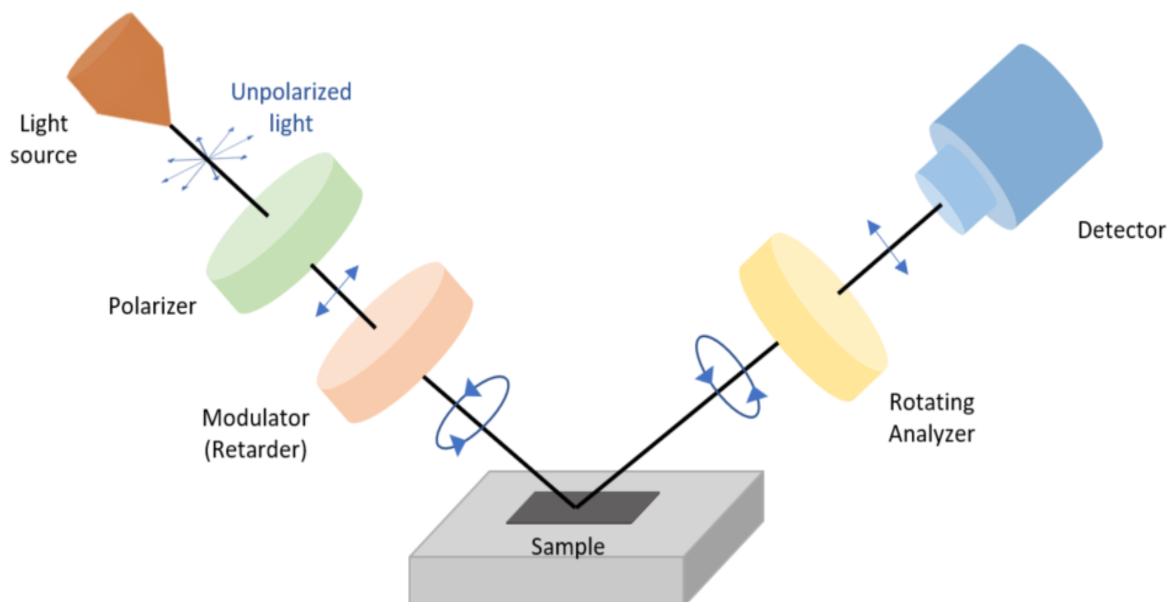

Figure A.8: Schematic of typical reflectance ellipsometry setup

The main components of an ellipsometer include a (i) light source, (ii) polarizer - to convert the unpolarized light to linearly polarized light, (iii) retarder – to convert linearly polarized light to elliptically polarized by introducing a phase delay, (iv) analyzer – receives the reflected signal and coverts to linearly polarized light and finally, (v) detector - an array of charged-coupled devices (CCD) to simultaneously monitor multiple spectral components. The ellipsometer used for characterization in this thesis was Vertical Vase ellipsometer by J. A. Woollam and the data is fit to extract the optical parameters using WVASE software.

A.3.2. Scanning Electron Microscopy

Electron microscopy is an imaging technique used to obtain high resolution images of specimen at nanoscale. This technique uses a beam of accelerated electrons as source to scan the samples. Having wavelengths much shorter than photons, electron microscopes offer high resolutions than light-based microscopies[218,219].

As mentioned earlier in section A.2.3, when electrons hit the target, they scatter elastically or inelastically. These scattering mechanisms produce different types of outputs like, Auger electrons, transmitted electrons, secondary electrons, back-scattered electrons, X-rays, cathodoluminescence etc. Each type of electrons contains different kind of information about surface topography and composition. For example, auger and secondary electrons (possess lower energies) gives information about the surface of the sample, while back-scattered electrons (have same energy as incoming electrons) penetrate more into the sample and can provide information from deeper part of the sample. Depending on the type of signals detected from the samples, different electron microscopies are classified.

The most used electron microscopes are Transmission electron Microscope (TEM) and Scanning electron Microscope (SEM). Transmitted electrons are detected and analyzed in TEM while reflected secondary electrons are used in SEM characterization. The schematic of the SEM system is shown in Fig.A.9. The main parts of the system are similar to the electron-beam lithography system. In fact, EBL is SEM with few extra components like deflection controls to write the pattern.

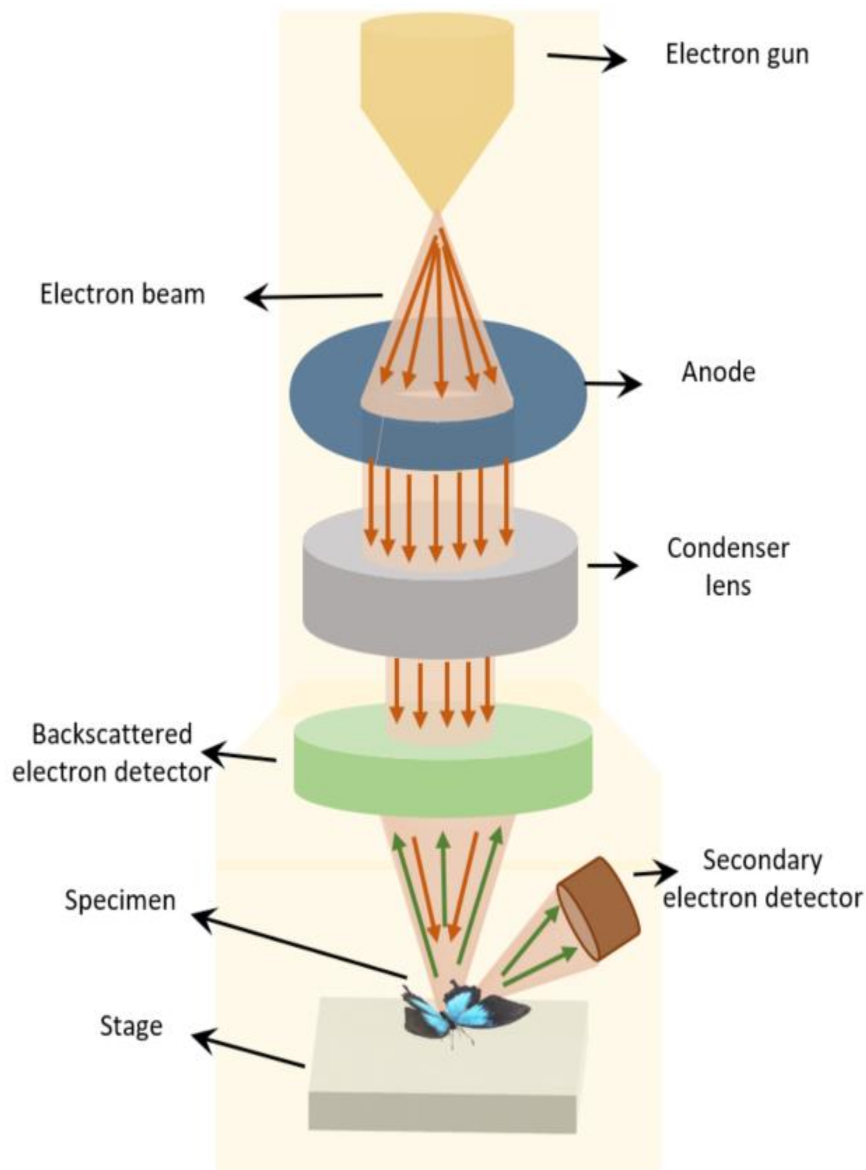

Figure A.9: Schematic of Scanning Electron Microscope

All the devices fabricated in this thesis were imaged using a FEI Helios NanoLab DualBeam 650 Scanning Electron Microscope. The SEM incorporated in the EBL system was also used to image few samples. Voltages ranging from 2kV to 20kV were used, depending on the samples. Secondary Electron Detectors in the system were used. In case of samples with glass substrates, a thin layer of 10nm Au was deposited using the e-beam evaporator to image the samples.

A.3.3. Atomic Force Microscopy

Atomic Force Microscopy (AFM) is a type of Scanning Probe microscopy (SPM) which uses a physical point probe to image the samples[220,221]. AFM has the advantage our other microscopic techniques as it can image even non-conductive samples with any damage to the samples. AFM can be operated in three main modes called, contact mode (static), tapping and non-contact modes (dynamic modes). In static contact mode, the sample and tip are in contact, and the cantilever moves as per the topology of the sample. In tapping and non-contact mode, the cantilever vibrates at a frequency which change according to the sample morphology.

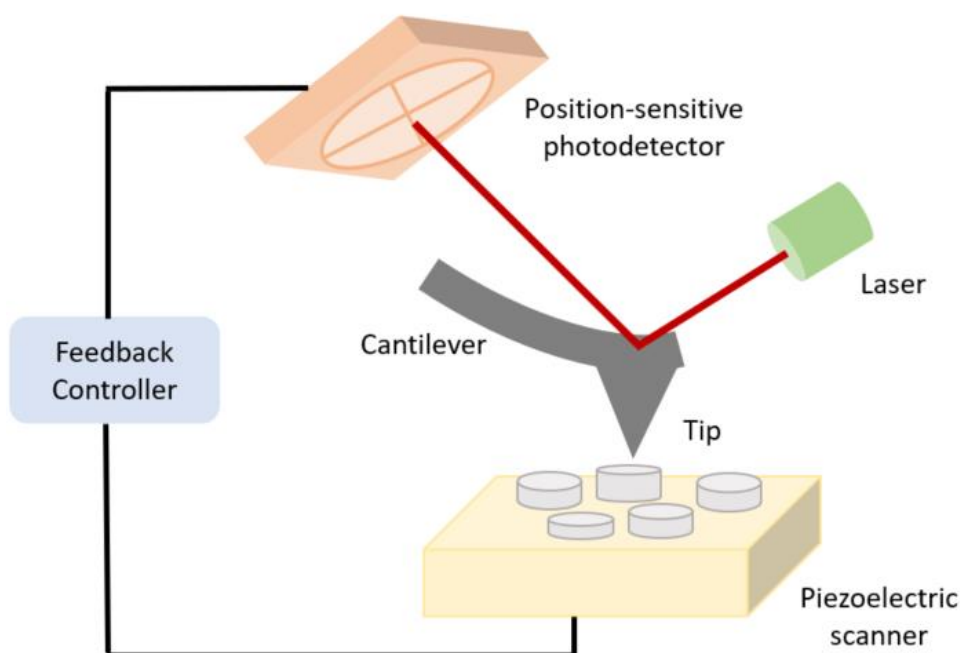

Figure A.10: Schematic of Atomic Force Microscopy.

A typical AFM mainly consists of (i) sharp tip – to probe the samples (ii) cantilever- to which the tip is attached and used to scan the sample (iii) laser – light source for optical signal (iv) photodetector – to read the optical signal (v) feedback controller and (vi) piezoelectric stage – to move the sample. AFM uses atomic forces to map the tip-sample interaction which change depending on the distance between the probe and the sample.

As the tip approaches the surface, the attractive forces between the surface and the tip cause the cantilever to deflect towards the surface. When the cantilever reaches a certain minimum distance from the sample, there are repulsive forces coming into the picture and the cantilever deflects away from the surface. These deflections are measured by the reflected laser beam from the top of the cantilever and are detected by a position-sensitive photodetector which maps the surface. The feedback control is used to maintain certain parameters constant during the imaging process. For example, the deflection of the cantilever can be kept constant, but changing the distance between the tip and sample. AFM system XE-100 by Park Scientific is used to obtain the AFM images reported in this thesis. All the images are taken in non-contact mode. Gywddion software was used for image analysis and processing.

REFERENCES

1. Barbillon, G., Nanoplasmonics: fundamentals and applications. BoD–Books on Demand: 2017.
2. Maier, S. A.; Atwater, H. A., Plasmonics: Localization and guiding of electromagnetic energy in metal/dielectric structures. Journal of Applied Physics 2005, 98 (1), 011101.
3. Fang, Y.; Sun, M., Nanoplasmonic waveguides: towards applications in integrated nanophotonic circuits. Light: Science & Applications 2015, 4 (6), e294-e294.
4. Atwater, H. A.; Polman, A., Plasmonics for improved photovoltaic devices. Nature Materials 2010, 9 (3), 205-213.
5. Haes, A. J.; Haynes, C. L.; McFarland, A. D.; Schatz, G. C.; Van Duyne, R. P.; Zou, S., Plasmonic Materials for Surface-Enhanced Sensing and Spectroscopy. MRS Bulletin 2005, 30 (5), 368-375.
6. Mejía-Salazar, J. R.; Oliveira, O. N., Plasmonic Biosensing. Chemical Reviews 2018, 118 (20), 10617-10625.
7. Mansuripur, M.; Zakharian, A. R.; Lesuffleur, A.; Oh, S.-H.; Jones, R. J.; Lindquist, N. C.; Im, H.; Kobyakov, A.; Moloney, J. V., Plasmonic nano-structures for optical data storage. Opt. Express 2009, 17 (16), 14001-14014.
8. Jiang, N.; Zhuo, X.; Wang, J., Active Plasmonics: Principles, Structures, and Applications. Chemical Reviews 2018, 118 (6), 3054-3099.
9. Zia, R.; Schuller, J. A.; Chandran, A.; Brongersma, M. L., Plasmonics: the next chip-scale technology. Materials Today 2006, 9 (7), 20-27.
10. Maier, S. A., Plasmonics: fundamentals and applications. Springer: 2007; Vol. 1.
11. Shahbazyan, T. V.; Stockman, M. I., Plasmonics: theory and applications. Springer: 2013; Vol. 15.
12. Amendola, V.; Pilot, R.; Frasconi, M.; Maragò, O. M.; Iatì, M. A., Surface plasmon resonance in gold nanoparticles: a review. Journal of Physics: Condensed Matter 2017, 29 (20), 203002.
13. Lee, K.-S.; El-Sayed, M. A., Gold and Silver Nanoparticles in Sensing and Imaging: Sensitivity of Plasmon Response to Size, Shape, and Metal Composition. The Journal of Physical Chemistry B 2006, 110 (39), 19220-19225.

14. Link, S.; El-Sayed, M. A., Size and Temperature Dependence of the Plasmon Absorption of Colloidal Gold Nanoparticles. The Journal of Physical Chemistry B 1999, 103 (21), 4212-4217.
15. Jackson, J. D., Classical Electrodynamics. Wiley: 2012.
16. Yariv, A., Optical Electronics. Oxford University Press: 1990.
17. Kittel, C., Introduction to Solid State Physics. Wiley: 2004.
18. Vinogradov, A. P.; Dorofeenko, A. V.; Pukhov, A. A.; Lisyansky, A. A., Exciting surface plasmon polaritons in the Kretschmann configuration by a light beam. Physical Review B 2018, 97 (23), 235407.
19. Koev, S. T.; Agrawal, A.; Lezec, H. J.; Aksyuk, V. A., An Efficient Large-Area Grating Coupler for Surface Plasmon Polaritons. Plasmonics 2012, 7 (2), 269-277.
20. Liu, L.; Xu, Y.; Zhu, J.; Wang, P.; Tong, L.; Krasavin, A. V., Excitation of Surface Plasmons by Inelastic Electron Tunneling. Frontiers in Physics 2020, 8.
21. Lirtsman, V.; Golosovsky, M.; Davidov, D., Surface plasmon excitation using a Fourier-transform infrared spectrometer: Live cell and bacteria sensing. Review of Scientific Instruments 2017, 88 (10), 103105.
22. Rakj , A. D.; Djuriaj , A. B.; Elazar, J. M.; Majewski, M. L., Optical properties of metallic films for vertical-cavity optoelectronic devices. Applied optics 1998, 37 22, 5271-83.
23. Solymar, L.; Shamonina, E., Waves in Metamaterials. OUP Oxford: 2009.
24. Pendry, J. B.; Smith, D. R., Reversing Light With Negative Refraction. Physics Today 2004, 57 (6), 37-43.
25. Sorger, V. J.; Oulton, R. F.; Yao, J.; Bartal, G.; Zhang, X., Plasmonic Fabry-Pérot Nanocavity. Nano Letters 2009, 9 (10), 3489-3493.
26. Suresh Kumar, N.; Naidu, K. C. B.; Banerjee, P.; Anil Babu, T.; Venkata Shiva Reddy, B., A Review on Metamaterials for Device Applications. Crystals 2021, 11 (5), 518.
27. Polman, A.; Atwater, H. A., Plasmonics: optics at the nanoscale. Materials Today 2005, 8 (1), 56.
28. Urbas, A. M.; Jacob, Z.; Negro, L. D.; Engheta, N.; Boardman, A. D.; Egan, P.; Khanikaev, A. B.; Menon, V.; Ferrera, M.; Kinsey, N.; DeVault, C.; Kim, J.; Shalaev, V.; Boltasseva, A.; Valentine, J.; Pfeiffer, C.; Grbic, A.; Narimanov, E.; Zhu, L.; Fan, S.; Alù, A.; Poutrina, E.; Litchinitser, N. M.; Noginov, M. A.; MacDonald, K. F.; Plum, E.; Liu, X.; Nealey, P. F.; Kagan,

C. R.; Murray, C. B.; Pawlak, D. A.; Smolyaninov, I. I.; Smolyaninova, V. N.; Chanda, D., Roadmap on optical metamaterials. Journal of Optics 2016, 18 (9), 093005.

29. Kim, S.-H.; Das, M. P., Understanding metamaterials in the realm of smart materials. AIP Conference Proceedings 2018, 2005 (1), 020011.
30. Losurdo, M.; Moreno, F.; Cobet, C.; Modreanu, M.; Pernice, W., Plasmonics: Enabling functionalities with novel materials. Journal of Applied Physics 2021, 129 (22), 220401.
31. Salim, A.; Lim, S., Recent advances in the metamaterial-inspired biosensors. Biosensors and Bioelectronics 2018, 117, 398-402.
32. Kasani, S.; Curtin, K.; Wu, N., A review of 2D and 3D plasmonic nanostructure array patterns: fabrication, light management and sensing applications. Nanophotonics 2019, 8 (12), 2065-2089.
33. Padilla, W. J.; Basov, D. N.; Smith, D. R., Negative refractive index metamaterials. Materials Today 2006, 9 (7), 28-35.
34. Papadakis, G. T.; Fleischman, D.; Davoyan, A.; Yeh, P.; Atwater, H. A., Optical magnetism in planar metamaterial heterostructures. Nature Communications 2018, 9 (1), 296.
35. Urzhumov, Y. A.; Shvets, G., Optical magnetism and negative refraction in plasmonic metamaterials. Solid State Communications 2008, 146 (5), 208-220.
36. Garcia, N.; Ponizovskaya, E. V.; Xiao, J. Q., Zero permittivity materials: Band gaps at the visible. Applied Physics Letters 2002, 80 (7), 1120-1122.
37. Mahmoud, A. M.; Engheta, N., Wave–matter interactions in epsilon-and-mu-near-zero structures. Nature Communications 2014, 5 (1), 5638.
38. Tsakmakidis, K. L.; Boardman, A. D.; Hess, O., 'Trapped rainbow' storage of light in metamaterials. Nature 2007, 450 (7168), 397-401.
39. Li, Y.; Su, L.; Shou, C.; Yu, C.; Deng, J.; Fang, Y., Surface-enhanced molecular spectroscopy (SEMS) based on perfect-absorber metamaterials in the mid-infrared. Scientific Reports 2013, 3 (1), 2865.
40. Guan, Y.; Wang, Z.; Ai, B.; Chen, C.; Zhang, W.; Wang, Y.; Zhang, G., Chiral Plasmonic Metamaterials with Tunable Chirality. ACS Applied Materials & Interfaces 2020, 12 (44), 50192-50202.
41. Deka, G.; Sun, C.-K.; Fujita, K.; Chu, S.-W., Nonlinear plasmonic imaging techniques and their biological applications. Nanophotonics 2017, 6 (1), 31-49.

42. Smith, J. G.; Faucheaux, J. A.; Jain, P. K., Plasmon resonances for solar energy harvesting: A mechanistic outlook. Nano Today 2015, 10 (1), 67-80.

43. Eversole, D.; Subramanian, K.; Harrison, R. K.; Bourgeois, F.; Yuksel, A.; Ben-Yakar, A., Femtosecond Plasmonic Laser Nanosurgery (fs-PLN) mediated by molecularly targeted gold nanospheres at ultra-low pulse fluences. Scientific Reports 2020, 10 (1), 12387.

44. Gellé, A.; Moores, A., Plasmonic nanoparticles: Photocatalysts with a bright future. Current Opinion in Green and Sustainable Chemistry 2019, 15, 60-66.

45. Song, M.; Wang, D.; Kudyshev, Z. A.; Xuan, Y.; Wang, Z.; Boltasseva, A.; Shalaev, V. M.; Kildishev, A. V., Enabling Optical Steganography, Data Storage, and Encryption with Plasmonic Colors. Laser & Photonics Reviews 2021, 15 (3), 2000343.

46. Li, J.-F.; Li, C.-Y.; Aroca, R. F., Plasmon-enhanced fluorescence spectroscopy. Chemical Society Reviews 2017, 46 (13), 3962-3979.

47. Liu, Z.; Yang, Z.; Peng, B.; Cao, C.; Zhang, C.; You, H.; Xiong, Q.; Li, Z.; Fang, J., Highly Sensitive, Uniform, and Reproducible Surface-Enhanced Raman Spectroscopy from Hollow Au-Ag Alloy Nanourchins. Advanced Materials 2014, 26 (15), 2431-2439.

48. Fang, J.; Du, S.; Lebedkin, S.; Li, Z.; Kruk, R.; Kappes, M.; Hahn, H., Gold Mesostructures with Tailored Surface Topography and Their Self-Assembly Arrays for Surface-Enhanced Raman Spectroscopy. Nano Letters 2010, 10 (12), 5006-5013.

49. Philip, A.; Kumar, A. R., The performance enhancement of surface plasmon resonance optical sensors using nanomaterials: A review. Coordination Chemistry Reviews 2022, 458, 214424.

50. Liu, S.-Y.; Huang, L.; Li, J.-F.; Wang, C.; Li, Q.; Xu, H.-X.; Guo, H.-L.; Meng, Z.-M.; Shi, Z.; Li, Z.-Y., Simultaneous Excitation and Emission Enhancement of Fluorescence Assisted by Double Plasmon Modes of Gold Nanorods. The Journal of Physical Chemistry C 2013, 117 (20), 10636-10642.

51. Wang, L.; Hasanzadeh Kafshgari, M.; Meunier, M., Optical Properties and Applications of Plasmonic-Metal Nanoparticles. Advanced Functional Materials 2020, 30 (51), 2005400.

52. Bucharskaya, A.; Maslyakova, G.; Terentyuk, G.; Yakunin, A.; Avetisyan, Y.; Bibikova, O.; Tuchina, E.; Khlebtsov, B.; Khlebtsov, N.; Tuchin, V., Towards Effective Photothermal/Photodynamic Treatment Using Plasmonic Gold Nanoparticles. International Journal of Molecular Sciences 2016, 17 (8), 1295.

53. Yuan, P.; Ding, X.; Yang, Y. Y.; Xu, Q.-H., Metal Nanoparticles for Diagnosis and Therapy of Bacterial Infection. Advanced Healthcare Materials 2018, 7 (13), 1701392.
54. Rastinehad, A. R.; Anastos, H.; Wajswol, E.; Winoker, J. S.; Sfakianos, J. P.; Doppalapudi, S. K.; Carrick, M. R.; Knauer, C. J.; Taouli, B.; Lewis, S. C.; Tewari, A. K.; Schwartz, J. A.; Canfield, S. E.; George, A. K.; West, J. L.; Halas, N. J., Gold nanoshell-localized photothermal ablation of prostate tumors in a clinical pilot device study. Proceedings of the National Academy of Sciences 2019, 116 (37), 18590-18596.
55. Ren, H.; Tang, M.; Guan, B.; Wang, K.; Yang, J.; Wang, F.; Wang, M.; Shan, J.; Chen, Z.; Wei, D.; Peng, H.; Liu, Z., Hierarchical Graphene Foam for Efficient Omnidirectional Solar–Thermal Energy Conversion. Advanced Materials 2017, 29 (38), 1702590.
56. Xuan, Y.; Duan, H.; Li, Q., Enhancement of solar energy absorption using a plasmonic nanofluid based on TiO2/Ag composite nanoparticles. RSC Advances 2014, 4 (31), 16206-16213.
57. Adamovic, N.; Schmid, U., Potential of plasmonics in photovoltaic solar cells. e & i Elektrotechnik und Informationstechnik 2011, 128 (10), 342-347.
58. Ueno, K.; Oshikiri, T.; Sun, Q.; Shi, X.; Misawa, H., Solid-State Plasmonic Solar Cells. Chemical Reviews 2018, 118 (6), 2955-2993.
59. Yao, K.; Zhong, H.; Liu, Z.; Xiong, M.; Leng, S.; Zhang, J.; Xu, Y.-x.; Wang, W.; Zhou, L.; Huang, H.; Jen, A. K. Y., Plasmonic Metal Nanoparticles with Core–Bishell Structure for High-Performance Organic and Perovskite Solar Cells. ACS Nano 2019, 13 (5), 5397-5409.
60. Jeong, S.-H.; Choi, H.; Kim, J. Y.; Lee, T.-W., Silver-Based Nanoparticles for Surface Plasmon Resonance in Organic Optoelectronics. Particle & Particle Systems Characterization 2015, 32 (2), 164-175.
61. Javed, H. M. A.; Sarfaraz, M.; Nisar, M. Z.; Qureshi, A. A.; e Alam, M. F.; Que, W.; Yin, X.; Abd-Rabboh, H. S. M.; Shahid, A.; Ahmad, M. I.; Ullah, S., Plasmonic Dye-Sensitized Solar Cells: Fundamentals, Recent Developments, and Future Perspectives. ChemistrySelect 2021, 6 (34), 9337-9350.
62. Catchpole, K. R.; Polman, A., Plasmonic solar cells. Opt. Express 2008, 16 (26), 21793-21800.
63. Siew, S. Y.; Li, B.; Gao, F.; Zheng, H. Y.; Zhang, W.; Guo, P.; Xie, S. W.; Song, A.; Dong, B.; Luo, L. W.; Li, C.; Luo, X.; Lo, G. Q., Review of Silicon Photonics Technology and Platform Development. Journal of Lightwave Technology 2021, 39 (13), 4374-4389.

64. Sharma, T.; Wang, J.; Kaushik, B. K.; Cheng, Z.; Kumar, R.; Wei, Z.; Li, X., Review of Recent Progress on Silicon Nitride-Based Photonic Integrated Circuits. IEEE Access 2020, 8, 195436-195446.

65. Song, M.; Wang, D.; Peana, S.; Choudhury, S.; Nyga, P.; Kudyshev, Z. A.; Yu, H.; Boltasseva, A.; Shalaev, V. M.; Kildishev, A. V., Colors with plasmonic nanostructures: A full-spectrum review. Applied Physics Reviews 2019, 6 (4), 041308.

66. Shaukat, A.; Noble, F.; Arif, K. M., Nanostructured Color Filters: A Review of Recent Developments. Nanomaterials 2020, 10 (8), 1554.

67. Liu, Y.; Lee, Y. H.; Zhang, Q.; Cui, Y.; Ling, X. Y., Plasmonic nanopillar arrays encoded with multiplex molecular information for anti-counterfeiting applications. Journal of Materials Chemistry C 2016, 4 (19), 4312-4319.

68. Wang, Z.; Zong, S.; Wu, L.; Zhu, D.; Cui, Y., SERS-Activated Platforms for Immunoassay: Probes, Encoding Methods, and Applications. Chemical Reviews 2017, 117 (12), 7910-7963.

69. Cheheltani, R.; Ezzibdeh, R. M.; Chhour, P.; Pulaparthi, K.; Kim, J.; Jurcova, M.; Hsu, J. C.; Blundell, C.; Litt, H. I.; Ferrari, V. A.; Allcock, H. R.; Sehgal, C. M.; Cormode, D. P., Tunable, biodegradable gold nanoparticles as contrast agents for computed tomography and photoacoustic imaging. Biomaterials 2016, 102, 87-97.

70. Ge, X.; Chen, B.; Liu, T.; Wei, L.; Tong, L.; Ma, Q.; Gao, S.; Song, J., Active targeting drug-gold nanorod hybrid nanoparticles for amplifying photoacoustic signal and enhancing anticancer efficacy. RSC Advances 2019, 9 (24), 13494-13502.

71. Liberal, I.; Engheta, N., Near-zero refractive index photonics. Nature Photonics 2017, 11 (3), 149-158.

72. Liberal, I.; Engheta, N., Zero-index platforms: Where light defies geometry. Optics and Photonics News 2016, 27 (7), 26-33.

73. Liberal, I.; Engheta, N., The rise of near-zero-index technologies. Science 2017, 358 (6370), 1540-1541.

74. Suchowski, H.; O'Brien, K.; Wong, Z. J.; Salandrino, A.; Yin, X.; Zhang, X., Phase Mismatch–Free Nonlinear Propagation in Optical Zero-Index Materials. Science 2013, 342 (6163), 1223-1226.

75. Enoch, S.; Tayeb, G.; Sabouroux, P.; Guérin, N.; Vincent, P., A Metamaterial for Directive Emission. Physical Review Letters 2002, 89 (21), 213902.

76. Mahmoud, A. M.; Engheta, N., " Static" Optics. arXiv preprint arXiv:1407.2338 2014.

77. Vulis, D. I.; Camayd-Muñoz, P.; Li, Y.; Reshef, O.; Lončar, M.; Mazur, E. In Integrated zero-index supercouplers, Frontiers in Optics 2017, Washington, D.C., 2017/09/18; Optica Publishing Group: Washington, D.C., 2017; p JW3A.108.
78. Liberal, I.; Engheta, N., Nonradiating and radiating modes excited by quantum emitters in open epsilon-near-zero cavities. Science Advances 2016, 2 (10), e1600987.
79. Silveirinha, M.; Engheta, N., Tunneling of electromagnetic energy through subwavelength channels and bends using ε-near-zero materials. Physical review letters 2006, 97 (15), 157403.
80. Powell, D. A.; Alù, A.; Edwards, B.; Vakil, A.; Kivshar, Y. S.; Engheta, N., Nonlinear control of tunneling through an epsilon-near-zero channel. Physical Review B 2009, 79 (24), 245135.
81. Niu, X.; Hu, X.; Chu, S.; Gong, Q., Epsilon-Near-Zero Photonics: A New Platform for Integrated Devices. Advanced Optical Materials 2018, 6 (10), 1701292.
82. Maas, R.; Parsons, J.; Engheta, N.; Polman, A., Experimental realization of an epsilon-near-zero metamaterial at visible wavelengths. Nature Photonics 2013, 7 (11), 907-912.
83. Pacheco-Peña, V.; Engheta, N.; Kuznetsov, S.; Gentselev, A.; Beruete, M., Experimental Realization of an Epsilon-Near-Zero Graded-Index Metalens at Terahertz Frequencies. Physical Review Applied 2017, 8 (3), 034036.
84. Wu, J.; Xie, Z. T.; Sha, Y.; Fu, H. Y.; Li, Q., Epsilon-near-zero photonics: infinite potentials. Photon. Res. 2021, 9 (8), 1616-1644.
85. David, C.; Mortensen, N. A.; Christensen, J., Perfect imaging, epsilon-near zero phenomena and waveguiding in the scope of nonlocal effects. Scientific Reports 2013, 3 (1), 2526.
86. Subramania, G.; Fischer, A. J.; Luk, T. S., Optical properties of metal-dielectric based epsilon near zero metamaterials. Applied Physics Letters 2012, 101 (24), 241107.
87. Caligiuri, V.; Palei, M.; Biffi, G.; Artyukhin, S.; Krahne, R., A Semi-Classical View on Epsilon-Near-Zero Resonant Tunneling Modes in Metal/Insulator/Metal Nanocavities. Nano Letters 2019, 19 (5), 3151-3160.
88. Vassant, S.; Archambault, A.; Marquier, F.; Pardo, F.; Gennser, U.; Cavanna, A.; Pelouard, J. L.; Greffet, J. J., Epsilon-Near-Zero Mode for Active Optoelectronic Devices. Physical Review Letters 2012, 109 (23), 237401.

89. Campione, S.; Kim, I.; de Ceglia, D.; Keeler, G. A.; Luk, T. S., Experimental verification of epsilon-near-zero plasmon polariton modes in degenerately doped semiconductor nanolayers. Opt. Express 2016, 24 (16), 18782-18789.

90. Edwards, B.; Alù, A.; Young, M. E.; Silveirinha, M.; Engheta, N., Experimental Verification of Epsilon-Near-Zero Metamaterial Coupling and Energy Squeezing Using a Microwave Waveguide. Physical Review Letters 2008, 100 (3), 033903.

91. Alù, A.; Engheta, N., Light squeezing through arbitrarily shaped plasmonic channels and sharp bends. Physical Review B 2008, 78 (3), 035440.

92. Mattheakis, M.; Valagiannopoulos, C. A.; Kaxiras, E., Epsilon-near-zero behavior from plasmonic Dirac point: Theory and realization using two-dimensional materials. Physical Review B 2016, 94 (20), 201404.

93. Moitra, P.; Yang, Y.; Anderson, Z.; Kravchenko, I. I.; Briggs, D. P.; Valentine, J., Realization of an all-dielectric zero-index optical metamaterial. Nature Photonics 2013, 7 (10), 791-795.

94. Newman, W. D.; Cortes, C. L.; Atkinson, J.; Pramanik, S.; DeCorby, R. G.; Jacob, Z., Ferrell–Berreman modes in plasmonic epsilon-near-zero media. Acs Photonics 2015, 2 (1), 2-7.

95. Javani, M. H.; Stockman, M. I., Real and Imaginary Properties of Epsilon-Near-Zero Materials. Physical Review Letters 2016, 117 (10), 107404.

96. Engheta, N., Pursuing Near-Zero Response. Science 2013, 340 (6130), 286-287.

97. Li, Y.; Kita, S.; Muñoz, P.; Reshef, O.; Vulis, D. I.; Yin, M.; Lončar, M.; Mazur, E., On-chip zero-index metamaterials. Nature Photonics 2015, 9 (11), 738-742.

98. Scully, M. O.; Svidzinsky, A. A., The Super of Superradiance. Science 2009, 325 (5947), 1510-1511.

99. Fleury, R.; Alù, A., Enhanced superradiance in epsilon-near-zero plasmonic channels. Physical Review B 2013, 87 (20), 201101.

100. Sokhoyan, R.; Atwater, H. A., Quantum optical properties of a dipole emitter coupled to an ε-near-zero nanoscale waveguide. Opt. Express 2013, 21 (26), 32279-32290.

101. Alù, A.; Silveirinha, M. G.; Salandrino, A.; Engheta, N., Epsilon-near-zero metamaterials and electromagnetic sources: Tailoring the radiation phase pattern. Physical Review B 2007, 75 (15), 155410.

102. Reshef, O.; De Leon, I.; Alam, M. Z.; Boyd, R. W., Nonlinear optical effects in epsilon-near-zero media. Nature Reviews Materials 2019, 4 (8), 535-551.

103. Boyd, R. W., Nonlinear Optics. Academic Press: 1992.

104. Yang, Y.; Lu, J.; Manjavacas, A.; Luk, T. S.; Liu, H.; Kelley, K.; Maria, J.-P.; Runnerstrom, E. L.; Sinclair, M. B.; Ghimire, S.; Brener, I., High-harmonic generation from an epsilon-near-zero material. Nature Physics 2019, 15 (10), 1022-1026.

105. Rocco, D.; Vincenti, M. A.; De Angelis, C., Boosting Second Harmonic Radiation from AlGaAs Nanoantennas with Epsilon-Near-Zero Materials. Applied Sciences 2018, 8 (11), 2212.

106. Silveirinha, M. G.; Engheta, N., Theory of supercoupling, squeezing wave energy, and field confinement in narrow channels and tight bends using $\ensuremath{\epsilon}$ near-zero metamaterials. Physical Review B 2007, 76 (24), 245109.

107. Liu, R.; Cheng, Q.; Hand, T.; Mock, J. J.; Cui, T. J.; Cummer, S. A.; Smith, D. R., Experimental Demonstration of Electromagnetic Tunneling Through an Epsilon-Near-Zero Metamaterial at Microwave Frequencies. Physical Review Letters 2008, 100 (2), 023903.

108. Caligiuri, V.; Palei, M.; Biffi, G.; Krahne, R., Hybridization of epsilon-near-zero modes via resonant tunneling in layered metal-insulator double nanocavities. Nanophotonics 2019, 8 (9), 1505-1512.

109. Caligiuri, V.; Biffi, G.; Palei, M.; Martín-García, B.; Pothuraju, R. D.; Bretonnière, Y.; Krahne, R., Angle and Polarization Selective Spontaneous Emission in Dye-Doped Metal/Insulator/Metal Nanocavities. Advanced Optical Materials 2020, 8 (1), 1901215.

110. Caligiuri, V.; Palei, M.; Imran, M.; Manna, L.; Krahne, R., Planar Double-Epsilon-Near-Zero Cavities for Spontaneous Emission and Purcell Effect Enhancement. ACS Photonics 2018, 5 (6), 2287-2294.

111. Caligiuri, V.; Biffi, G.; Patra, A.; Pothuraju, R. D.; De Luca, A.; Krahne, R., One-Dimensional Epsilon-Near-Zero Crystals. Advanced Photonics Research 2021, 2 (7), 2100053.

112. Zhou, X.; Tian, P.; Sher, C.-W.; Wu, J.; Liu, H.; Liu, R.; Kuo, H.-C., Growth, transfer printing and colour conversion techniques towards full-colour micro-LED display. Progress in Quantum Electronics 2020, 71, 100263.

113. Kazlauciunas, A., The role of colorants in the generation, storage, and output of digital still images. Coloration Technology 2014, 130 (1), 8-12.

114. Alamán, J.; Alicante, R.; Peña, J. I.; Sánchez-Somolinos, C., Inkjet Printing of Functional Materials for Optical and Photonic Applications. Materials 2016, 9 (11), 910.

115. Lin, H.-H.; Lee, C.-h.; Lu, M.-H., Dye-less color filter fabricated by roll-to-roll imprinting for liquid crystal display applications. Opt. Express 2009, 17 (15), 12397-12406.

116. Vukusic, P.; Sambles, J. R.; Lawrence, C. R.; Wootton, R. J., Now you see it — now you don't. Nature 2001, 410 (6824), 36-36.
117. Yu, Y.; Wen, L.; Song, S.; Chen, Q., Transmissive/Reflective Structural Color Filters: Theory and Applications. Journal of Nanomaterials 2014, 2014, 212637.
118. Proust, J.; Bedu, F.; Gallas, B.; Ozerov, I.; Bonod, N., All-Dielectric Colored Metasurfaces with Silicon Mie Resonators. ACS Nano 2016, 10 (8), 7761-7767.
119. Diest, K.; Dionne, J. A.; Spain, M.; Atwater, H. A., Tunable Color Filters Based on Metal−Insulator−Metal Resonators. Nano Letters 2009, 9 (7), 2579-2583.
120. Aalizadeh, M.; Serebryannikov, A. E.; Khavasi, A.; Vandenbosch, G. A. E.; Ozbay, E., Toward Electrically Tunable, Lithography-Free, Ultra-Thin Color Filters Covering the Whole Visible Spectrum. Scientific Reports 2018, 8 (1), 11316.
121. Lee, K.-T.; Han, S. Y.; Li, Z.; Baac, H. W.; Park, H. J., Flexible High-Color-Purity Structural Color Filters Based on a Higher-Order Optical Resonance Suppression. Scientific Reports 2019, 9 (1), 14917.
122. https://www.imechyperspectral.com/en/hyperspectral-imaging-technology
123. Lucarini, V.; Saarinen, J. J.; Peiponen, K. E.; Vartiainen, E. M., Kramers-Kronig Relations in Optical Materials Research. Springer Berlin Heidelberg: 2006.
124. Abutoama, M.; Abuleil, M.; Abdulhalim, I., Resonant Subwavelength and Nano-Scale Grating Structures for Biosensing Application: A Comparative Study. Sensors 2021, 21 (13), 4523.
125. Gnilitskyi, I.; Mamykin, S. V.; Lanara, C.; Hevko, I.; Dusheyko, M.; Bellucci, S.; Stratakis, E., Laser Nanostructuring for Diffraction Grating Based Surface Plasmon-Resonance Sensors. Nanomaterials 2021, 11 (3), 591.
126. Xu, T.; Wu, Y.-K.; Luo, X.; Guo, L. J., Plasmonic nanoresonators for high-resolution colour filtering and spectral imaging. Nature Communications 2010, 1 (1), 59.
127. Alaee, R.; Menzel, C.; Huebner, U.; Pshenay-Severin, E.; Bin Hasan, S.; Pertsch, T.; Rockstuhl, C.; Lederer, F., Deep-Subwavelength Plasmonic Nanoresonators Exploiting Extreme Coupling. Nano Letters 2013, 13 (8), 3482-3486.
128. Ghobadi, A.; Hajian, H.; Rashed, A. R.; Butun, B.; Ozbay, E., Tuning the metal filling fraction in metal-insulator-metal ultra-broadband perfect absorbers to maximize the absorption bandwidth. Photon. Res. 2018, 6 (3), 168-176.

129. Pothuraju, R. D.; Krahne, R. In Cavity and Dipole Resonances in Laterally Structured Metal-Insulator-Metal Nanocavities, 2021 Fifteenth International Congress on Artificial Materials for Novel Wave Phenomena (Metamaterials), 20-24 Sept. 2021; 2021; pp 340-342.

130. Zenin, V. A.; Garcia-Ortiz, C. E.; Evlyukhin, A. B.; Yang, Y.; Malureanu, R.; Novikov, S. M.; Coello, V.; Chichkov, B. N.; Bozhevolnyi, S. I.; Lavrinenko, A. V.; Mortensen, N. A., Engineering Nanoparticles with Pure High-Order Multipole Scattering. ACS Photonics 2020, 7 (4), 1067-1075.

131. Li, W.; Urbanski, L.; Marconi, M. C., Invited Article: Progress in coherent lithography using table-top extreme ultraviolet lasers. Review of Scientific Instruments 2015, 86 (12), 121301.

132. Mojarad, N.; Gobrecht, J.; Ekinci, Y., Interference lithography at EUV and soft X-ray wavelengths: Principles, methods, and applications. Microelectronic Engineering 2015, 143, 55-63.

133. Chen, H.; Qin, L.; Chen, Y.; Jia, P.; Gao, F.; Chen, C.; Liang, L.; Zhang, X.; Lou, H.; Ning, Y.; Wang, L., Refined grating fabrication using Displacement Talbot Lithography. Microelectronic Engineering 2018, 189, 74-77.

134. Wikipedia contributors, "Talbot effect," Wikipedia, The Free Encyclopedia, https://en.wikipedia.org/w/index.php?title=Talbot_effect&oldid=1071099763 (accessed March 5, 2022).

135. Manzeli, S.; Ovchinnikov, D.; Pasquier, D.; Yazyev, O. V.; Kis, A., 2D transition metal dichalcogenides. Nature Reviews Materials 2017, 2 (8), 17033.

136. Choi, W.; Choudhary, N.; Han, G. H.; Park, J.; Akinwande, D.; Lee, Y. H., Recent development of two-dimensional transition metal dichalcogenides and their applications. Materials Today 2017, 20 (3), 116-130.

137. Gryczynski, I.; Malicka, J.; Gryczynski, Z.; Lakowicz, J. R., Surface Plasmon-Coupled Emission with Gold Films. The Journal of Physical Chemistry B 2004, 108 (33), 12568-12574.

138. Kuznetsov, A. I.; Miroshnichenko, A. E.; Brongersma, M. L.; Kivshar, Y. S.; Luk'yanchuk, B., Optically resonant dielectric nanostructures. Science 2016, 354 (6314), aag2472.

139. Decker, M.; Staude, I., Resonant dielectric nanostructures: a low-loss platform for functional nanophotonics. Journal of Optics 2016, 18 (10), 103001.

140. Zhao, Q.; Zhou, J.; Zhang, F.; Lippens, D., Mie resonance-based dielectric metamaterials. Materials Today 2009, 12 (12), 60-69.

141. Vismara, R.; Länk, N. O.; Verre, R.; Käll, M.; Isabella, O.; Zeman, M., Solar harvesting based on perfect absorbing all-dielectric nanoresonators on a mirror. Opt. Express 2019, 27 (16), A967-A980.

142. Chandra, S.; Chowdhury, J., SERS on all dielectric materials: A brief review. 2019, 28, 177-189.

143. Bontempi, N.; Chong, K. E.; Orton, H. W.; Staude, I.; Choi, D.-Y.; Alessandri, I.; Kivshar, Y. S.; Neshev, D. N., Highly sensitive biosensors based on all-dielectric nanoresonators. Nanoscale 2017, 9 (15), 4972-4980.

144. Evlyukhin, A. B.; Novikov, S. M.; Zywietz, U.; Eriksen, R. L.; Reinhardt, C.; Bozhevolnyi, S. I.; Chichkov, B. N., Demonstration of Magnetic Dipole Resonances of Dielectric Nanospheres in the Visible Region. Nano Letters 2012, 12 (7), 3749-3755.

145. Pinton, N.; Grant, J.; Collins, S.; Cumming, D. R. S., Exploitation of Magnetic Dipole Resonances in Metal–Insulator–Metal Plasmonic Nanostructures to Selectively Filter Visible Light. ACS Photonics 2018, 5 (4), 1250-1261.

146. Huo, P.; Zhang, S.; Liang, Y.; Lu, Y.; Xu, T., Hyperbolic Metamaterials and Metasurfaces: Fundamentals and Applications. Advanced Optical Materials 2019, 7 (14), 1801616.

147. Chen, H.-T.; Taylor, A. J.; Yu, N., A review of metasurfaces: physics and applications. Reports on Progress in Physics 2016, 79 (7), 076401.

148. Pendry, J. B., Negative Refraction Makes a Perfect Lens. Physical Review Letters 2000, 85 (18), 3966-3969.

149. Liu, N.; Langguth, L.; Weiss, T.; Kästel, J.; Fleischhauer, M.; Pfau, T.; Giessen, H., Plasmonic analogue of electromagnetically induced transparency at the Drude damping limit. Nature Materials 2009, 8 (9), 758-762.

150. Poddubny, A.; Iorsh, I.; Belov, P.; Kivshar, Y., Hyperbolic metamaterials. Nature Photonics 2013, 7 (12), 948-957.

151. Haxha, S.; AbdelMalek, F.; Ouerghi, F.; Charlton, M. D. B.; Aggoun, A.; Fang, X., Metamaterial Superlenses Operating at Visible Wavelength for Imaging Applications. Scientific Reports 2018, 8 (1), 16119.

152. Landy, N. I.; Sajuyigbe, S.; Mock, J. J.; Smith, D. R.; Padilla, W. J., Perfect Metamaterial Absorber. Physical Review Letters 2008, 100 (20), 207402.

153. Yoo, S.; Park, Q.-H., Metamaterials and chiral sensing: a review of fundamentals and applications. Nanophotonics 2019, 8 (2), 249-261.

154. Brady, B.; Steenhof, V.; Nickel, B.; Blackburn, A. M.; Vehse, M.; Brolo, A. G., Plasmonic Light-Trapping Concept for Nanoabsorber Photovoltaics. ACS Applied Energy Materials 2019, 2 (3), 2255-2262.

155. Moritake, Y.; Tanaka, T., Controlling bi-anisotropy in infrared metamaterials using three-dimensional split-ring-resonators for purely magnetic resonance. Scientific Reports 2017, 7 (1), 6726.

156. Gigli, C.; Marino, G.; Borne, A.; Lalanne, P.; Leo, G., All-Dielectric Nanoresonators for $\chi(2)$ Nonlinear Optics. Frontiers in Physics 2019, 7.

157. Kuznetsov, A. I.; Miroshnichenko, A. E.; Fu, Y. H.; Zhang, J.; Luk'yanchuk, B., Magnetic light. Scientific Reports 2012, 2 (1), 492.

158. Yan, J. H.; Liu, P.; Lin, Z. Y.; Wang, H.; Chen, H. J.; Wang, C. X.; Yang, G. W., Magnetically induced forward scattering at visible wavelengths in silicon nanosphere oligomers. Nature Communications 2015, 6 (1), 7042.

159. Yu, Y. F.; Zhu, A. Y.; Paniagua-Domínguez, R.; Fu, Y. H.; Luk'yanchuk, B.; Kuznetsov, A. I., High-transmission dielectric metasurface with 2π phase control at visible wavelengths. Laser & Photonics Reviews 2015, 9 (4), 412-418.

160. Shibanuma, T.; Matsui, T.; Roschuk, T.; Wojcik, J.; Mascher, P.; Albella, P.; Maier, S. A., Experimental Demonstration of Tunable Directional Scattering of Visible Light from All-Dielectric Asymmetric Dimers. ACS Photonics 2017, 4 (3), 489-494.

161. Lin, L.; Jiang, Z. H.; Ma, D.; Yun, S.; Liu, Z.; Werner, D. H.; Mayer, T. S., Dielectric nanoresonator based lossless optical perfect magnetic mirror with near-zero reflection phase. Applied Physics Letters 2016, 108 (17), 171902.

162. Decker, M.; Staude, I.; Falkner, M.; Dominguez, J.; Neshev, D. N.; Brener, I.; Pertsch, T.; Kivshar, Y. S., High-Efficiency Dielectric Huygens' Surfaces. Advanced Optical Materials 2015, 3 (6), 813-820.

163. Afanasiev, G. N.; Stepanovsky, Y. P., THE ELECTROMAGNETIC FIELD OF ELEMENTARY TIME-DEPENDENT TOROIDAL SOURCES. Journal of Physics A 1995, 28, 4565-4580.

164. Fedotov, V. A.; Rogacheva, A. V.; Savinov, V.; Tsai, D. P.; Zheludev, N. I., Resonant Transparency and Non-Trivial Non-Radiating Excitations in Toroidal Metamaterials. Scientific Reports 2013, 3 (1), 2967.

165. Miroshnichenko, A. E.; Evlyukhin, A. B.; Yu, Y. F.; Bakker, R. M.; Chipouline, A.; Kuznetsov, A. I.; Luk'yanchuk, B.; Chichkov, B. N.; Kivshar, Y. S., Nonradiating anapole modes in dielectric nanoparticles. Nature Communications 2015, 6 (1), 8069.

166. Savinov, V.; Papasimakis, N.; Tsai, D. P.; Zheludev, N. I., Optical anapoles. Communications Physics 2019, 2 (1), 69.

167. Mazzone, V.; Totero Gongora, J. S.; Fratalocchi, A., Near-Field Coupling and Mode Competition in Multiple Anapole Systems. Applied Sciences 2017, 7 (6), 542.

168. Ospanova, A. K.; Stenishchev, I. V.; Basharin, A. A., Anapole Mode Sustaining Silicon Metamaterials in Visible Spectral Range. Laser & Photonics Reviews 2018, 12 (7), 1800005.

169. Lamprianidis, A. G.; Miroshnichenko, A. E., Excitation of nonradiating magnetic anapole states with azimuthally polarized vector beams. Beilstein Journal of Nanotechnology 2018, 9, 1478-1490.

170. Kapitanova, P.; Zanganeh, E.; Pavlov, N.; Song, M.; Belov, P.; Evlyukhin, A.; Miroshnichenko, A., Seeing the Unseen: Experimental Observation of Magnetic Anapole State Inside a High-Index Dielectric Particle. Annalen der Physik 2020, 532 (12), 2000293.

171. Yang, Y.; Bozhevolnyi, S. I., Nonradiating anapole states in nanophotonics: from fundamentals to applications. Nanotechnology 2019, 30 (20), 204001.

172. Amanaganti, S. R.; Ravnik, M.; Dontabhaktuni, J., Collective photonic response of high refractive index dielectric metasurfaces. Scientific Reports 2020, 10 (1), 15599.

173. van de Groep, J.; Polman, A., Designing dielectric resonators on substrates: Combining magnetic and electric resonances. Opt. Express 2013, 21 (22), 26285-26302.

174. Qin, C.; Guo, Y.; Seo, J.; Shuai, Y.; Lee, J.; Lee, B. J., Absorption characteristics of a metal-insulator-metal nanodisk for solar thermal applications. Opt. Express 2020, 28 (10), 15731-15743.

175. Koya, A. N.; Zhu, X.; Ohannesian, N.; Yanik, A. A.; Alabastri, A.; Proietti Zaccaria, R.; Krahne, R.; Shih, W.-C.; Garoli, D., Nanoporous Metals: From Plasmonic Properties to Applications in Enhanced Spectroscopy and Photocatalysis. ACS Nano 2021, 15 (4), 6038-6060.

176. Fujita, T., Hierarchical nanoporous metals as a path toward the ultimate three-dimensional functionality. Science and Technology of Advanced Materials 2017, 18 (1), 724-740.

177. Ponzellini, P.; Giovannini, G.; Cattarin, S.; Zaccaria, R. P.; Marras, S.; Prato, M.; Schirato, A.; D'Amico, F.; Calandrini, E.; De Angelis, F.; Yang, W.; Jin, H.-J.; Alabastri, A.; Garoli, D.,

Metallic Nanoporous Aluminum–Magnesium Alloy for UV-Enhanced Spectroscopy. The Journal of Physical Chemistry C 2019, 123 (33), 20287-20296.

178. Qiu, H. J.; Li, X.; Xu, H.-T.; Zhang, H.-J.; Wang, Y., Nanoporous metal as a platform for electrochemical and optical sensing. Journal of Materials Chemistry C 2014, 2 (46), 9788-9799.

179. Zhang, J.; Li, C. M., Nanoporous metals: fabrication strategies and advanced electrochemical applications in catalysis, sensing and energy systems. Chemical Society Reviews 2012, 41 (21), 7016-7031.

180. Qiu, H. J.; Xu, H.-T.; Liu, L.; Wang, Y., Correlation of the structure and applications of dealloyed nanoporous metals in catalysis and energy conversion/storage. Nanoscale 2015, 7 (2), 386-400.

181. Huang, A.; He, Y.; Zhou, Y.; Zhou, Y.; Yang, Y.; Zhang, J.; Luo, L.; Mao, Q.; Hou, D.; Yang, J., A review of recent applications of porous metals and metal oxide in energy storage, sensing and catalysis. Journal of Materials Science 2019, 54 (2), 949-973.

182. Gonçalves, J. M.; Kumar, A.; da Silva, M. I.; Toma, H. E.; Martins, P. R.; Araki, K.; Bertotti, M.; Angnes, L., Nanoporous Gold-Based Materials for Electrochemical Energy Storage and Conversion. Energy Technology 2021, 9 (5), 2000927.

183. Qian, L. H.; Yan, X. Q.; Fujita, T.; Inoue, A.; Chen, M. W., Surface enhanced Raman scattering of nanoporous gold: Smaller pore sizes stronger enhancements. Applied Physics Letters 2007, 90 (15), 153120.

184. Lang, X. Y.; Chen, L. Y.; Guan, P. F.; Fujita, T.; Chen, M. W., Geometric effect on surface enhanced Raman scattering of nanoporous gold: Improving Raman scattering by tailoring ligament and nanopore ratios. Applied Physics Letters 2009, 94 (21), 213109.

185. Ron, R.; Haleva, E.; Salomon, A., Nanoporous Metallic Networks: Fabrication, Optical Properties, and Applications. Advanced Materials 2018, 30 (41), 1706755.

186. Rebbecchi, T. A.; Chen, Y., Template-based fabrication of nanoporous metals. Journal of Materials Research 2018, 33 (1), 2-15.

187. Bartlett, P. N.; Baumberg, J. J.; Birkin, P. R.; Ghanem, M. A.; Netti, M. C., Highly Ordered Macroporous Gold and Platinum Films Formed by Electrochemical Deposition through Templates Assembled from Submicron Diameter Monodisperse Polystyrene Spheres. Chemistry of Materials 2002, 14 (5), 2199-2208.

188. Haupt, M.; Miller, S.; Glass, R.; Arnold, M.; Sauer, R.; Thonke, K.; Möller, M.; Spatz, J. P., Nanoporous Gold Films Created Using Templates Formed from Self-Assembled Structures of Inorganic–Block Copolymer Micelles. Advanced Materials 2003, 15 (10), 829-831.
189. Guo, X.; Zhang, C.; Tian, Q.; Yu, D., Liquid metals dealloying as a general approach for the selective extraction of metals and the fabrication of nanoporous metals: A review. Materials Today Communications 2021, 26, 102007.
190. Chen, Q.; Ding, Y.; Chen, M., Nanoporous metal by dealloying for electrochemical energy conversion and storage. MRS Bulletin 2018, 43 (1), 43-48.
191. Zhao, C.; Kisslinger, K.; Huang, X.; Bai, J.; Liu, X.; Lin, C.-H.; Yu, L.-C.; Lu, M.; Tong, X.; Zhong, H.; Pattammattel, A.; Yan, H.; Chu, Y.; Ghose, S.; Liu, M.; Chen-Wiegart, Y.-c. K., Design nanoporous metal thin films via solid state interfacial dealloying. Nanoscale 2021, 13 (42), 17725-17736.
192. Hu, L.-W.; Liu, X.; Le, G.-M.; Li, J.-F.; Qu, F.-S.; Lu, S.-Y.; Qi, L., Morphology evolution and SERS activity of the nanoporous Au prepared by dealloying sputtered Au-Ag film. Physica B: Condensed Matter 2019, 558, 49-53.
193. Seker, E.; Reed, M. L.; Begley, M. R., Nanoporous Gold: Fabrication, Characterization, and Applications. Materials 2009, 2 (4), 2188-2215.
194. Pedireddy, S.; Lee, H. K.; Tjiu, W. W.; Phang, I. Y.; Tan, H. R.; Chua, S. Q.; Troadec, C.; Ling, X. Y., One-step synthesis of zero-dimensional hollow nanoporous gold nanoparticles with enhanced methanol electrooxidation performance. Nature Communications 2014, 5 (1), 4947.
195. Li, Y.; Zhang, Z.; Wang, M.; Men, X.; Xue, Q., Environmentally safe, substrate-independent and repairable nanoporous coatings: large-scale preparation, high transparency and antifouling properties. Journal of Materials Chemistry A 2017, 5 (38), 20277-20288.
196. https://www.lumerical.com/products/.
197. Kane, Y., Numerical solution of initial boundary value problems involving maxwell's equations in isotropic media. IEEE Transactions on Antennas and Propagation 1966, 14 (3), 302-307.
198. Archambeault, B.; Ramahi, O. M.; Brench, C., The Finite-Difference Time-Domain Method. In EMI/EMC Computational Modeling Handbook, Springer US: Boston, MA, 1998; pp 35-67.
199. Griffiths, D. J., Introduction to Electrodynamics. Pearson Education: 2014.

200. Kunz, K. S.; Luebbers, R. J., The Finite Difference Time Domain Method for Electromagnetics. Taylor & Francis: 1993.

201. R, P.; S, R.; M.Savith; M.Balachandar, REVIEW OF PHYSICAL VAPOUR DEPOSITION (PVD) TECHNIQUES. 2013.

202. Sun, L.; Yuan, G.; Gao, L.; Yang, J.; Chhowalla, M.; Gharahcheshmeh, M. H.; Gleason, K. K.; Choi, Y. S.; Hong, B. H.; Liu, Z., Chemical vapour deposition. Nature Reviews Methods Primers 2021, 1 (1), 5.

203. Wang, Z.; Zhang, Z., Electron Beam Evaporation Deposition. In Advanced Nano Deposition Methods, 2016; pp 33-58.

204. Nishimura, Y.; Yano, K.; Itoh, M.; Ito, M., Photolithography. In Flat Panel Display Manufacturing, 2018; pp 287-310.

205. Luo, C.; Xu, C.; Lv, L.; Li, H.; Huang, X.; Liu, W., Review of recent advances in inorganic photoresists. RSC Advances 2020, 10 (14), 8385-8395.

206. Xie, Z.; Yu, W.; Wang, T.; Zhang, H.; Fu, Y.; Liu, H.; Li, F.; Lu, Z.; Sun, Q., Plasmonic Nanolithography: A Review. Plasmonics 2011, 6 (3), 565.

207. Willson, C. G.; Dammel, R.; Reiser, A., Photoresist materials: a historical perspective. SPIE: 1997; Vol. 3050.

208. Totzeck, M.; Ulrich, W.; Göhnermeier, A.; Kaiser, W., Pushing deep ultraviolet lithography to its limits. Nature Photonics 2007, 1 (11), 629-631.

209. Wu, B.; Kumar, A., Extreme ultraviolet lithography: A review. Journal of Vacuum Science & Technology B: Microelectronics and Nanometer Structures Processing, Measurement, and Phenomena 2007, 25 (6), 1743-1761.

210. Chen, Y., Nanofabrication by electron beam lithography and its applications: A review. Microelectronic Engineering 2015, 135, 57-72.

211. Vieu, C.; Carcenac, F.; Pépin, A.; Chen, Y.; Mejias, M.; Lebib, A.; Manin-Ferlazzo, L.; Couraud, L.; Launois, H., Electron beam lithography: resolution limits and applications. Applied Surface Science 2000, 164 (1), 111-117.

212. Li, P., A review of proximity effect correction in electron-beam lithography. arXiv preprint arXiv:1509.05169 2015.

213. Franssila, S.; Sainiemi, L., Reactive Ion Etching (RIE). In Encyclopedia of Microfluidics and Nanofluidics, Li, D., Ed. Springer US: Boston, MA, 2013; pp 1-13.

214. Irene, E. A., Applications of spectroscopic ellipsometry to microelectronics. Thin Solid Films 1993, 233 (1), 96-111.

215. Cody, D.; Babeva, T.; Madjarova, V.; Kharchenko, A.; Sabad-e-Gul; Mintova, S.; Barrett, C. J.; Naydenova, I., In-Situ Ellipsometric Study of the Optical Properties of LTL-Doped Thin Film Sensors for Copper(II) Ion Detection. Coatings 2020, 10 (4), 423.

216. Li, K.; Wang, S.; Wang, L.; Yu, H.; Jing, N.; Xue, R.; Wang, Z., Fast and Sensitive Ellipsometry-Based Biosensing. Sensors 2018, 18 (1), 15.

217. Azzam, R. M. A.; Azzam, R. M.; Bashara, N. M., Ellipsometry and Polarized Light. North-Holland: 1987.

218. Goodhew, P. J.; Humphreys, J.; Beanland, R., Electron microscopy and analysis. CRC press: 2000.

219. Idrobo, J. C., A new resolution quest in electron microscopy. Nature Reviews Materials 2021, 6 (2), 100-102.

220. Eaton, P.; West, P., Atomic force microscopy. Oxford university press: 2010.

221. Giessibl, F. J., Advances in atomic force microscopy. Reviews of modern physics 2003, 75 (3), 949.